Xin Zhao

A Contribution to the Computer Aided Development of an Electrical Window Regulator System

A Contribution to the Computer Aided Development of an Electrical Window Regulator System

Mechatronic Models, Parameter Identification and Numerical Simulations

Xin Zhao

Universitätsverlag Ilmenau
2015

Impressum

Bibliografische Information der Deutschen Nationalbibliothek
Die Deutsche Nationalbibliothek verzeichnet diese Publikation in der Deutschen Nationalbibliografie; detaillierte bibliografische Angaben sind im Internet über http://dnb.d-nb.de abrufbar.

Diese Arbeit hat der Fakultät für Maschinenbau der Technischen Universität Ilmenau als Dissertation vorgelegen.

Tag der Einreichung:	11. November 2014
1. Gutachter:	Univ.-Prof. Dr.-Ing. habil. Klaus Zimmermann (Technische Universität Ilmenau)
2. Gutachter:	Prof. Dr.-Ing. Johannes Zentner (HTWK Leipzig)
3. Gutachter:	Dr. Sergey Petkun (Brose Fahrzeugteile GmbH & Co. Kommanditgesellschaft, Hallstadt)
Tag der Verteidigung:	26. Februar 2015

Technische Universität Ilmenau/Universitätsbibliothek
Universitätsverlag Ilmenau
Postfach 10 05 65
98684 Ilmenau
www.tu-ilmenau.de/universitaetsverlag

Herstellung und Auslieferung
Verlagshaus Monsenstein und Vannerdat OHG
Am Hawerkamp 31
48155 Münster
www.mv-verlag.de

ISBN 978-3-86360-121-8 (Druckausgabe)
URN urn:nbn:de:gbv:ilm1-2015000266

Titelfoto: Veit Henkel | Fakultät für Maschinenbau, TU Ilmenau

Acknowledgements

This work is financially supported by Brose Fahrzeugteile GmbH & Co. Kommanditgesellschaft, Hallstadt. Hereby, I would thank Mr. T. Spangler and Mr. R. Kalb for the trust and the chance they have given me. Without them, this work would not come into being.

I would like to express my deep appreciation to Prof. K. Zimmermann, Dr. I. Zeidis and Dr. S. Petkun for the academic guidance. The advices are like lights when I was lost in darkness searching for a way out. And there were lots of discussion with Dr. Petkun. We had many interesting ideas. It is not sure whether these ideas are going to be realized or not. But, for me, such mental exercises make me more thoughtful. Dr. Petkun deserves this special thank.

I would like to thank Mr. S. Bars, Mr. D. Welz, Mr. T. Scholz and many other Brose colleagues for the support in helping me understand working principle, measurements and so on. Without their explanation, I would be still struggling.

In the end, I thank friends, seniors, my girlfriend, Miss. W.T. Li, and my families for the continual encouragement. Because of it, I went through the hardest time and did not collapse. Now, I smile to all I encounter without fear, because I know you will be with me all the time.

Abstract

The work is oriented to develop models and simulations of electrical power window regulator system, with the objectives to obtain improved understandings of system behaviors and parameter influence. Under the background that window regulator system is becoming a complicated mechatronic system, simulation is more and more frequently utilized. In this work, general simulations of mechatronic system on different level are compared. Applications of simulating window regulator are summarized and compared. Based on comparison, system simulation with uniformed modeling language, VHDL-AMS, is chosen as method.

Before diving deeply into detailed modeling of window regulator system, a highly abstracted analytical models is built up to study its dynamic behavior. Principally, the model has two degrees of freedom and is formed in the way that two masses are connected by spring and damper. One mass stands for glass and the other is for inertia of motor armature. With method of averaging, the analytical model is studied to find out the condition of system stability. Modeling of window regulator system begins with dividing system into components, according to functions. Components, such as electrical drive, lifting mechanism, door frame, electronic system and so on, are studied and modeled to described either electrical or mechanical behavior. Depending on the complexity of behaviors, modeling techniques are accordingly chosen, for example, physical modeling or behavioral modeling or a combination of both.

Parametrization of models is achieved with information combined from component suppliers, existing data bank and measurements. Component models are verified and validated against their component measurements, for instance, drive characteristic lines. System simulation deals with integration of all component models in one simulation bench and imitates operations of window regulator under different working cases. Important signals, which monitor state of system, like speed of drive and current, are compared between simulation and measurement in a concrete application of window regulator. Furthermore, anti-pinch function is compared, quantitatively by pinching forces under several voltages. However, applications of simulations are not limited to the examples demonstrated in the thesis. Subsystem simulations with emphasis on investigation of components can be developed with component models.

Kurzfassung

Die Arbeit orientiert sich daran, Modelle und Simulationen von elektrischen Fensterhebersystemen zu entwickeln. Das Ziel ist verbessertes Verständnis des Systemverhaltens und Einfluss von Parametern zu erlangen. Vor dem Hintergrund, dass Fensterhebersysteme komplizierte mechatronische Systeme darstellen, wird die Simulation als Werkzeug vermehrt eingesetzt. In dieser Arbeit werden verschiedene Simulation–en von mechatronischen Systemen auf unterschiedlichen Ebenen verglichen. Applikationen von Fensterhebersimulationen werden zusummengefasst und bewertet. Basierend auf dieser Auswertung wurde die Systemsimulation mit der Modellierungssprache, VHDL-AMS, als Methode ausgewählt.

Bevor sich tiefgründig mit der Modellierung von Fensterheber–systemen beschäftigt wird, soll zuvor ein stark abstrahiertes analytisches Modell für die Bewertung des dynamischen Verhaltens erstellt werden. Grundlegend besitzt das Modell 2 Freiheitsgrade und besteht aus 2 Massen, die über eine Feder und einen Dämpfer verbunden sind. Eine Masse stellt die Glasscheibe und die andere die Massenträgheit des Motorankers dar. Mit der Mittelwertmethode wird das analytische Modell hinsichtlich der Stabilitätsbedingungen untersucht. Die Modellbildung des Fensterhebersystems beginnt mit der Aufteilung des Systems in einzelne Komponenten, basierend auf deren Funktion. Die Komponenten, wie z.B. elektrische Motoren, Hebemechaniken, Türrahmen, Elektroniken, etc., werden untersucht und anschließend Modelle erstellt, um ihre elektrische oder mechanische Funktionsweise zu beschreiben. Abhängig von

der Komplexität wird die Technik der Modellierung ausgesucht, zum Beispiel physikalische oder verhaltensmäßige Modellierung oder eine Kombination von beiden.

Die Parameter der Modelle wurden anhand von gesammelten Informationen von Komponentenlieferanten, existierenden Datenbanken und Messungen ermittelt. Komponentenmodelle wurden anhand von Messdaten verifiziert, z.B. Motorkennlinie. Die Systemsimulation beschäftigt sich mit der Integration von allen Komponentenmodellen in eine Simulation und imitiert Ausführung der Fensterhebersysteme in verschiedenen Lastfällen. In einer konkreten Applikation wurden die Ergebnisse der Messung und der Simulation anhand der Werte von wichtigen Signalen, die den Status des Systems abbilden, wie zum Beispiel Drehzahl und Strom des Motors, verglichen. Außerdem wurde die Einklemmschutzfunktion quantitativ durch Messung der Einklemmkräfte bei verschiedenen Spannungen verglichen. Trotzdem sind die Simulationen nicht auf die demonstrierten Beispiele dieser Arbeit limitiert. Teilsystemsimulationen mit dem Schwerpunkt auf der Untersuchung von Komponenten können auch mit den Komponentenmodellen entwickelt werden.

Contents

Abbreviations

2D	two dimensional.
3D	three dimensional.
BroSAnT	Brose Simulation Analysis Tool.
DC	Direct Current.
DCPM motor	Direct Current Permanent Magnet motor.
ECU	Electronic Control Unit.
EMF	Electromotive Force.
M&S	Modeling and simulation.
VHDL	VHSIC Hardware Description Language.
VHDL–AMS	VHDL–Analog and Mixed Signal.
VHSIC	Very High Speed Integrated Circuit.
WR	Window regulator.

Symbols

α	Coefficient to convert dimensional system to non-dimensional system.
β	Ratio between F_a and F_r.
Δ	Coefficient of frequence displacement.
ε	Coefficient to convert dimensional system to non-dimensional system.
c	Stiffness of window regulator mechanism.
F_a	Equivalent driving force from drive.
F_r	Friction force to window regulator.
i	Reduction ratio of worm gear.
J_a	Moment of inertia of armature in drive.
J_w	Equivalent moment of inertia of armature in electrical drive, after conversion over worm gear.
L	Length scale to convert dimensional to non-dimensional displacement.
M	Sum of M_1 and M_2.
M_1	Equivalent mass for moment of internia of motor armature.
m_1	Ratio of M_1 and M.
M_2	Mass of window glass.
m_2	Sum of M_2 and M.
μ	Damping factor of window regulator.
η_w	Power transmission ratio of worm gear.
ν	ratio between angular frequency ω and ω_0.

ω_a	Rotational velocity of armature.
ω_w	Rotational velocity of gear wheel.
r_{cd}	Radius of cable drum.
sgn	Sign function.
t^*	Dimensional time.
t	Non-dimensional time.
V_1	Tangential speed of cable drum.
ω_0	Time scale to convert dimensional time to non-dimensional time.
x_1^*	Dimensional displacement of M_1.
$\dot{x}_1^*$	One order differentiation of dimensional displacement of M_1.
$\ddot{x}_1^*$	Tow order differentiation of dimensional displacement of M_1.
x_1	Non–dimensional displacement of M_1.
$\dot{x}_1$	One order differentiation of non–dimensional displacement of M_1.
$\ddot{x}_1$	Tow order differentiation of non–dimensional displacement of M_1.
x_2^*	Dimensional displacement of M_2.
$\dot{x}_2^*$	One order differentiation of dimensional displacement of M_2.
$\ddot{x}_2^*$	Tow order differentiation of dimensional displacement of M_2.
x_2	Non–dimensional displacement of M_2.
$\dot{x}_2$	One order differentiation of no–dimensional displacement of M_2.
$\ddot{x}_2$	Tow order differentiation of non–dimensional displacement of M_2.
i_0	No–load current of motor, unit: A.
i_a	Motor current, unit: A.
i_b	Stall current of motor, unit: A.

k_e	Back Electromotive Force (EMF) constant, unit: V/(rad/s).
k_t	Torque constant, unit: Nm/A.
L_a	Motor inductance, unit: F.
M_b	Stall torque of motor armature, unit: Nm.
M_c	Coulomb's dry friction torque, unit: Nm.
J_a	Moment of inertia of motor armature, unit: kg$\cdot$ m^2.
M_{la}	Load torque at armature, unit: Nm.
ω_i	Idle speed of motor armature, unit: rad/s.
R_a	Motor resistance, unit: Ω.
U_a	Motor voltage , unit: V.
$Visc$	Viscous friction coefficient, unit: Nm/(rad/s).
ω_a	Rotational velocity of armature, unit: rad/s.
ω_{a0}	No–load rotational velocity of motor armature, unit: rad/s.
F_f	friction force between worm gear at contacting face, unit: N.
F_{gAxi}	Force of gear in axial direction, unit: N.
F_{gAxiNf}	Force of gear in axial direction with no friction considered, unit: N.
F_{gRad}	Force of gear in radial direction, unit: N.
F_{gRadNf}	Force of gear in radial direction with no friction considered, unit: N.
F_{gTan}	Force of gear in tangential direction, unit: N.
F_{gTanNf}	Force of gear in tangential direction with no friction considered, unit: N.
F_n	Normal force at contacting face, unit: N.
F_{sq}	Squeezing force to friction model in worm gear model, unit: N.

F_{wAxi}	Force of worm in axial direction, unit: N.
F_{wAxiNf}	Force of worm in axial direction with no friction considered, unit: N.
F_{wRad}	Force of worm in radial direction, unit: N.
F_{wRadNf}	Force of worm in radial direction with no friction considered, unit: N.
F_{wTan}	Force of worm in tangential direction, unit: N.
F_{wTanNf}	Force of worm in tangential direction with no friction considered, unit: N.
M_f	Friction torque in worm gear model, unit: Nm.
M_g	Torque at gear, unit: Nm.
M_i	Torque at internal pin in worm gear model, unit: Nm.
μ_c	Coulomb friction coefficient.
M_w	Torque at worm, unit: Nm.
φ_g	Angle at gear, unit: rad.
φ_i	Angle at internal pin in worm gear model, unit: rad.
φ_l	Lear angle of worm gear, unit: rad.
φ_p	Press angle of worm gear, unit: rad.
φ_w	Angle at worm, unit: rad.
r_g	Pitch radius of gear, unit: m.
r_w	Pitch radius of worm, unit: m.
S_f	Relative displacement of worm and gear at contacting face at pitch circle, unit: m.
S_g	Peripheral displacement of gear shaft at pitch circle, unit: m.
S_w	Peripheral displacement of worm shaft at pitch circle, unit: m.

Chapter 1

Objective and motivation

1.1 Mechatronic system

The term “Mechatronics” was first introduced by an electric company in Japan, Yasakawa[1, 2]. The term itself is a combination of “Mecha” from mechanics and “tronics” from electronics. The definition of mechatronics has not stopped evolving since its first appearance. The books[3, 4] from Robert H. Bishop have traced its evolution. The concept of integration [5] appears quite often in more recent proposals of definitions, see [6, 7, 8].However, a consensus has not yet reached, but it is commonly accepted that mechatronics is an integration of several sciences and it is more than a simple combination.

In a narrow sense, mechatronics is in the overlapping area of mechanics, electronics and information technology[9], in figure 1.1. An extended representation in the papers [10, 11, 12] shows that mechatronics is the synergistic integration of physical systems, electronics, controls and computers. Publications and papers, see e.g. [13, 14, 15, 16, 17], demonstrate the similar imagination of mechatronic systems structure.

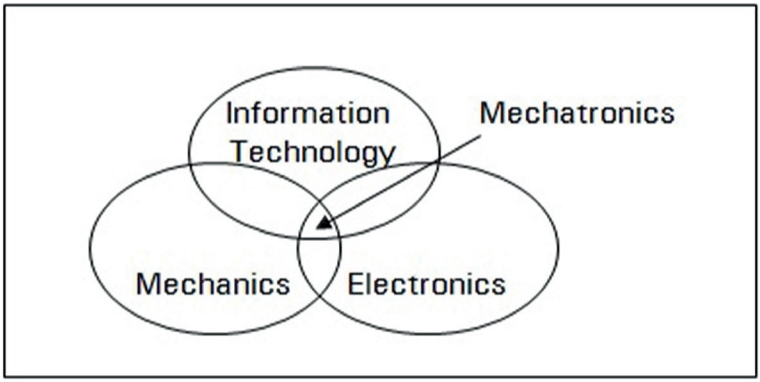

Figure 1.1: Mechatronics

The nature of mechatronics is multidisciplinary.[18]. Resulted from its nature, machatronic systems have unique properties , in comparison with other systems dealing with only single science. For example, these properties are high–degree integration of components from different fields and being critical to optimize overall system performance across a broad rang of system parameters[19]. Based on increasingly improved understanding, more mechatronic systems are invented with various functions. One instance of classical mechatronic systems is robot[20]. In automobile industry, many mechatronic systems are developed. They provide intelligent functions. Such system are like new braking and suspension system[21, 22]. It is expected that more novel applications will be brought forward, as mechatronics develops.

1.2 Development methods of mechatronic systems

Since the appearance of “Mechatronics”, the development of mechatronic systems has been fueled by the growth from the constituent areas. In the other way round, the developments in the constituent areas are also accelerated by mechatronics. Meanwhile more and more

new technologies are entering mechatronics. Under such circumstance, mechatronic systems need a suitable development approach. It is beyond the power of the traditional development methods used in individual fields. In search of an approach, Modeling and simulation (M&S) gain more and more attention and are being used widely in applications of mechatronic systems developments.

1.2.1 Development methods

The traditional sequential development strategy doesn't represent ideal structure to develop components of an modern mechatronic system [23, 24, 25]. Nowadays concurrent engineering [25] is popular and accepted in industrial applications.

In a narrow sense, concurrent implementations are developments of components in one or several sub technologies with consideration of components in another or other sub technologies. An example is that passive suspensions of passenger cars. The pure mechanical devices are integrated with electronics and controls. Then it becomes active systems and increases driving comfort[26]. Such kind of concurrent strategy works without problem as well in other combinations of components. Generally in such systems, one part is taking dominating role in system development, while other parts are loosely attached. Theses applications are limited in a small scale.

In large scale of applications, amount and complexity of components increase dramatically. Components or modules are developed firstly in each specific field with existing and well-formed methods and then focus of system development shifts to proper interfaces in between [27, 4].

In a wider sense of concurrent development strategy, mechatronic systems design[28, 4] provides a better solution. Mechatronic system design means designing and developing on system level. Publications [29, 30] have brought insights on this approach. In using system approach to develop mechatronic systems, M&S is the key technology for success. For the use and application of M&S, association of german

engineers(VDI) issues also their design methodolgy for mechatronic systems, VDI 2206[31]. In the deign guideline, the development activities begin with the analysis of system request and are followed by system draft. With the domain specific development finished, system is integrated and tested to ensure required product properties released.

1.2.2 Modeling and simulation

The technology boom of the 1990s enables the wide usage of models and simulations, which was once a tool for training military, now in almost every aspect of life[32, 33, 34]. The fundamental notion at the core of M&S is that models are approximations of the real world[35]. Plenty of books have been published regarding M&S as a discipline[36, 37, 38].

Table 1.1: Modeling and simulation

Simulation	Fields	Method	Application
Component	Mechanics	Finite Element Method	ANSYS®
		Multi Body Simulation	Adams®
	Electronics	Circuit analysis	PSpice®
	Control	Signal flow	MatLab SimuLink®
Cooperative	Mechanics Electronics Control	Functional Mock-up	Modelisar
System	Mechanics Electronics Control	Modeling language	VHDL-AMS Modelica

In the context of mechatronic system developments, M&S play an important role[39, 40, 41, 42, 4], because it can best cope with the multidisciplinary nature of mechatronics. It is well exploited in constituent technologies. It is also used to study the interactions of interfacing components. The advantage of M&S is that it helps with a better overview of design processes and it brings into being a seamless concurrent development of mechatronic systems.

1.3 Electrical power window regulator

Modern electrical power Window regulator (WR) in automobile industry[43, 44] is one of the classical examples of mechatronic systems. WR, or in another word "window lift", evolves through phases, from manual system at the beginning, then power system as the development of electrical motors until nowadays electrical power system with safety and comfort functions. Modern WR incorporate mechanical structures as power transmission, electrical drives as actuator, sensor to observe system states and electronics together with intelligent controlling software. Electrical WRs are mechatronic systems, because they are multidisciplinary. Its development needs an approach, which is not found in traditional development methods.

1.4 Objectives and structure of the thesis

This work contributes to the development of electrical WR with use of the technology of M&S. Requests in automobile industry have brought more and more challenges to system suppliers. Development cycle is shorter, customer requirement becomes more, qualities are to be ensured and improved to higher level and so on. Under such situation, market players have to be able to respond more quickly to requests. The technology of model and simulation is about to help. In this work, a development of models of WRs and simulations is presented. It is expected to reach the following general goals.

- An assisting tool, to improve understanding of systems and provide a perspective to observe systems in development processes
- Early error detecting, to cut down cost and effort costed by design mistakes in later development phases
- Validation of system functions based on simulations
- System behavior prediction, to find out critical and weak points in systems at early development phases

The thesis is organized as in Fig. 1.2. Following chapter 1 and 2, electrical WR systems are explored by analytical investigation in chaper 3 and by M&S in chapter 4 and 5. In chapter 4, WR is firstly broken down to its marco mechatronic models and then each component is modeled. Chapter 5 makes use of mechatronic models in chapter 4 and builds up simulations of WR. In Fig. 1.3, stucture of chpater 4 and 5 is presented.

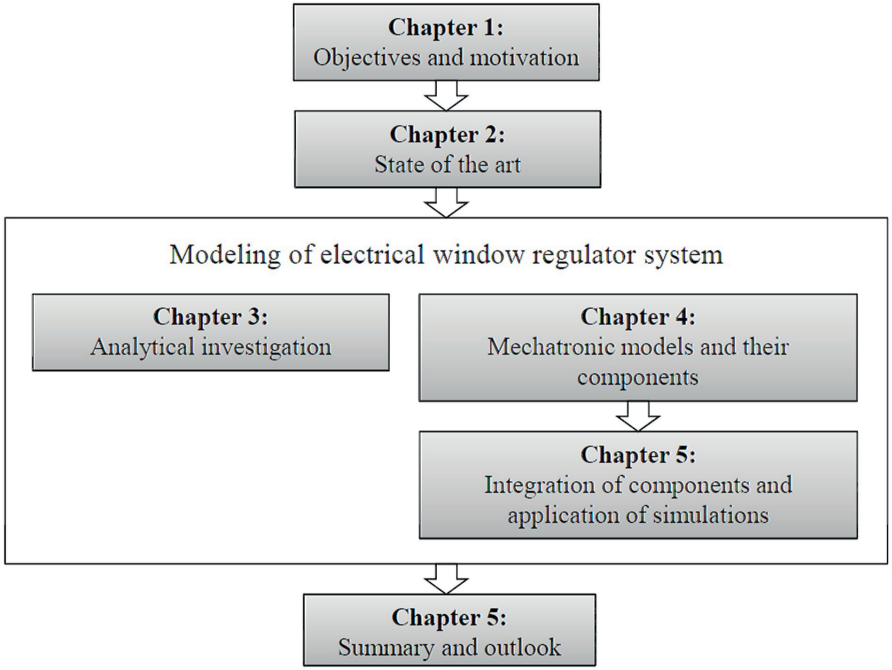

Figure 1.2: Structure of the thesis

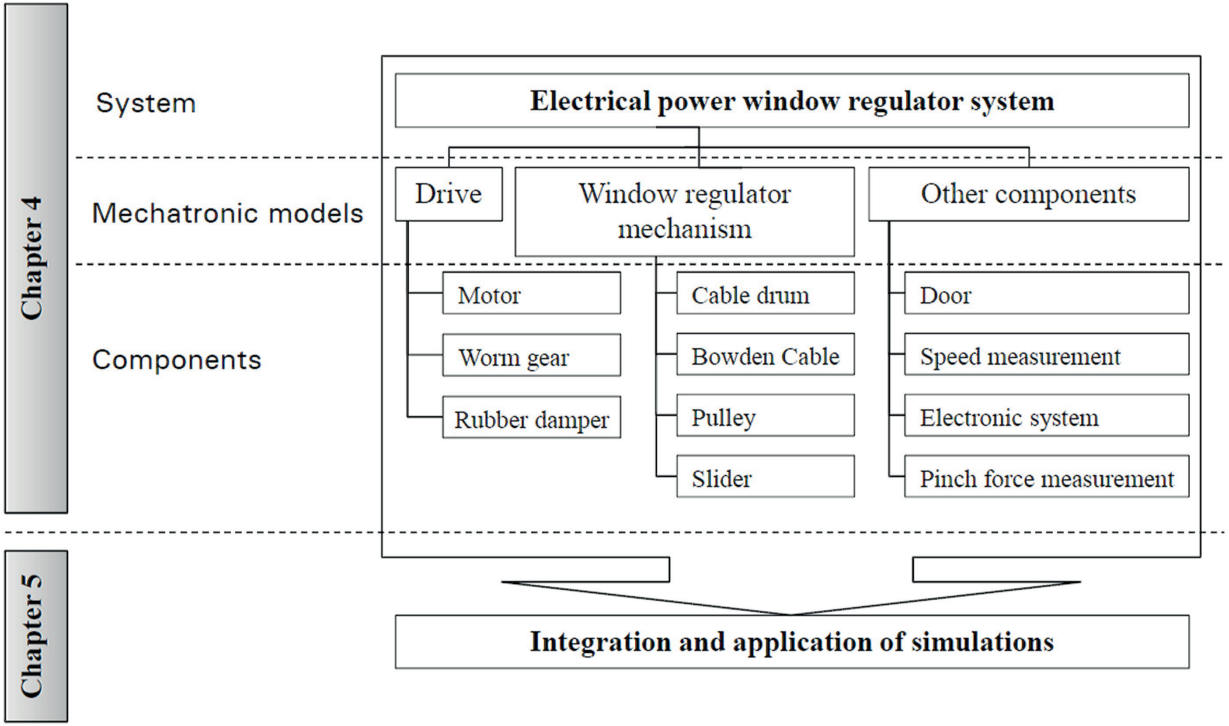

Figure 1.3: Structure of the thesis

Chapter 2

State of the art

2.1 State of the art – window regulator systems

Since the emergence of automobiles, WRs are continually further developped. Nowadays there are three types of WR mechanisms widely used in vehicle door, rail guided cable driven WR[45, 46, 47, 48, 49, 50], cross arm WR[51, 52] and track guided cable driven WR.

2.1.1 Rail guided cable driven window regulators

The rail guided cable driven mechanism is currently mainstream for WR structure. The structure and components are shown in Fig. 2.1. Electrical drive is actuator and can be replaced by a handle in manual applications. Inside of cable drum housing, the inner side of cable drum clutches with electrical or manual drive and the outer side of cable drum is wrapped with cable. Cable goes through bowden cable and changes its driving direction by wrapping around pulleys. Pulleys are loosely riveted on metal guiding rails and rails are aligned in glass moving direction. In the shown case, glass is held by two pieces of sliders and sliders, wrapped over rails, is pulled by cable either upwards or downwards. The component marked with number 3 is to compensate the prolongation of cable over lifetime. Depending on vehicle door designs,

rail guided WRs have several variants. For example, depending on the number of rails, there are double rail and single rail systems; by number of bowden cables, there are bowden and non-bowden systems. Many factors influence the choice of window regulator structures in projects, such as size of glass and door, rang of glass movement, components distribution on door plate and so on.

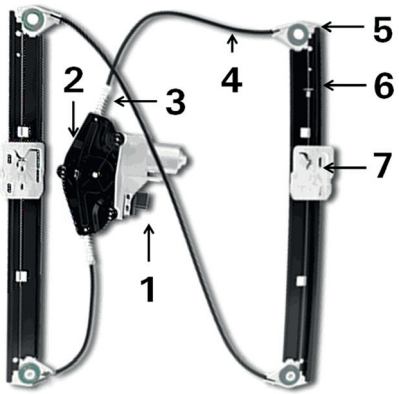

Figure 2.1: Double rail guided cable driven WR. 1. Electrical drive and electronics, 2. Cable drum housing, 3. Compensation spring, 4. Bowden cable and cable, 5. Pulley, 6. Guiding rail, 7. Glass slider

2.1.2 Crossarm window regulators

Cross arm mechanism is traditional design of WR. It contains parts in Fig. 2.2. Electrical drive is the same in rail systems. Tooth segment serve as movement transmission mechanics from drive to driving arm. Supporting arm provides a second point to stabilize the glass level in moving direction. The fundamental principle of cross arm mechanism is lever effect. Supporting arm may be omit in applications, that glass movement is already quite stable through door sealings and frames. Other variants can be at the layout of pinions, with the purpose to make maximal use of driving power.

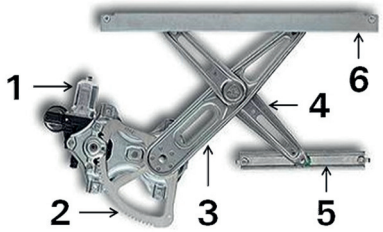

Figure 2.2: Cross arm WR. 1. Electrical drive and electronics, 2. Tooth segment, 3. Driving arm(Main arm), 4. Supporting arm(sub arm), 5. Supporting rail 6. Main rail(Glass rail)

2.1.3 Track guided window regulators

Track guided WRs are used mostly in rear side–window in coupés and convertibles, which require complex movements. In these applications, glass movement is not translational along A pillar and B pillar but it is a combination of translational and rotational movement. To achieve control of movement, glass carrier is pulled by cable and three rollers of carrier are guided in tracks with different path and length.

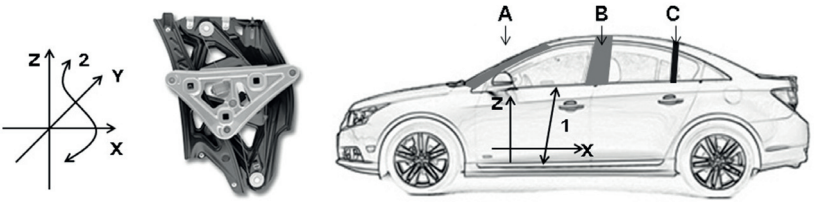

Figure 2.3: Track guided WR 1. Movement of glass with rail WR in sedan 2. Movement of glass with track guided WR

2.1.4 Comparison of window regulators

From the perspective of usage and applications, track guided WRs are used less often than rail guided and cross arm WRs, because the design of door glass in vehicles are usually straightforward, that is, translational upwards and downwards moving. Rail WRs and arm WRs are

widely implemented in car doors. Arm WRs are cost–efficient solutions. But, with the development of productions, rail WRs are becoming cheaper and cheaper. Under constant load applied from car door to WR mechanism, rail structure can theoretically supply a constant glass speed, while glass speed with arm structure will be lower at bottom and at top than in the middle position, due to the nature of lever effect. From another aspect, rail WRs have generally a better acoustic performance. Careless treatment at metal contact in arm WR may result to auditory discomfort. Arm WR itself is heavier than rail WR, which does not fit for the increasing strict requirement of system weight. From this point of view, rail WR is taking a leading position.

2.2 State of the art – simulation methods of window regulator systems

2.2.1 State of the art

Simulation is utilized widely in automobile industry, in vehicle manufacturers and also in suppliers. But, within the whole industry, a complete standard for components and systems simulation does not exist. Each manufacturer makes simulations based on its own understanding of problems and its own requirements. So it is the same with WR simulation. Window regulators system suppliers or components suppliers may choose simulation tools and solutions based on its knowledge and viewpoints. As to the number of WR system suppliers, who make use of simulation during development, a few examples are presented here to illustrate the state of the art of WR system simulations.

Under the link[1], it is the simulation interface from KOSTAL GmbH & Co. KG. It simulates the anti-pinch functionality and durability of the electronic control unit under rough road condition. Statistic simulation is carried out to test robustness of anti–trap algorithms. As the product focus of KOSTAL is electronics, so the goal of simulation is to validate

[1] see at http://www.kostal.com/german/HILwindow.htm

the functions of electronics and such simulation concept is executed based on HIL (Hardware In the Loop), which means that information regarding situations of rough road, car variants and door construction are all input from a black box.

Another approach to simulation WRss is co–simulation, which stands for cooperative simulation. Co–simulation makes use of two or more simulators to fulfill simulation tasks, in aim to explore the strength of different simulators and also to deal with complicated calculation. The paper[53] demonstrated such idea, with co–simulation of Dymola®, an implementation of modeling language Modelica, and Simulink®. In the environment of Dymola®, electrical drive, window regulator mechanism, vehicle door and control sequences are described. At the interface, information, like motor voltage, current, signal from Hall sensor and pinching force, is transferred into Simulink®, in which window regulator control and anti-pinch algorithms are implemented. In this case, simulation exploits the advantage of Simulink® in control and algorithm design and the strength of Modelica as a modeling language for physical systems.

Brose GmbH & Co. KG uses simulation technology to investigate dynamical property and behaviors of its window regulator systems. The technical demand is that reaction time for pinch detection is between 10ms and 50ms. The concept of co–simulation was also implemented and realized, beginning from 2005 and ending in 2007. The cooperation was between Adams® and Simulink®.

As shown in Fig. 2.4, the simulation has a straightforward demonstration of WR systems, based on three dimensional (3D) model in Adams®. Simulation of anti-pinch function and control algorithms is led by Simulink® and the simulation result of anti–pinch force is shown on the right side of Fig. 2.4.

The practices of simulating WR components and systems above have their advantages. However, the drawbacks are also obvious. The HIL simulation of control unit from KOSTAL tested only the robustness

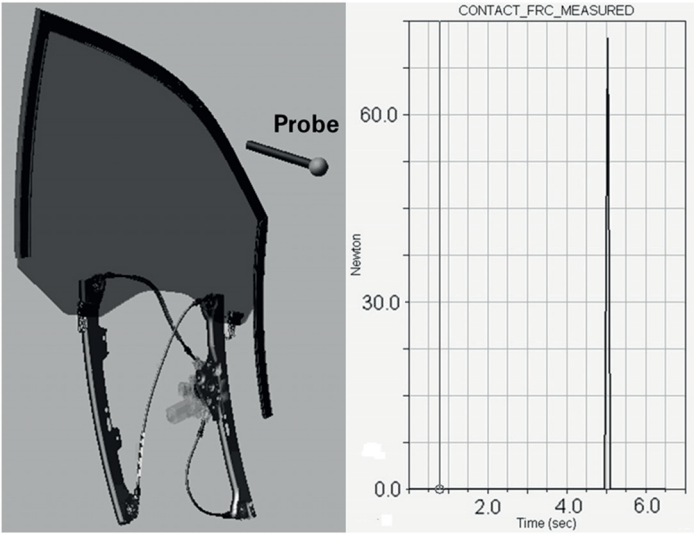

Figure 2.4: Co-Simulation at Brose. Step 1: glass moves down. Step 2: Probe moves between door frame and glass. Step 3: glass moves up. Step 4: glass edge hits probe, contact force is measured by probe and glass reverses.

of the electronic components and performance of algorithms, because KOSTAL is an electronic component suppler and does not have the technical understanding on a system level. The co–simulation practice in paper[53] supplemented the mechanical components of WR systems, as well as Brose co–simulation. While the power of different simulators are well used, the price has to pay for the design of interfaces in between. The more special one simulator is in its field, the more difficult a proper interface is built to communicate with others. Modelica is still growing and the number of components in its built-in library is not enough for a quick construction of mechatronic system simulations. In spite of the advantage of visualization, Adams® simulations in Brose has its problem that the effort involved in building simulation takes too much. 3D model of WR is available in design and construction department. But such data has to be processed manually to fit usage in Adams®, such as meshing, material stress, damping factor, stiffness and so on. Even

if the cost of time to adapt algorithms in Simulink® is neglected, the total cost of time and effort is still too much and the direct consequence is that the simulation falls behind the development schedule of on-going projects, which turns out that the value of such kind of simulation is not attractive any more.

Table 2.1: Comparison of methods to simulate window regulators

Method	User	Advantage	Disadvantage
HIL (Hardware in Loop)	KOSTAL	Functions of electronic component are tested and validated	Proof of compatibility with other components in WR is poor.
Co-simulation Dymola & SimuLink	Hella	Interaction between physical behaviors and controlling processes is simulated	design of interface between simulators costs much effort.
Co-simulation Adams & SimuLink	Brose	Good visualization	Adjusting 3D model in Adam® costs much time.

2.2.2 Requirements to simulations of window regulator systems

A systematic approach is needed for simulation of electrical power WR system. Based on the last section, it is summarized that simulation of WR systems needs a system method, namely system simulation. The term of system simulation appears quite often in automobile development[54, 55, 56]. Since years ago, Dr. Sergy Petkun from Brose investigated also in this direction[57, 58, 59]. System simulation means to simulate the composition of system components in a synergistic way. In the case of WR simulation, focus is equally on both the simulation of single components and the interfaces in between. The distribution of effort in describing component models should be well maintained in the way that no single model is too deeply modeled and other models

become relatively weak and shallow in systems. A short summary of requirements on system simulation is listed below, based on the practices in Brose.

- System simulation must provide a good system overview
- Time and effort efficiency in simulation preparation
- Enough detailedness of simulation components description and sufficient parameters as most significant factors of system properties
- Simulation result should contain the most information for a quick judgement, whether systems meet requirements or not. But such information should not be too much, which may lead analysis of result to be disordered.

2.3 System approach

Modeling and simulation are playing an active role in development of mechatronic systems. Among different strategies of M&S, we choose system simulation. The reason is that system simulation provides means to understand and predict behaviors of mechatronic systems. And it is especially useful in the case of electrical power window regulator systems.

2.3.1 System simulation

System simulation has unique features, comparing with component simulation. A short comparison is in Tab. 2.2. An example to the point of parameters in Tab. 2.2 is the simulation of frictional torque between shaft and bearing. In principle, it can be calculated with known pressing force, shaft diameter and friction coefficient. However, in a 3D simulation environment of bearing, besides the previous three parameters, length, width and height of bearing have to be given. But, they do not have a direct effect on frictional torque.

Table 2.2: System simulation and component simulation

Aspect	System simulation	Component simulation
Focus	Resultant system behaviors of interaction between components from different domains	Respond of components to its stimulus in specific field
Modeling	High level of abstraction of real system	Deep modeling into device level
Parameters	Parameters have essential influence on system behaviors	Part of parameters are necessary to build up models but have little influence on component functions.

In this work, system simulation is chosen as approach. The reasons are based on technical requests.

1. Modeling building must be up to the pace of product development.
2. Characteristic parameters must be within limited set and can be identified without much effort.
3. It must be easy for non–simulation–developer end user to understand and use simulations.

System simulation of electrical WR is based on models of its constituent components, which are described in unified modeling language. Each model of component is characteristic with its featured parameters, including electrical, geometrical and dynamical ones. The process of parametrization enables the fast adaption and reusability of models to fit into the needs of new projects.

2.3.2 Modeling language and simulation engine

Purposes determine choices of simulation tools and proper tools accelerate simulations. On market, there are already plenty of simulation software. A type of them, with an example of PSpice[60], provides users with build-in libraries of components and users need only to drag components into the simulation container and interconnect them to build up

simulations. Library of components can be extent by importing external packages. This kind of simulations is quite famous in component simulation for a specific area. Besides of build-in library, other simulation software, like SimuLink® [61], provide possibility to run scripts, which can describe non-existing behaviors of certain components. Instead of scripting language, Synopsys® Saber®[62, 63] provides uniformed modeling language MAST, which can model components in various domains. But MAST is bound to Saber, which limits the wide acceptance.

In this work, VHDL–Analog and Mixed Signal (VHDL–AMS)[64, 65, 66] is selected to be modeling language. VHDL–AMS extends the modeling language of VHSIC Hardware Description Language (VHDL)[67, 68], with the capability to model analog and mixed-signal systems. Analog and mixed-signal systems cover analog circuit, mechanical devices, hydraulic devices, optical systems and other physical systems. VHDL–AMS is chosen based on the reasons.

1. VHDL–AMS, as a uniformed modeling language, fits to the idea of system simulation. It takes care of components, interfaces and meanwhile behaviors at system level. However, it provides also the possibility for detailed modeling. Users have freedom to describe subjects or processes in detailedness based on their demands with the power of multi–domain modeling language.
2. It is easier to maintain models in one modeling language than switching from one to another, since each modeling language has its technical focus.
3. VHDL–AMS is widely accepted international standard. Numbers of model package and simulator are available on market.

This work adopts Synopsys® Saber® as simulation engine. Referring to the feature of modeling language, a quick switch to another engine is possible.

2.4 System decomposition and steps in using modeling and simulation

2.4.1 System decomposition

The performance of window regulators should be tested in car doors. Figure 2.5 shows that rail window regulator is mounted in car door. And, to the purpose to test safety functionality, a force gauge is also necessary. It is not shown in Fig.. A vehicle door system can be decomposited into macro models, as shown in Tab. 2.3. The decomposition is based on domains, functions and interfaces. The interconnection of marco components is presented in Fig. 2.6.

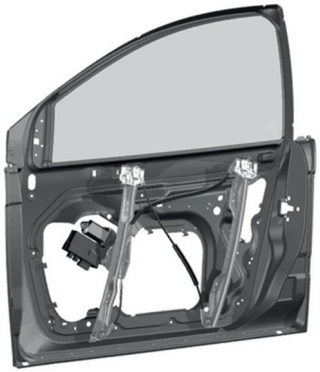

Figure 2.5: Vehicle door system

The decomposition of system fits to the development process in house of Brose. The number of interfaces between components is optimized and a straightforward correspondence between real systems and simulation systems can be built. Macro models in table are built up with sub models. The doctor work investigates macro models and their sub models.

Table 2.3: Decomposition of window regulator systems

Index	Macro models
1	Drive
2	Window regulator mechanism
3	Door
4	Anti-pinch spring
5	Electronic hardware
6	Software
7	Switch (Control Sequence)
8	Battery

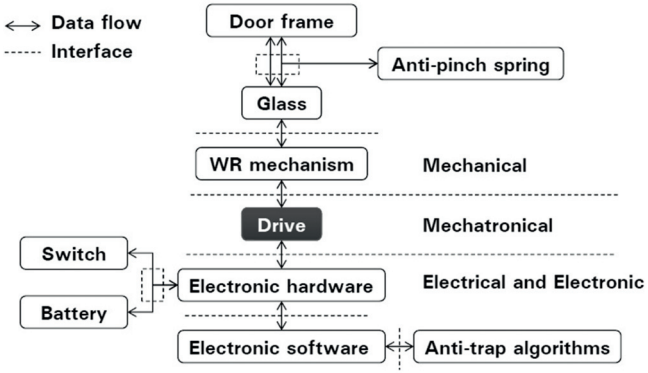

Figure 2.6: Macro models and interfaces

2.4.2 Steps in using modeling & simulation

The fundamental, more like a philosophy, is that it is impossible to create perfect simulations and models to 100% represent reality. Normally M&S are used to describe a slide of reality. The result of simulations can approach reality by infinitely improving the quality of models. However, the goal is not simply to make simulations but to make simulations and models in order to bring insights.[69].

To achieve an effective usage of simulation, steps have to be taken. The processes of M&S [70, 71, 72] are required to go through steps, in Fig. 2.7. In the first step, it is important that a clear target is set and criteria of result evaluation is defined. The practical outcome can be

either concepts in minds or specifications in written forms. The actions of M&S verification and validation ensure that simulation objects are right modeled and right models are found.

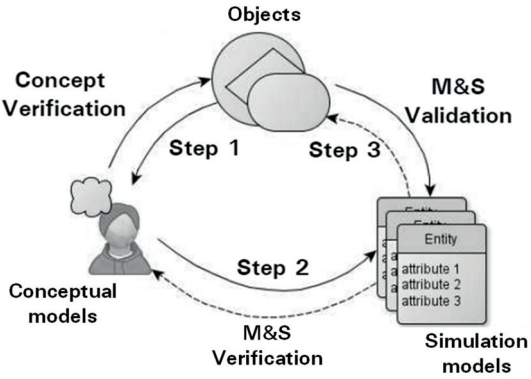

Figure 2.7: Modeling and simulation. Step 1: Simulation objects to conceptual models, associated with concept verification, Step 2: Conceptual models to simulation models, associated with M&S verification, Step 3: Compare simulation models to Simulation objects, associated with M&S validation

The work of this thesis complies with the required steps in using M&S, as described above. Specifically, they are

1. Mathematical models
2. Implement mechatronic models in VHDL–AMS
3. Parameter identification
4. Compare simulation verse measurements.

For the most, mathematical models are provided as conceptual models. VHDL models are implementations of concepts. Parameter identification process finds reliable values of parameters for models. Comparing simulations with measurements serves as validation. During comparison, causes of differences are searched and reasons are discussed.

Chapter 3

Modeling of electrical window regulator system - Analytical investigation

3.1 Modeling and simulation of the behavior of analytical model

3.1.1 Analytical model

Mechanical door in Fig 2.5 and WR mechanism 2.1 have many components, yet the analytical model of WR system is abstracted to contain only the essential parts as in Fig. 3.1. M_1 is the equivalent mass of armature inertia and F_a is the equivalent driving force of motor[73]. The spring and damper stand for the important characteristic of WR system, system stiffness c and damping factor μ. M_2 represents the glass mass and F_r is the friction force between glass and door sealings. x_1^* and x_2^* indicate each the displacement of M_1 and M_2.

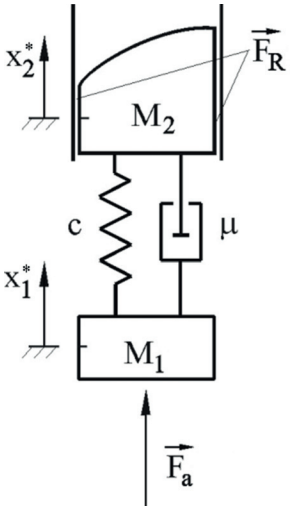

Figure 3.1: Analytical model of window regulator system

Many components of a WR system, like double rail WR, have masses and moment of inertia, such as cable, pulley, cable drum, gear of electrical drive and so on. Quantitatively, their inertia are either small or big. But only glass mass and moment of inertia of armature are taken into account in analytical model. The reason is kinetic energy. When electrical drive moves window glass, motor armature and glass have the most kinetic energy of the whole system. Kinetic energy of other components is not comparable. Therefore, no other components but only these two parts are considered in model.

Table 3.1: Kinetic energy of components

Component	Mass/Moment of Inertia	Velocity	Kinetic energy
Armature	$9.9 \times 10^{-06}\,\mathrm{kg} \cdot \mathrm{m}^2$	$398\,\mathrm{rad/s}$	$0.7848\,\mathrm{J}$
Wheel	$12 \times 10^{-06}\,\mathrm{kg} \cdot \mathrm{m}^2$	$5.4\,\mathrm{rad/s}$	$0.186 \times 10^{-03}\,\mathrm{J}$
Drum	$4.9 \times 10^{-06}\,\mathrm{kg} \cdot \mathrm{m}^2$	$5.4\,\mathrm{rad/s}$	$0.073 \times 10^{-03}\,\mathrm{J}$
Pulley	$2 \times 10^{-06}\,\mathrm{kg} \cdot \mathrm{m}^2$	$5.4\,\mathrm{rad/s}$	$0.036 \times 10^{-03}\,\mathrm{J}$
Cable	$0.5\,\mathrm{kg} \cdot \mathrm{m}^2$	$0.12\,\mathrm{m/s}$	$0.0037\,\mathrm{J}$
Glass	$5\,\mathrm{kg}$	$0.12\,\mathrm{m/s}$	$0.036\,\mathrm{J}$

The model in Fig. 3.1 is applied with the Newton's second law, each M_1 and M_2, resulting analytical description in Eq. 3.1.

$$M_1\ddot{x}_1^* + c(x_1^* - x_2^*) + \mu(\dot{x}_1^* - \dot{x}_2^*) = F_a \tag{3.1a}$$
$$M_2\ddot{x}_2^* + c(x_2^* - x_1^*) + \mu(\dot{x}_2^* - \dot{x}_1^*) = F_r \tag{3.1b}$$

The purpose of this model is to study dynamical behavior of WR under various working cases. So, F_a and F_r are given different forms. In the following sections, method of averaging will be put into use to analyze two dynamical cases.

3.1.2 Theoretical investigations - Method of averaging

3.1.2.1 Friction depending on relative velocity

In this case, the direction of friction depends on the relative velocity between glass and motor armature. It then has the form as $-F_r sgn(\dot{x}_2^* - \dot{x}_1^*)$, where $(\dot{x}_2^* - \dot{x}_1^*) \neq 0$ and F_r is the amplitude of friction force. The driving force of electrical motor is a harmonic function on time with angular frequency ω and an amplitude F_a [74]. The general description of model in Eq. 3.1 is instantiated as following.

$$M_1\ddot{x}_1^* + c(x_1^* - x_2^*) + \mu(\dot{x}_1^* - \dot{x}_2^*) = F_a \sin(\omega t^*) \tag{3.2a}$$
$$M_2\ddot{x}_2^* + c(x_2^* - x_1^*) + \mu(\dot{x}_2^* - \dot{x}_1^*) = -F_r sgn(\dot{x}_2^* - \dot{x}_1^*) \tag{3.2b}$$

As the next step, the dimensional system (denoted by asterisk) is converted into a dimentionless system, by introducing dimensionless variables and converting scales. $t = t^*\omega_0$, $x_i = \frac{x_i^*}{L}, i = 1, 2$, $\dot{x}_i = \frac{\dot{x}_i^*}{L\cdot\omega_0}, i = 1, 2$, $\ddot{x}_i = \frac{\ddot{x}_i^*}{L\cdot\omega_0^2}, i = 1, 2$, $\omega_0^2 = c\frac{M_1+M_2}{2M_1M_2}$, $\nu = \frac{\omega}{\omega_0}$, $\varepsilon = \frac{F_r}{ML\omega_0^2}$, $\alpha = \frac{\mu L\omega_0}{F_r m_1 m_2}$, $\beta = \frac{F_a}{F_r}$, $m_1 = \frac{M_1}{M}$, $m_2 = \frac{M_2}{M}$, $M = M_1 + M_2$, $m_1 + m_2 = 1$. Here, L is the scale of length, while ω_0 is the scale of time. Substituting variables in equations above gives dimensionless system as following.

$$\ddot{x}_1 + 2m_2(x_1 - x_2) + m_2\varepsilon\alpha(\dot{x}_1 - \dot{x}_2) = \frac{\varepsilon}{m_1}\beta\sin(\nu t) \tag{3.3a}$$

$$\ddot{x}_2 + 2m_1(x_2 - x_1) + m_1\varepsilon\alpha(\dot{x}_2 - \dot{x}_1) = -\frac{\varepsilon}{m_2}sgn(\dot{x}_2 - \dot{x}_1) \tag{3.3b}$$

The method of averaging [75] requires that the system should be transformed into standard form. The operation, 3.3a$\cdot\, m_1 +$ 3.3b$\cdot\, m_2$, results into Eq. 3.4a. The second operation, 3.3b $-$ 3.3a, gives Eq. **??**.

$$m_2\ddot{x}_2 + m_1\ddot{x}_1 = \varepsilon[\beta\sin(\nu t) - sgn(\dot{x}_2 - \dot{x}_1)] \tag{3.4a}$$

$$(\ddot{x}_2 - \ddot{x}_1) + 2(x_2 - x_1) = \tag{3.4b}$$

$$-\varepsilon\left[\frac{1}{m_2}sgn(\dot{x}_2 - \dot{x}_1) + \alpha(\dot{x}_2 - \dot{x}_1) + \beta\frac{1}{m_1}\sin(\nu t)\right]$$

Further simplification can be achieved by introducing velocity of center of mass, $V(t) = m_1\dot{x_1} + m_2\dot{x_2}$, and relative displacement, $z(t) = x_2 - x_1$, into system.

$$\dot{V} = \varepsilon[\beta\sin(\nu t) - sgn(\dot{z})] \tag{3.5a}$$

$$\ddot{z} + 2z = -\varepsilon\left[\frac{1}{m_2}sgn(\dot{z}) + \alpha\dot{z} + \beta\frac{1}{m_1}\sin(\nu t)\right] \tag{3.5b}$$

For unperturbed system, ν in 3.5b is equal to constant, $z(t) = x_2 - x_1$ changes harmonically with a constant amplitude. According to it, a general solution is provided to Eq. 3.5b in the form: $z(t) = a(t)\cos(\varphi)$ and $\dot{z} = -a\sqrt{2}\sin(\varphi)$, where $\varphi = \sqrt{2}t + \theta$. Then,

$$\dot{z} = \dot{a}\cos(\varphi) - a(\sqrt{2} + \dot{\theta})\sin(\varphi) \tag{3.6}$$

It yields

$$\dot{\theta} = \frac{\dot{a}\cos(\varphi)}{a\sin(\varphi)} \tag{3.7}$$

The general solution and the relation 3.7 are applied to 3.6. The system has then the form.

$$\dot{V} = \varepsilon[\beta \sin(\nu t) - sgn(-a\sqrt{2}\sin(\varphi))] \tag{3.8a}$$

$$\dot{a} = \varepsilon \frac{\sin(\varphi)}{\sqrt{2}} \left[\frac{1}{m_2} sgn(-a\sqrt{2}\sin(\varphi)) - \alpha a \sqrt{2}\sin(\varphi) + \beta \frac{1}{m_1}\sin(\nu t) \right] \tag{3.8b}$$

$$\begin{aligned} \dot{\varphi} &= \dot{a} + \sqrt{2} \\ &= \varepsilon \frac{\cos(\varphi)}{\sqrt{2}a} \left[\frac{1}{m_2} sgn(-a\sqrt{2}\sin(\varphi)) - \alpha a \sqrt{2}\sin(\varphi) + \beta \frac{1}{m_1}\sin(\nu t) \right] \\ &+ \sqrt{2} \end{aligned} \tag{3.8c}$$

The system behavior is investigated in the vicinity of the main resonance frequency: $\psi = (\sqrt{2} + \varepsilon\Delta)t$, $\nu = \sqrt{2} + \varepsilon\Delta$. Through introducing new slow variable $\xi = \psi - \varphi$, $\dot{\xi} = -\dot{\theta} + \varepsilon\Delta$, the standard form of the systme is:

$$\dot{V} = \varepsilon[\beta \sin(\xi + \varphi) - sgn(-a\sqrt{2}\sin(\varphi))] \tag{3.9a}$$

$$\dot{a} = \varepsilon \frac{\sin(\varphi)}{\sqrt{2}} \left[\frac{1}{m_2} sgn(-a\sqrt{2}\sin(\varphi)) - \alpha a \sqrt{2}\sin(\varphi) + \beta \frac{1}{m_1}\sin(\xi + \varphi) \right] \tag{3.9b}$$

$$\begin{aligned} \dot{\xi} = -\varepsilon \frac{\cos(\varphi)}{\sqrt{2}a} \cdot \\ \left[\frac{1}{m_2} sgn(-a\sqrt{2}\sin(\varphi)) - \alpha a \sqrt{2}\sin(\varphi) + \beta \frac{1}{m_1}\sin(\xi + \varphi) \right] + \varepsilon\Delta \end{aligned} \tag{3.9c}$$

When $\varepsilon \ll 1$, the variables V, a and ξ change slowly. According to the method of averaging[75], the procedure $\langle \cdots \rangle = \int_0^{2\pi} (\cdots) d\varphi$ is applied to these slow variables in Eq. 3.9. And the fast changing element is filtered out.

$$\dot{V} = 0 \tag{3.10a}$$

$$\dot{a} = -\varepsilon \frac{1}{\sqrt{2}} \left(\frac{1}{m_2} \frac{2}{\pi} + \alpha a \sqrt{2} \frac{1}{2} - \beta \frac{1}{m_1} \cos(\xi) \right) \tag{3.10b}$$

$$\dot{\xi} = -\dot{\theta} + \varepsilon\Delta = -\varepsilon \frac{1}{\sqrt{2}a} \left(\beta \frac{1}{m_1} \frac{1}{2} \sin(\xi) \right) + \varepsilon\Delta \tag{3.10c}$$

The stationary solution of the system of Eq. 3.10 is under searching. As $\dot{V} = 0$, the stationary amplitude of V depends on its initial value. a and ξ have stationary state, when $\dot{a} = 0$ and $\dot{\xi} = 0$. By eliminating $\cos(\xi)$ and $\sin(\xi)$ with $\cos(\xi)^2 + \sin(\xi)^2 = 1$, it yields

$$2m_1^2 m_2^2 \pi^2 (\alpha^2 + 4\Delta^2)\alpha^2 + 8\sqrt{2} m_1^2 m_2 \pi \alpha a + (16 m_1^2 - m_2^2 \pi^2 \beta^2) = 0 \tag{3.11}$$

A positive stationary amplitude exists under the restriction $\beta > \frac{4m_1}{\pi m_2}$. Thus, the stationary amplitude of a is

$$a = \frac{-4\sqrt{2} m_1 \alpha + \sqrt{2[m_2^2 \pi^2 \beta^2 (\alpha^2 + 4\Delta^2) - 64\Delta^2 m_1^2]}}{2 m_1 m_2 \pi (\alpha^2 + 4\Delta^2)} \tag{3.12}$$

3.1.2.2 Friction depending on velocity of mass M_2

In this case, the direction of friction force has dependence on the velocity of M_2. Friction forece is denoted by the form, $-F_r sgn(\dot{x_2^*})$. The driving force is the same as in the previous case. As a result, the instants of system equations are

$$M_1 \ddot{x}_1^* + c(x_1^* - x_2^*) + \mu(\dot{x}_1^* - \dot{x}_2^*) = F_a \sin(\omega t^*) \tag{3.13a}$$

$$M_2 \ddot{x}_2^* + c(x_2^* - x_1^*) + \mu(\dot{x}_2^* - \dot{x}_1^*) = -F_r sgn(\dot{x}_2^*) \tag{3.13b}$$

The same conversion from dimensional system to dimensionless system is applied. The same variables, velocity of center of mass and relative displacement, are introduced and utilized.

$$\dot{V} = \varepsilon[\beta \sin(\nu t) - sgn(\dot{x}_2)] \tag{3.14a}$$

$$\ddot{z} + 2z = -\varepsilon \left[\frac{1}{m_2} sgn(\dot{x}_2) + \alpha \dot{z} + \beta \frac{1}{m_1} \sin(\nu t) \right] \tag{3.14b}$$

As $m_1\dot{x_1} + m_2\dot{x_2} = V(t)$ and $\dot{z} = \dot{x_2} - \dot{x_1} = -a(t)\sin(\varphi)$, it can be deduced, $\dot{x}_2 = V - m_1 a\sqrt{2}\sin(\varphi)$. Then, with the same variable ξ, the standard form of system in this case is

$$\dot{V} = \varepsilon[\beta \sin(\xi + \varphi) - sgn(V - m_1 a\sqrt{2}\sin(\varphi))] \tag{3.15a}$$

$$\dot{a} = \varepsilon \frac{\sin(\varphi)}{\sqrt{2}} \cdot \left[\frac{1}{m_2} sgn(V - m_1 a\sqrt{2}\sin(\varphi)) - \alpha a\sqrt{2}\sin(\varphi) + \beta \frac{1}{m_1} \sin(\xi + \varphi) \right] \tag{3.15b}$$

$$\dot{\xi} = -\varepsilon \frac{\cos(\varphi)}{\sqrt{2}a} \cdot \left[\frac{1}{m_2} sgn(V - m_1 a\sqrt{2}\sin(\varphi)) - \alpha a\sqrt{2}\sin(\varphi) + \beta \frac{1}{m_1} \sin(\xi + \varphi) \right] + \varepsilon\Delta \tag{3.15c}$$

The procedure of averaging, $\langle \cdots \rangle = \int_0^{2\pi} (\cdots) d\varphi$, is applied. As outcome, slow variables have form.

$$\dot{V} = \begin{cases} \varepsilon, V < -m_1 a\sqrt{2} \\ \varepsilon \left[-\frac{2}{\pi} \arcsin\left(\frac{V}{m_1 a\sqrt{2}} \right) \right], |V| \leq m_1 a\sqrt{2} \\ -\varepsilon, V > m_1 a\sqrt{2} \end{cases} \tag{3.16}$$

$$\dot{a} = \begin{cases} -\varepsilon\frac{1}{\sqrt{2}}\left(\alpha a\sqrt{2}\frac{1}{2} - \beta\frac{1}{m_1}\frac{1}{2}\cos(\xi)\right), V < -m_1 a\sqrt{2} \\ -\varepsilon\frac{1}{\sqrt{2}}\left[\alpha a\sqrt{2}\frac{1}{2} + \frac{1}{m_2}\frac{2}{\pi}\sqrt{1-\frac{V^2}{2m_1^2a^2}} - \beta\frac{1}{m_1}\frac{1}{2}\cos(\xi)\right], \\ \qquad |V| \leq m_1 a\sqrt{2} \\ -\varepsilon\frac{1}{\sqrt{2}}\left(\alpha a\sqrt{2}\frac{1}{2} - \beta\frac{1}{m_1}\frac{1}{2}\cos(\xi)\right), V > m_1 a\sqrt{2} \end{cases} \quad (3.17)$$

$$\dot{\xi} = -\dot{\theta} + \varepsilon\Delta = -\varepsilon\frac{1}{\sqrt{2}a}\left(\beta\frac{1}{m_1}\frac{1}{2}\sin(\xi)\right) + \varepsilon\Delta \quad (3.18)$$

The stationary solution exists, only under the condition, $|V| \leq m_1 a\sqrt{2}$, because ε is not equal to zero. Eliminating $\cos\xi$ and $\sin\xi$ in Eq. 3.17 - 3.18 when $|V| \leq m_1 a\sqrt{2}$. We obtain the stationary amplitude of a, which is the same as in Eq. 3.12.

$$a = \frac{-4\sqrt{2}m_1\alpha + \sqrt{2[m_2^2\pi^2\beta^2(\alpha^2+4\Delta^2) - 64\Delta^2 m_1^2]}}{2m_1 m_2\pi(\alpha^2+4\Delta^2)} \quad (3.19)$$

It is found under the condition $\beta > \frac{4m_1}{\pi m_2}$.

3.1.2.3 Numerical simulations

To obtain a direct view of the behavior, the analytical model is simulated and solved numerically. The typical values for the model are $M_1 = 45\,\mathrm{kg}$, $M_2 = 5\,\mathrm{kg}$, $c = 2\times10^4\,\frac{\mathrm{N}}{\mathrm{m}}$ and $\mu = 80\frac{\mathrm{N}}{\mathrm{m/s}}$. The identification of M_1, c and μ is discussed in the next section. With given values, ω_0 is then equal to $47.1\,\mathrm{s}^{-1}$. In the case of relative friction, the driving force is assumed to be $F_a = 200N$ and $\omega = 75.8\,\mathrm{s}^{-1}$, while F_r is $10N$. Thus, $\beta = 20$, it meets the requirement $\beta > \frac{4m_1}{\pi m_2} = 11.5$. according to [76], the scale of length L is calculated by equation $\frac{F_a}{M_1\omega_0{}^2|2-\nu^2|}$. Then L has value of $3.3\times10^{-3}\,\mathrm{m}$. As consequence, $\varepsilon = 0.05$, $\alpha = 14.9$ and $\Delta = 4$.

Fig. 3.2 represents the exact and averaged system solved with initial condition,$V(0) = 0$, $a(0) = 0.01$, $\xi(0) = 0$. With supplied parameters, the stationary amplitude of a has value, 0.43, which is identical to the

calculation with formula in Eq. 3.12. The dimensional value of a is 1.4×10^{-3} m. The friction force in this model represents the friction because of the relative motion between masses M_1 and M_2, while the only external force is the periodic force, $F_a \sin(\omega t^*)$. Such model setup and forces combination simulate the rough road situation when testing WR system. When window regulator has no movement and car is driven on rough road, the vibrating car body results the periodic changing force. According to the definition of β and the system setup in the example, only when external force is at least 20 times greater than the "internal" friction force, there would be a slight relative displacement of two masses. As an example, when "internal" friction force is $50N$, at least $600N$ is required to produce position change. Actually, such change of the position difference is undesired in real system. And as a matter of fact, such great external vibrating force is unrealistic. Therefore, we can conclude, the more "internal" friction there is, the more stable WR system is in rough road test.

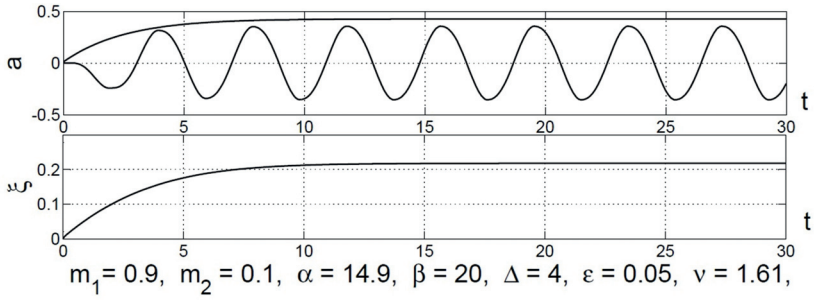

Figure 3.2: Numerical solution of exact 3.9 and average system 3.10

The system with "external" friction has the same system parameter set, M_1, M_2, c, μ, ω_0, ω, as the system with "internal" friction. Coulomb's dry friction force F_r is here 90N. The amplitude of the external driving force F_a, applied to mass M_1, is 1800N. Thus the value of β is 20 and meets the same condition as in the case of "internal" friction, because a in both cases has the same form. The scale of length L has value in this

case to be 3×10^{-2} m. The values $\varepsilon = 0.05$, $\alpha = 14.9$, and $\Delta = 4$ are also the same. Fig. 3.3 shows the results, after solving the exact and averaged system with initial condition, $V(0) = 0$, $a(0) = 0.01$, $\xi(0) = 0$. From the numerical solution of averaged equation, stationary a is 0.43, which is identical to the calculation in Eq. 3.19. The dimensional value of a here is 1.3×10^{-2} m. Such combination of periodic driving force and external friction force simulates the stability of WR system under disturbance from electrical drive. Electrical drive can supply an effective driving force up to 650N, when it is stalled. During the normal upward stroke, the driving force is around 250N. As the ambient condition changes, external friction can decrease dramatically, for example, when there is oil or grease between glass and sealing, when WR works in environment of high humidity, or when sealing wears out and ages. Then the vibration in electrical drive, which is usually caused by the irregularity of its gear transmission, can lead into the unstable moving speed of window glass. The instability can be troublesome in realizing anti-trap function; in extreme case it can cause failure, such as false reversing of WR.

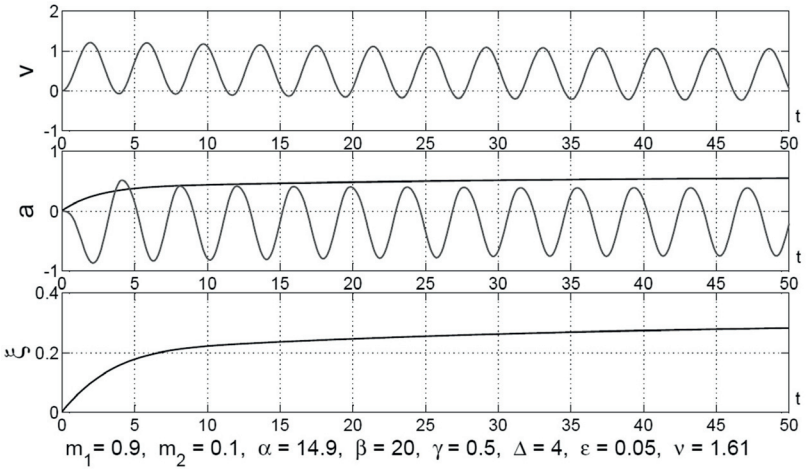

Figure 3.3: Numerical solution of the exact 3.15 and average system 3.16 - 3.18

3.2 Parameter identification – Equivalent mass of motor armature

M_1 in the analytical model is an equivalent mass of motor armature. The conversion from inertia of motor armature to mass is valid only under the precondition that the kinetic energy is kept the same. The flow of kinetic energy starts from rotating armature. It is then reduced through worm gear. In the end, it converts from rotational form into translational form. Therefore, the conversion of moment of inertia achieves in two steps. Step 1 is conversion over worm gear and step 2 is conversion over calbe drum.

To realize step 1, we define J_a as moment of inertia of armature, ω_a as rotational velocity of aramture, J_w as converted moment of inertia over worm gear and ω_w as rotational velocity of gear wheel. The mesh of worm gear is shown in Fig. 3.4.

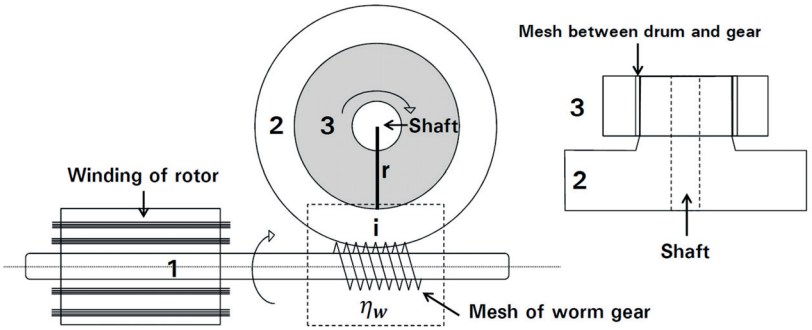

Figure 3.4: Conversion of moment of inertia into equivalent mass.
1: Armature of electrical drive, with complete winding. 2: Gear wheel. 3: Cable drum. i: Reduction ratio of worm gear. η_w: Power transmission efficiency

Worm gear is characteristic with parameters, i as reduction ratio and η_w as power transmission efficiency. Therefore, it gives

$$\eta_w \frac{1}{2} J_a \omega_a^2 = \frac{1}{2} J_w \omega_w^2 \tag{3.20a}$$

$$\omega_w = \frac{\omega_a}{i} \tag{3.20b}$$

Eliminate ω_w,

$$J_w = \eta_w \cdot i^2 \cdot J_a \tag{3.21}$$

In step 2, we define r_{cd} as radius of cable drum, V_1 as tangential speed of cable drum Then, energy equilibrium and velocity relation are

$$\frac{1}{2} J_w \omega_w^2 = \frac{1}{2} M_1 V_1^2 \tag{3.22a}$$

$$V_1 = r_{cd} \cdot \omega_w \tag{3.22b}$$

Eliminate V_1,

$$M_1 = \frac{J_w}{r_{cd}^2} \tag{3.23}$$

By eliminating J_w in Eq. 3.21 and 3.23, it yields

$$M_1 = \eta_w \frac{i^2 J_a}{r_{cd}^2} \tag{3.24}$$

A WR drive has typically inertia $8.0 \times 10^{-6}\,\mathrm{kg \cdot m^2}$, $i = 73$, $\eta_w = 0.42$ and $r_{cd} = 0.02\,\mathrm{m}$. Its equivalent mass is then, according to Eq. 3.24, about 45 kg. With this method, equivalent mass for analytical model in Fig. 3.1 can be calculated.

Chapter 4

Mechatronical models for window regulator systems and their components

4.1 Window regulator drive

Electrical drive is the key component in WR system. As shown in Fig. 2.6, drive connects WR mechanism and electrical components. It is source of lifting power and executes all control sequences. A WR drive consists of two parts. One part is Direct Current Permanent Magnet motor (DCPM motor) and the second part are worm gear and its housing, as shown in Fig. 4.1. In WR systems, the maximal torque of DCPM motor is in range from 0.3 Nm to 0.45 Nm. No–load speed can reach about 7000 rpm. Worm gear changes the rotation direction of motor armature into the desired direction of cable drum. Meanwhile, rotational speed is reduced to about 80 rpm and maximal torque of armature is amplified to be in range from 9 Nm to 13.75 Nm. Inside of worm gear wheel, there is in certain design rubber damper, which has the purpose

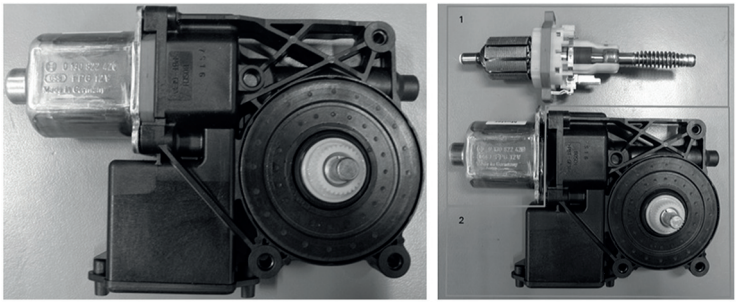

Figure 4.1: Window regulator drive and disassembly
1. DCPM motor 2. Worm gear and housing

to ease the tension in systems when glass hits door upper frame. This chapter is started with modeling of DCPM motor. Modeling processes consist of mathematical description, model and verification, parameter identification and validation. As followed, worm gear and rubber damper are modeled. At last, drive is modeled as an assembly of these three components.

4.1.1 DCPM motor

4.1.1.1 Mathematical description

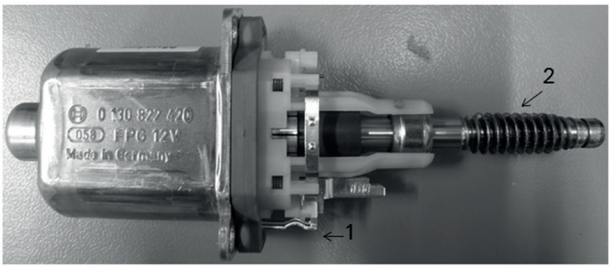

Figure 4.2: DCPM motor. 1. Electrodes 2. Shaft of armature

In Fig. 4.2, it is a DCPM brush motor. It transforms electrical energy into mechanical energy. Many books and papers have been published to descibe DCPM motor from different perspectives and in different level of accuracy [77, 78, 79, 80]. The mathematical description of DCPM

motor in this work builds up energy balance of Direct Current (DC) motor from electrical and mechanical characteristics. The equivalent electrical circuit of DCPM motor is shown in Fig. 4.3.

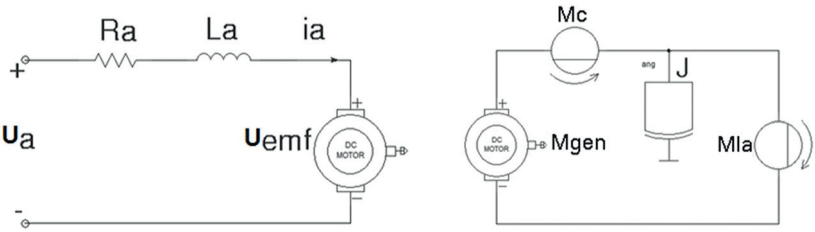

Figure 4.3: Equivalent circuit of DCPM motor

According to Kirchof's voltage law, electrical and mechanical balances are described

$$U_a = R_a \cdot i_a + L_a \cdot \frac{d}{dt} i_a + k_e \cdot \omega_a \tag{4.1a}$$

$$k_t \cdot i_a = M_c + Visc \cdot \omega_a + J_a \cdot \frac{d}{dt} \omega_a + M_{la} \tag{4.1b}$$

In equation 4.1, U_a and i_a are each the voltage across electrodes and the current through electrodes. ω_a is the rotational velocity of armature. M_{la} is the actual torque applied at armature. The rest of quantities are parameters for DCPM motor. Their definition and composition are listed in Tab. 4.1. These parameters are each simplified to represent certain properties of DCPM motor. For example, internal resistance of DCPM motor, R_a, abstracts resistive characteristic of winding, brush, commutator and brush voltage drop and leak current.

4.1.1.2 Mechatronic model and verification

The symbolic representation of DCPM motor in simulation is shown in Fig. 4.4. It has three pins as interfaces with other components. The two electrical pins are labelled with plus and minus signs. The last pin is the mechanical pin as shaft of armature. The voltage across electrical pins, U_a, is named in another way cross variable and the current flowing through the two pins, i_a, is through variable. Cross and through

Table 4.1: Parameter definitions of DCPM motor model

Parameter	Definition	Composition
R_a	Effective resistance	resistance of winding resistance of brush resistance of commutator voltage drop on brush leak current on brush ...
L_a	Effective inductance	inductance of winding inductance of brush inductance of commutator ...
k_e	Back EMF constant (Electromotive Force)	
k_t	Torque constant	
J_a	Effective inertia of rotor	inertia of winding inertia of commutator inertia of ring magnet ...
M_c	Coulomb friction	Mechanical friction loss at bearing Mechanical friction loss at brush and commutator
$Visc$	Viscous friction coefficient, damping constant	aerodynamic losses

variables are always associated to pins of different sciences. Base on the analogy [81, 82], similar idea is used in mechanical pins. In the case of mechanical translational movement, cross and through variables are displacement and force, or velocity and force. For rotational movement, they are angle and torque, or angular velocity and torque. In other sciences, like thermal dynamics and optics, cross and through variable are defined to simulate different physical effects[83]. The shaft of armature in DCPM motor model has angle as cross variable and torque as through variable.

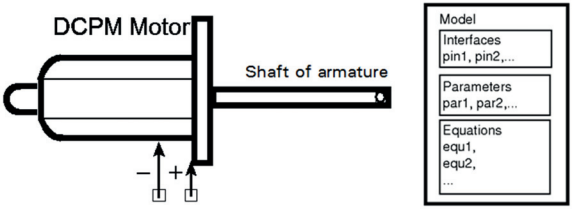

Figure 4.4: Model of DCPM motor

Behind the graphic model of DCPM motor, the same mathematical equations as in Eq. 4.1 are implemented in VHDL–AMS to describe electrical and mechanical behaviors. The concrete content and structure of models in VHDL–AMS are presented in appendix A. Model of DCPM motor is shown as an example.

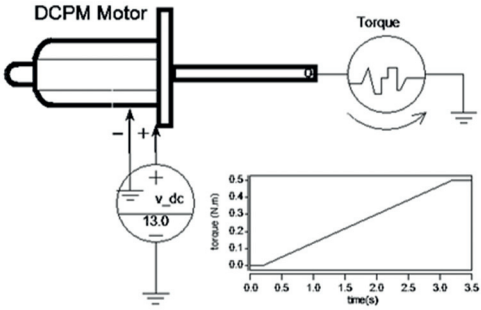

Parameter	Value
ke	0.020378816
kt	0.017258310
La	1.018000000
Ra	0.555841275
J	8.037360000E-06
Visc coef	1.893949567E-05
Mcoul	0.002055545

Figure 4.5: Verification of DCPM motor model

Verification is required, to make sure that requirements are correctly implemented in models. To verify DCPM motor, current and velocity as function of torque are defined as target quantities. Their values are compared between analytical calculation in Mathematica® and numerical simulation. In both calculations, the same voltage, load torque and parameter set are provided, as in Fig. 4.5.

The result of comparison in Tab. 4.2 4.3 shows that velocity curves and current curves from simulation and mathematical calculation overlay each other. Quantitative difference is less than 0.8%.

Table 4.2: Speed comparison between calcuation and simulation

Troque [Nm]	Vel. Sim. [rpm]	Vel. cal. [rpm]	Diff. [%]
0.031	5452	5456	0.08
0.050	5171	5171	0.07
0.101	4433	4436	0.07
0.150	3703	3706	0.07
0.200	2974	2976	0.06
0.251	2236	2238	0.04
0.300	1507	1508	0.02

Table 4.3: Current comparison between calcuation and simulation

Troque [Nm]	Cur. Sim. [A]	Cur. cal. [A]	Diff. [%]
0.031	2.44	2.42	0.8
0.050	3.52	3.50	0.5
0.101	6.35	6.34	0.2
0.150	9.15	9.15	0.1
0.200	11.9	11.9	0.1
0.251	14.8	14.8	0.3
0.300	17.6	17.6	0.0

4.1.1.3 Parameter identification

Parameter identification is to find out suitable values of parameter with suitable methods. In the case of DCPM motor and WR drive, the author summarizes three possibilities.

1. Drive data sheet or component specification
2. Laboratory method and designated experiments
3. Calculation with existing measurements

DCPM motor has wide applications in industry and in daily life. Lots of studies have been conducted on modeling and parameterization. A comparison of methods to identify parameters of DCPM motor are discussed and attached in appendix B.

In this work, a procedure is developed to find parameter values with affordable effort but not at the cost of losing precision. The identifica-

tion is flexible, by using different information resources and combining different methods. Tab. 4.4 shows the identification method.

Table 4.4: Parameter identification of DCPM motor

Parameter	Unit	Identification
R_a	Ohm	Supplier specification or calculation
L_a	uH	Supplier specification
k_e	V/(rad/s)	Calculation from characteristic lines
k_t	Nm/A	Calculation from characteristic lines
M_c	Nm	Calculation from characteristic lines
$Visc$	Nm/(rad/s)	Experiments or calculation
J_a	kg*m2	Supplier specification

Mainly, there are two sources. One direct source is component specification or data sheet from suppliers. The other indirect one is to deduce values from characteristic curves(performance curves) measurements. Normally, component specification or data sheet could provide the electrical and mechanical characteristic values, like rotor inertia and winding resistance and inductance. But, other parameters may be provided with additional cost. The problems are

- the cost to obtain additional parameter is usually higher than the added value.
- Suppliers may also decline the request with the argument that they are their "Know-Hows".
- Automobile industry is cost sensitive. Every piece of additional request in component specification means more cost.

To overcome the problems, the other part of parameters are obtained through the industry standardized measurements. One of the standardized measurements for WR drive is characteristic curves, or called performance curves.

Fig. 4.6 shows a measurement characteristic curves for a WR drive. For DCPM motor, the same measurement exists. In the result of measurements, the x-axis is torque applied at drive, the left y-axis is ro-

tational velocity and the right y-axis is current. The colored lines in the figure are the measurements in both clockwise and anti clockwise rotation, while the dashed lines mark boundary of drive characteristics. The graphic gives an straightforward impression. Besides, there are discrete measurement information at two torque points. At each torque point, values of velocity and current are measured and recorded. As a standard, the two torque points are each taken at 10% and 50% of the maximal torque of drive.

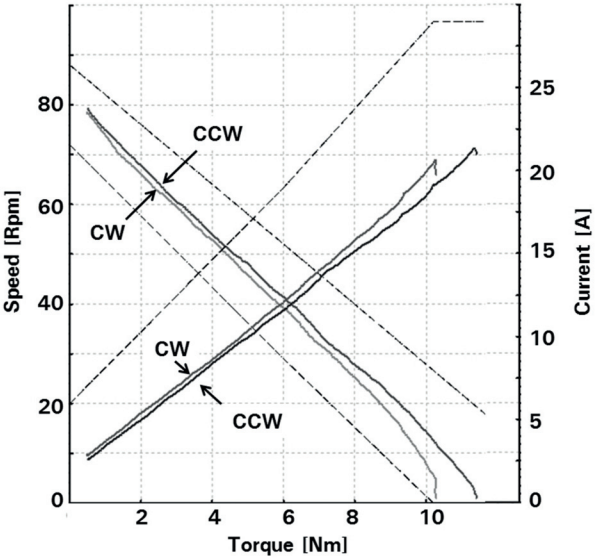

Figure 4.6: Measurement of characteristic curves

The values of velocity and current at two torque points are inputs for parameter calculator. The output are R_a, k_e, k_t and M_c. The parameter calculator is developed in this work. With it, all parameters for DCPM motor can be identified.

4.1.1.4 Validation

The goal of validation is to ensure that right models are found for target objects or processes. There are many ways of validation [84]. One of the

direct ways is to compare model simulation results with measurements of objects in reality. However, criteria should be set before validation actions are carried out. It prevents that comparisons take too much details in account, which then leads to the loss of overview. In the case of DCPM motor model, general criteria are defined as below.

- The parameter set should achieve a high degree of approximation of speed-torque curves of DCPM motor within working range under room temperature.
- The effort should be reasonable to achieve necessary preision in identifying values of parameters and validating simulation models.

The working range of DCPM motor is defined in the thesis to be from 10% to 80% of maximal torque. In such range, the behavior of DCPM motor has a high degree of linearity. Meanwhile, it can already provide a good basis for later comparison with drive performance curves and it covers completely normal working range of drive. In the range of 80% to 100%, measurement equipment can not determine a relatively precise value of moment at armature, rotational velocity and current, because of the disturbance from commutating process at low speed. In the range of 0% to 10%, the effects of brush voltage drop, brush leak current and brush resistance lead to a slight different linearity. Additionally, under normal working condition, the range of 0% to 10% is not used.

Not to over load motor tests, it is developed in the thesis to deduce part of parameters from standardized measurements of DCPM motor performance curves. Parameter set is searched under room temperature. For motor models under -30°C and +80°C, another two set of parameters can be identified with the same method. It needs less effort, in comparison with determining temperature coefficient of each single parameter. At the moment, this method is sufficient to provide reliable parameter set for investigating motor behaviors under different temperature.

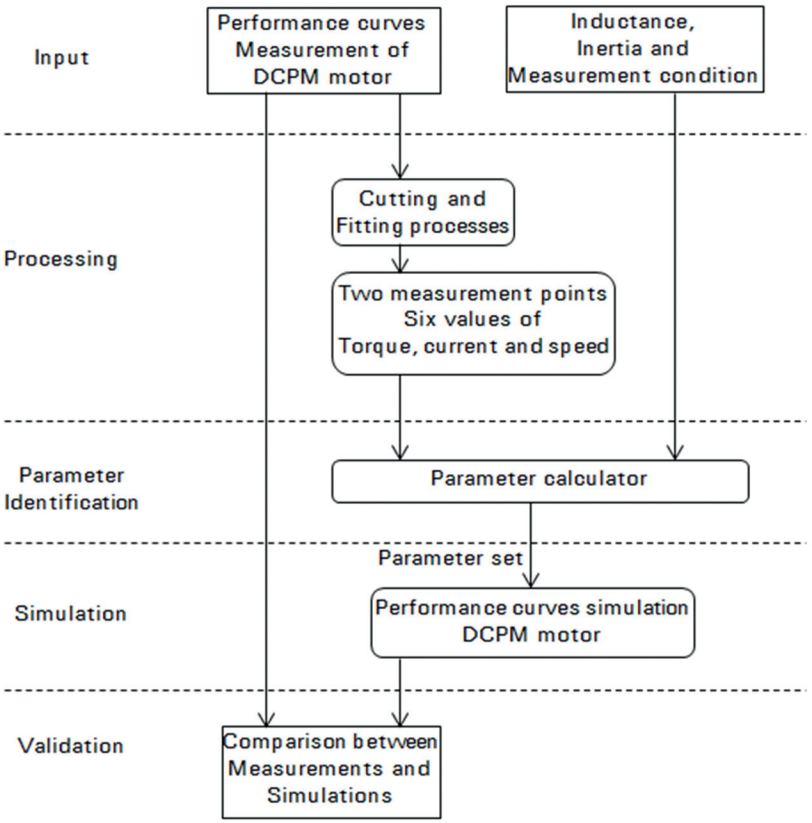

Figure 4.7: Procedure of parameter identification and validation

The validation processes in this section will be divided mainly into two segments. The first one is about deducing parameter values. The second one is simulating performance curves and then comparing simulation result with measurements. The complete procedure of parameter identification and validation is shown in Fig. 4.7.

The measurements of DCPM motor performance curves are performed in the test stand shown in Fig. 4.8. The backplate, which stands on the test platform, holds from one side the motor fixture and from the other side the relative position of servo drive, velocity and torque sensors. The

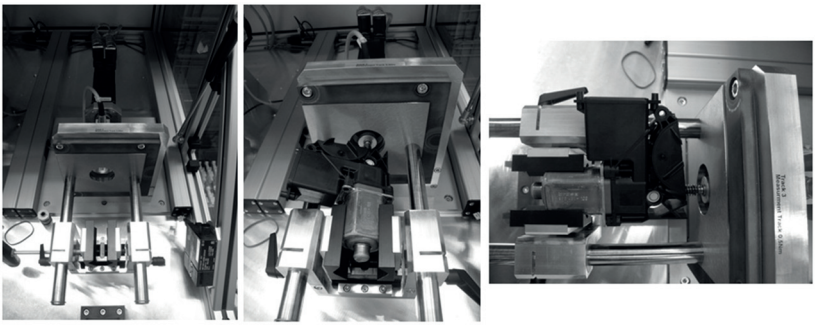

Figure 4.8: Measurement stand of DCPM motor performance curves

motor body is clamped by the fixture and the armature is coupled with servo drive through the hole on the backplate. When one measurement starts,

- Step 1: Motor is driven with 13 V and servo drive pushes motor in this phase to rotate at about 6200 rpm. At this speed, motor is working as a generator. Torque sensor shows a negative value.
- Step 2: The speed of servo drive decreases slowly so that the motor current increases to be positive, until torque sensor reaches zero. At this moment, the no–load speed and no–load current of motor are recorded.
- Step 3: Speed of servo drive is decreased further. Servo drive serves as linear increasing load to motor. Speed of motor decreases gradually and current increases.
- Step 4: Speed reduction continues until motor is stalled. At that time, stall torque and stall current of motor are recorded.

Between the no–load point and stall point, torque, speed and current are observed and recorded.

Measurements of performance curves are used to identify parameters of DCPM motor models. The identification procedure can process single measurement data. It can also be exploited in processing a group of motors.

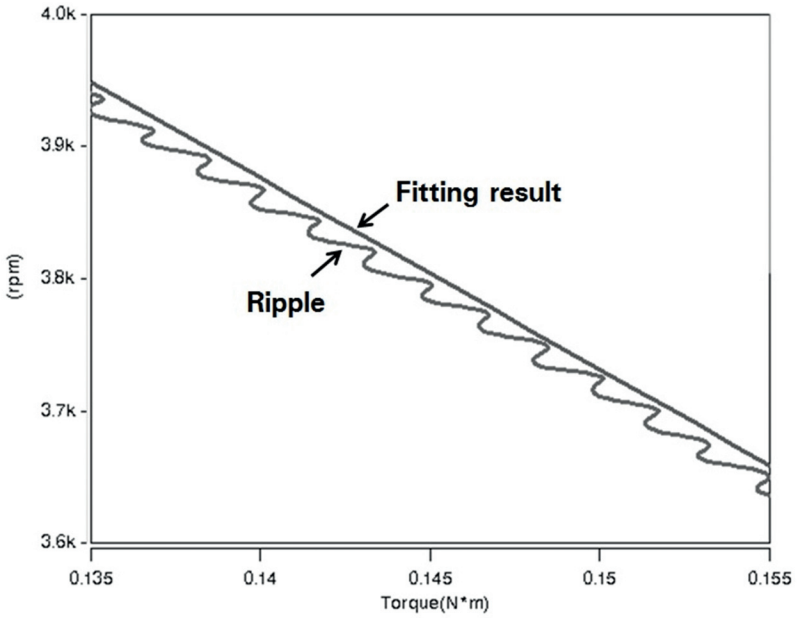

Figure 4.9: Fitting measurements and ripple in curves
x-axis: torque; y-axis 1: rotational speed

a) Identification procedure of single measurement
The procedure firstly filters row data of a measurement to find speed–torque curves and current–torque curves over defined working range. Then the two curves are fit with first order polynomial approximation, to be linear lines. The reason is that measurement has ripples because of commutating process, shown in Fig. 4.9. From the linear lines, velocity and current at two different torque points are selected. Six values in two torque points, together with inductance and inertia, are given to the parameter calculator. The parameters, output from calculator, then will be simulated in DCPM motor model and the result is compared with measurement.

Fig. 4.10 demonstrates the procedure. Fig. 4.10(a) is the row data from measurement. It is the change of motor torque over time, where

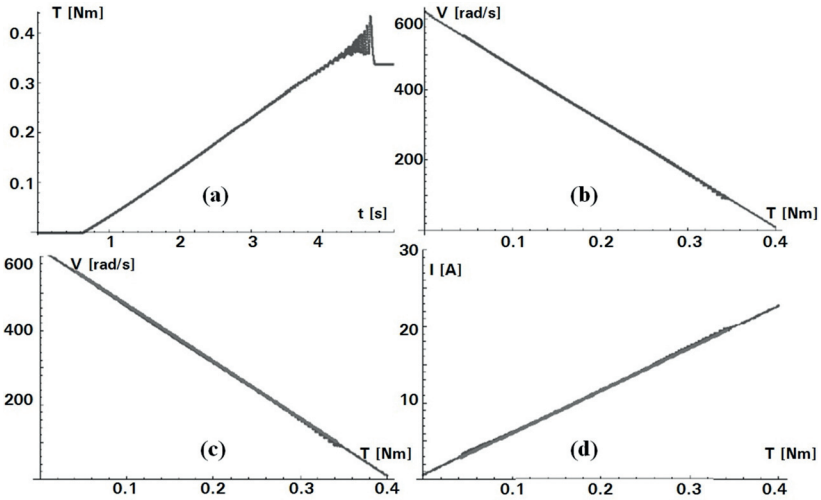

Figure 4.10: Validation of single motor
(a) Measured armature torque over time
(b) Comparison of fitting and measured speed–torque curves
(c) Comparison of simulation and measured speed–torque curves
(d) Comparison of simulation and measured current–torque curves

it is seen that lots of vibration take place almost at the end of measurement. After cutting and fitting process, the output of speed–torque curve is compared to measured curve, shown in Fig. 4.10(b). With the calculated model parameters, the comparison of speed–torque curve and current–torque curve between measurement and simulation are presented in Fig. 4.10(c) and (d). In the working range, the difference is neglectable.

b) Identification procedure of a group of measurements

The comparison above proves the validation of motor model and parameter set for single motor. In practices, two motors with the same design, the same production line and the same batch can hardly have the same performance curves. So, it is meaningful to find a model representing a family of motors.

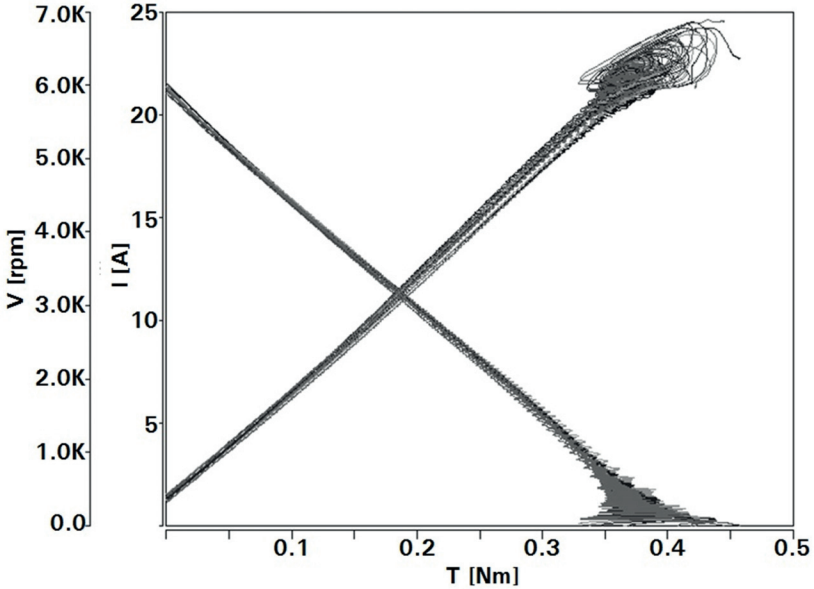

Figure 4.11: Measurements of 5 motors
x-axis: torque; y-axis 1: rotational speed; y-axis 2: current

Five pieces of Bosch 12Nm drives are picked up randomly and sent into motor performance curve measurements. Before measurements, gear and gear housing of drives are detached from DCPM motors. Maximal output torque of this type of DCPM motors can range from 0.35Nm to 0.45Nm. The measurement results of both rotation directions are represented in speed–torque curves and current–torque curves, shown in Fig. 4.11. The Fig. shows that motor stalls at about 0.4Nm and has a idle rotational velocity at about 6000rpm. The idle current and stall current are each about 1.2A and 25A. It is clear to see curves are disordered in the range of high torque. This part is not used in identification procedures. Each measurement is cut to leave the range from 10% to 80% of max torque. Linear fitting lines are found for every motor curves. The fitting result is shown in Fig. 4.12.

Boundaries lines and mean value line are found for the group of fitting curves, shown in Fig. 4.13. Besides, the middle line between boundaries

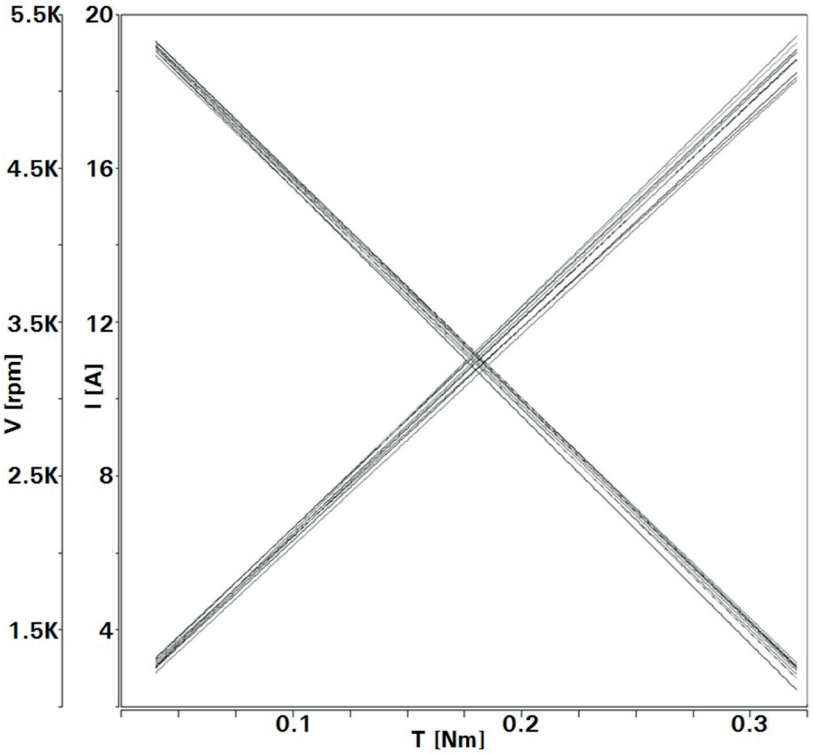

Figure 4.12: Fitting of 5 motors
x-axis: torque; y-axis 1: rotational speed; y-axis 2: current

is produced and it is used as the basis to abstract measurement points for parameter calculation. The boundaries lines are helpful to have an overview how much deviation one motor could have from another. The middle line of boundaries is served to find a nominal parameter set, representing a group of motors. A phenomenon in the comparison of fitting curves and boundary curves is that no motor is overlapping boundaries in the complete range.

Values of speed and current are measured at two different points of torque on the middle line of fitting boundaries. At point $i_{an}, n = 1, 2$, it is defined, M_n as armature torque, i_{an} as motor current, and ω_{an} as

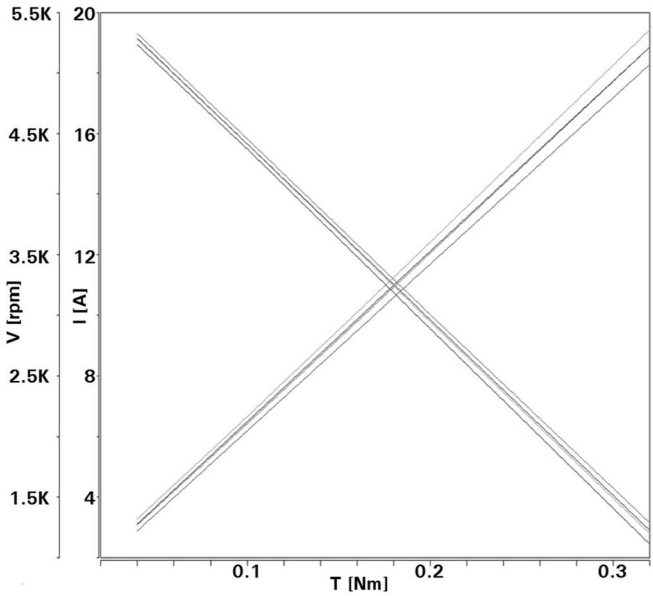

Figure 4.13: Min, max and mean curves of fitting of 5 motors
x-axis: torque; y-axis 1: rotational speed; y-axis 2: current

armature velocity. All the six values are input to automatic calculation tool, together with motor inertia, inductance and testing conditions. Inside the parameter tool, the calculation processes are done in the following steps. $M_n, i_{an}, \omega_{an}, n = 1, 2$ are applied to equations 4.1. Then, obtain,

$$U_a = R_a \cdot i_{a1} + L_a \cdot \frac{d}{dt} i_a + k_e \cdot \omega_{a1} \tag{4.2a}$$

$$k_t \cdot i_{a1} = M_c + Visc \cdot \omega_{a1} + J \cdot \frac{d}{dt} \omega_a + M_1 \tag{4.2b}$$

$$U_a = R_a \cdot i_{a2} + L_a \cdot \frac{d}{dt} i_a + k_e \cdot \omega_{a2} \tag{4.2c}$$

$$k_t \cdot i_{a2} = M_{coul} + Visc \cdot \omega_{a2} + J \cdot \frac{d}{dt} \omega_a + M_2 \tag{4.2d}$$

According to Eq. 4.2a, when $i_a = 0$ and i_a is about to increases, ω_a reaches the high value. It is called idle speed, ω_i, and can be obtained.

$$\omega_i = \frac{\omega_{a1} - \omega_{a2}}{i_{a2} - i_{a1}} \cdot i_{a1} + \omega_{a1} \tag{4.3}$$

With ω_i, k_e is abtained through

$$U_a = L_a \cdot \frac{d}{dt} i_a + k_e \cdot \omega_{idle} \tag{4.4a}$$

$$k_e = \frac{U_a - L_a \cdot \frac{d}{dt} i_a}{\omega_i} \tag{4.4b}$$

$$\frac{d}{dt} i_a = \frac{di_a}{dM} \cdot \frac{dM}{dt} = \frac{i_{a2} - i_{a1}}{M_2 - M_1} \cdot \frac{dM}{dt} \tag{4.4c}$$

$$\frac{dM}{dt} = const. \tag{4.4d}$$

In equations 4.4, the rate of torque increment is known, because the torque of DCPM motor is applied with a servo drive, which is programmed to constantly increase the torque from $0Nm$ to $0.5Nm$ over 3 seconds.

Substract equation 4.2c by equation 4.2a gives

$$0 = (i_{a2} - i_{a1}) \cdot R_a + K_e \cdot (\omega_{a2} - \omega_{a1}) \tag{4.5a}$$

$$R_a = k_e \cdot \frac{\omega_{a1} - \omega_{a2}}{i_{a2} - i_{a1}} \tag{4.5b}$$

Substract equation 4.2d by equation 4.2b gives

$$(i_{a2} - i_{a1}) \cdot k_t = Visc \cdot (\omega_{a2} - \omega_{a1}) + (M_2 - M_1) \tag{4.6a}$$

$$K_t = \frac{(Visc \cdot (\omega_{a2} - \omega_{a1}) + (M_2 - M_1))}{i_{a2} - i_{a1}} \tag{4.6b}$$

Substitute k_t in equation 4.2b with 4.6b, then

$$\frac{(Visc \cdot (\omega_{a2} - \omega_{a1}) + (M_2 - M_1))}{i_{a2} - i_{a1}} \cdot i_{a1} = M_{coul} + Visc \cdot \omega_{a1} + J \cdot \frac{d}{dt}\omega_a + M_1 \tag{4.7a}$$

$$Visc = \frac{i_{a1}\dfrac{M_2 - M_1}{i_{a2} - i_{a1}} - J\dfrac{d}{dt}\omega_a - M_1}{\omega_{a1} + \dfrac{\omega_{a1} - \omega_{a2}}{i_{a2} - i_{a1}} i_{a1}} \tag{4.7b}$$

$$\frac{d}{dt}\omega_a = \frac{d\omega_a}{dM} \cdot \frac{dM}{dt} = \frac{\omega_{a2} - \omega_{a1}}{M_2 - M_1} \cdot \frac{dM}{dt} \tag{4.7c}$$

With $Visc$ known from 4.7b, k_t becomes known from 4.6b. In the end, M_{coul} can be obtained

$$M_{coul} = i_{a1} \cdot K_t - M_1 - J\frac{d}{dt}\omega_a - Visc \cdot \omega_{a1} \tag{4.8a}$$

With the equation and calculation processes above, values of parameters are determined. Until here, parameter identification is done. Parameters are then applied in the simulation models of DCPM motor. Models are simulated and simulation results of performance curves are compared with fitting curves and measurement result.

It is hardly to find difference between simulated curves and middle curves of fitting boundaries from vision in Fig. 4.14. A quantitative comparison between these two sets of curves are presented in Fig. 4.15. The comparison table shows that the rotational speed has a maximal 1.8% difference and the current has a maximal 4.03% difference.

In the end, the simulated performance curves of DCPM motor is compared with physical measurements of 5 motors, shown in Fig. 4.16. The dark and straight lines indicate simulation result of speed–torque curve and current–torque curve, while other are measurements. The two thin vertical lines in Fig. mark the working range from 10% to 80% of maximal torque. Within this working range, the simulated

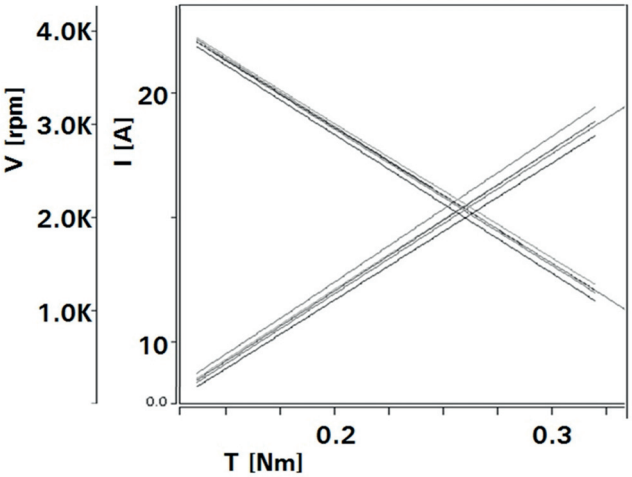

Figure 4.14: Comparison simulation with fitting curves
x-axis: torque; y-axis 1: rotational speed; y-axis 2: current

Torque arm	Sim Vel armature	Speed Mean	Speed difference %	Sim Current	Current Mean	Current difference %
0.042956	5276.9	5238.3	0.731490079	3.1141	3.245	4.033898305
0.10042	4435.6	4408.7	0.606456849	6.3432	6.4443	1.568828267
0.15314	3663.9	3635.9	0.764212997	9.3056	9.4041	1.047415489
0.2	2977.9	2949.4	0.95705027	11.939	12.046	0.888261664
0.25005	2245.1	2219.3	1.149169302	14.752	14.886	0.900174661
0.30064	1504.6	1481.4	1.541938057	17.594	17.757	0.917947852
0.31928	1231.8	1209.5	1.810358824	18.642	18.814	0.91421282

Figure 4.15: Quantitive comparison simulation with fitting curves

speed–torque curves have a good approximation to measurement. The current–torque curve fits to measurements in the most part but has a little gap at 0.04Nm and this gap increase as torque decreases to zero. The reason is that the resistive effect of brush reduces as measurement goes on. When motor stands still for a while, a thin layer on the surface of brush is oxidized. This oxidization layer has a higher resistance, in comparison to the resistance of brush itself. When motor starts to turn, the oxidization layer is worn out and the resistance decreases. In simulation model this changing resistance is not considered. Therefore, the simulated rotational speed is a little higher than the measurements in the low torque range. In the high torque range, simulation results

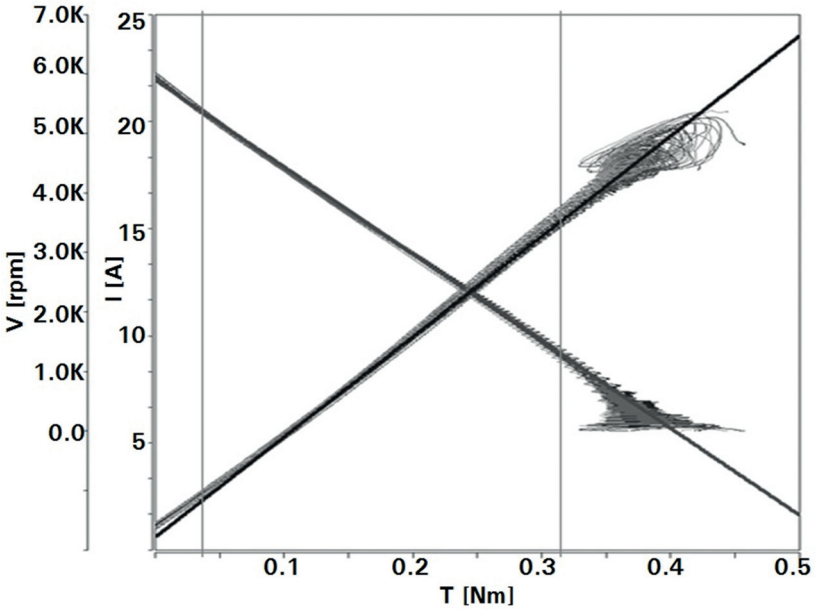

Figure 4.16: Comparison simulation with measurements curves
x-axis: torque; y-axis 1: rotational speed; y-axis 2: current

do not have disturbance like in measurement, because commutating process is not present in model. In the rest, the simulation model is acceptable to represent a family of DCPM motor.

This method can be applied to other motors from different suppliers, to produce reliable parameter sets. It is necessary to point out that the selection of measurement points has influence on parameter set and then later on the comparison of simulation results. It is possible to find lots of different combinations of parameters, the simulation with these parameters can all fit to measurements very well. It is also clear that searching for better parameter sets can be an infinite loop of improvement. The answer to the question, which set of parameters is the best or until when one has to stop searching for better parameter set, depends highly on the required quality of simulations and the research goal. Regarding DCPM motor model, a good coincidence of speed-

torque curve is under request, with the condition that no additional effort involves. The parameter identificaiton procedure, developed in this work, is flexible to fit in use of single motor and also a group of motors.

4.1.2 Worm gear

4.1.2.1 Mathematical description

A worm gear mechanism is a combination of two gears. One gear is called "worm", which is in the form of a screw, while the other is called "gear" or "gear wheel", which is similar like a spur gear. In the rest of the thesis, worm gear will be called gear in short.

The function of worm gear determines its usage in WRs. The worm gear arrangement decreases rotational speed and increases torque, when driving power is transferred from worm to gear. In WR systems, DCPM motors usually have a high output rotational velocity, about 6000 rpm, and a low output torque ranging from 0.35 Nm to 0.45 Nm. With worm gear attached, output speed is reduced to 80 rpm and output torque is increased to be from 9 Nm to 13.75 Nm. Then, it can be used in different designs of WRs and doors. When rotational power is transferred from gear into worm, worm remains its angular position. In applications, such non-reversibility in the movement is named self–locking function. It plays an important role in WR systems to maintain the last position of glass after power is switched off in motor.

Book [85] and papers [86, 87, 88, 89, 90] have been published on the topics of mathematical models, theory and practice of worm gear mechanism with the purpose to improve the designing and manufacturing processes of worms and gears. It involves geometrical, dynamical details and ambient conditions. The model of worm gear mechanism in this section does not go too deep into details but tries to describe its behaviors in an abstract level, because it is not intended to study how the construction parameters of worm gear effect its output performances. The focus is the simulation of the behavior of worm gear.

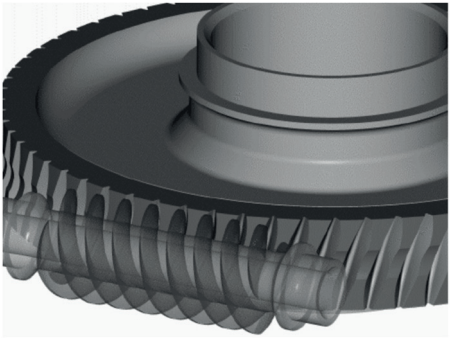

Figure 4.17: Worm gear mechanism

In this section, the functionality of worm gear is represented in simulation system. To this purpose, the behaviors of worm gear are described in two working modes, that is, driving mode and self–locking mode. Under driving mode, driving power is from worm to gear. Under this condition, speed of worm is reduced by a constant ratio, while torque of worm is magnified by the same constant ratio and transmission efficiency. The mathematical equations for driving mode are shown as below.

$$\omega_{worm} = \omega_{gear} \cdot i \tag{4.9a}$$

$$M_{gear} = M_{worm} \cdot i \cdot \eta \tag{4.9b}$$

ω in equations 4.9 are each rotational speed of worm and gear, while M are each torque at worm and gear. The definition of parameters are listed in Tab. 4.5. When a torque is applied at gear to drive worm, worm does not rotate, because of self–locking function. In this period, worm gear is in self–locking model. Theoretically, angle of worm and gear does not change. And no matter how great the torque at gear is, the torque at worm is always zero.

Figure 4.18 demonstrates the basic principle of self-locking function. An object is placed on a rough plane with Coulomb friction coefficient μ. The angle α represents friction angle, which is equal to $\arctan(\mu)$. The angle between the force direction and vertical direction of the plane is

Table 4.5: Parameter definitions of worm gear model

Parameter	Definition	Composition
i	gear ratio	$i = Z_2/Z_1$ Z_1 : number of teeth of worm Z_2 : number of teeth of gear
η	efficiency	$\eta = P_{gear}/P_{worm}$ $= (M_{gear} \cdot \omega_{gear})/(M_{worm} \cdot \omega_{worm})$ $= M_{gear}/(M_{worm} \cdot i)$

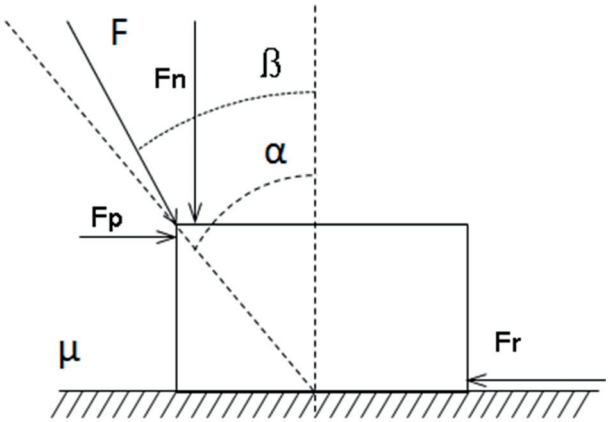

Figure 4.18: Self-locking principle

named β. When β is smaller than α, shown Fig. 4.18, F will not be able to move the object, no matter how much force is applied. The reason is that F_p is not enough to overcome the break–away friction force. The break–away friction force is a product of friction coefficient and the normal force, while F_n is the projection of F on vertical direction. Here the mass of object is neglected.

$$0 < \beta < \alpha < 90^{\circ} \tag{4.10a}$$

$$\tan(\beta) < \tan(\alpha) \tag{4.10b}$$

$$\sin(\beta) < \cos(\beta) \cdot \tan(\alpha) \tag{4.10c}$$

$$F_p = F_n \cdot \sin(\beta) \tag{4.10d}$$

$$F_r = F_n \cdot \mu = F \cdot \cos(\beta) \cdot \tan(\alpha) \tag{4.10e}$$

$$F_p < F_n \tag{4.10f}$$

When the basic principle of self–locking is applied in worm gear, the ground in Fig. 4.18 is the contacting surface of worm and gear. In driving mode, β of driving force is greater than α, then worm can drive gear to rotate. In self–locking mode, the design of worm gear ensures that β is smaller than α, so that friction force neutralizes projected force from gear. However, it is not always that the force angle is smaller than friction angle on contacting surface of worm gear so as to achieve self–locking function. When the force angle is a little bit greater than friction angle, self–locking function can be still ensured by the friction at bearing of worm gear. Therefore, self-locking function is a result of both friction at contacting surface of worm and gear and at the bearing of worm gear.

In practice, too much torque at gear is not allowed, because it could lead to unrecoverable deformation on gear teeth and as a result the movement of worm gear will not be smooth any more.

4.1.2.2 Model and verification

Model of worm gear mechanism has two pins, shown in Fig. 4.19. The pin of worm is to connect to armature shaft of DCPM motor. The pin of gear will act as the output connector of drive. The implementations of worm gear model in this thesis have three architectures[91]. All realize the two working modes defined in the last section. However, methods and internal analysis vary from each other. The first architecture builds

up model based on the description of behaviors, so it is named to be behavioral architecture. The second implementation analyzes the internal interaction of forces at contacting surface and also bearing on a plane, so it has a name as 2D architecture. The last implementation have analysis on internal force interactions in space and so it is given a name 3D architecture. All these architecture of worm gear model are sharing the same pins to connect with other models in simulations. The difference among them lies on how much details are involved in internal analysis and how much information can be used for post processing and evaluation.

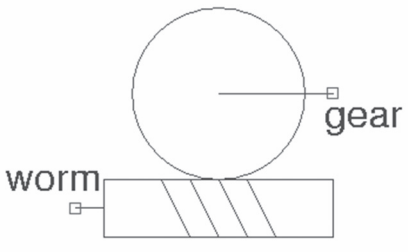

Figure 4.19: Model of worm gear mechanism

4.1.2.3 Behavioral architecture

The internal interpretation of worm gear model in behavioral architecture is represented in Fig. 4.20. Besides the two external pins, there is one internal pin, namely internal_worm. On the left, internal_worm connects a model of gear box. On the bottom, it connects a rotational friction model. On the right, it is linked to output pin "gear". Every pin have a cross variable and through variable, angle φ and torque M.

The gear box model has gear ratio as its only parameter, the value of which is the same to i of worm gear model. The function of gear box model is to transfer movement from one side to the other side without additional loss. The transfer functions are equations 4.11a and 4.11b.

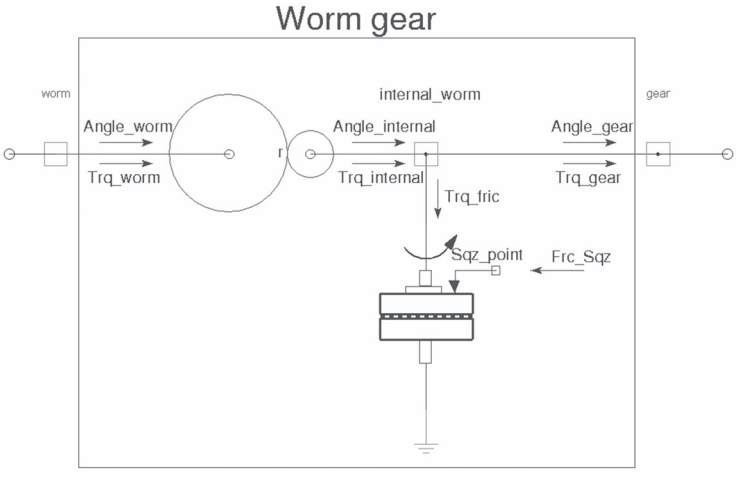

Figure 4.20: Driving mode of behavioral architecture

$$\varphi_w = \varphi_i \cdot i \tag{4.11a}$$
$$M_i = M_w \cdot i \tag{4.11b}$$

$$M_g = M_i - M_f \tag{4.11c}$$
$$\varphi_g = \varphi_i \tag{4.11d}$$

$$M_f = F_{sq} \tag{4.11e}$$
$$F_{sq} = M_i \cdot (1 - \eta) \tag{4.11f}$$

At the internal pin, it deals with torque from three directions. According to nodal circuit analysis principle and Kirchhoff's current law, the sum of torque flowing into one node is equal to the sum of torque flowing out. Under driving mode, torque from gear box model flows into the internal node. There are two branches flowing out. Their relation are given in equation 4.11c. Because there is no additional processing model between internal pin and gear, so it gives equation 4.11d. The ro-

tational friction model serves to produce designated friction loss worm gear. The amount of friction losses is determined by the parameter η of worm gear model in Tab. 4.5. The rotational friction model is designed in the way that the amplitude of friction torque M_f depends linearly on the friction coefficient and the squeezing force, which presses the two reletive rotating disks against each other. By carefully parametrizing the friction model, it can lead to relation quantitatively in equation 4.11e. It is programmed in model that squeezing force F_{sq} is related to internal torque by equation 4.11f under driving mode, so that it produces the same equation as in 4.9, after substituting all φ_i and M_i in equations 4.11 and making first order differentiation over angle. In this manner, the working mode of worm gear model is accomplished.

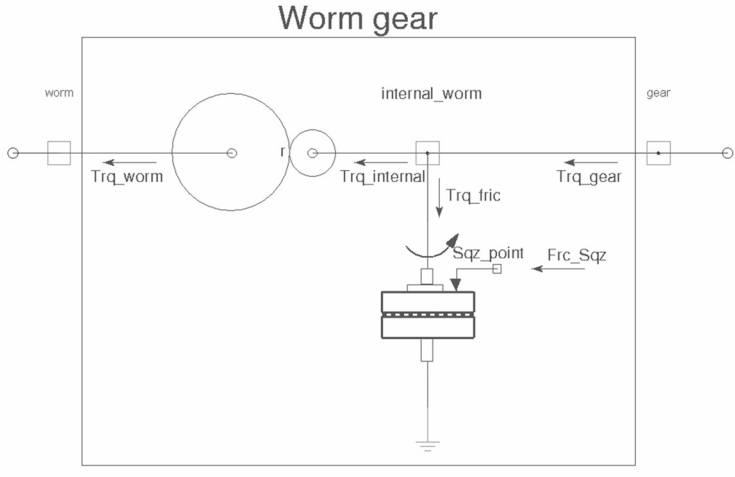

Figure 4.21: Self-locking mode of behavioral architecture

Worm gear model under self-locking mode makes use of the same components as under driving mode, shown in Fig. 4.21. But the tendency of power flow changes to be from gear to worm. As a result, the relation at internal pin switches into equation 4.12c, which means that gear provides all the torque needed for friction and worm. When the torque going into worm is zero, then worm will not be able to turn.

To make it, the same parametrization is applied to friction model and squeezing force is programmed to have the same quantity as torque of gear. Therefore, all the torque at gear flows into friction model but not into worm. Mathematical relations are in equations 4.12. In this way, self-locking function is realized.

$$\varphi_w = \varphi_i \cdot i \tag{4.12a}$$
$$M_i = M_w \cdot i \tag{4.12b}$$

$$M_g = M_i + M_f \tag{4.12c}$$
$$\varphi_g = \varphi_i \tag{4.12d}$$

$$M_f = F_{sq} \tag{4.12e}$$
$$F_{sq} = M_g \tag{4.12f}$$

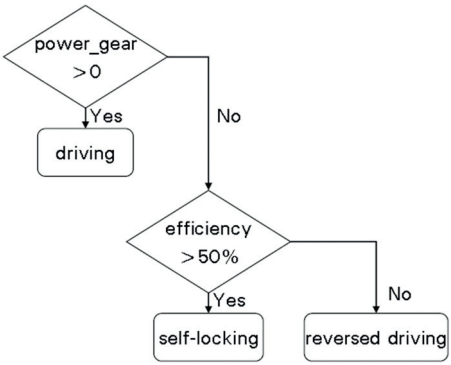

Figure 4.22: Working mode determination

The functions of gear box model and rotational friction model are independent from working mode of worm gear. In contrast, squeezing force depends completely on working modes. The determination of working mode is the important feature of behavioral architecture. Because of the property of nodal network analysis and the interpretation of mod-

eling language in simulator, mechanical power at worm is negative and mechanical power at gear is positive during driving mode, while, during self-locking mode, power at gear turns to be minus and power at worm becomes positive. So, working mode can be determined by observing mechanical power at gear. However, it does not mean that self–locking is always achievable for every worm gears. In practice with worm gear in industry, self–locking function acts when power transmission efficiency, η, is below 50%. When η is higher than 50% and gear tends to drive worm, worm gear goes into reversed driving mode. This working mode can be useful for speed modulation in certain cases. But, in applications of WR systems, it is excluded. The flow chart in Fig. 4.22 shows the determination process of working mode in behavioral architecture.

4.1.2.4 2D architecture

Comparing with behavioral architecture, 2D architecture realizes worm gear model based on simplified kinetic and kinematic analysis. In a narrow sense, worm gear is a gear box with great internal losses to achieve self-locking function. The two kinds of functions are realized in behavioral architecture separately. Transmission is implemented by gear box model, with gear ratio as parameter. The friction model brings internal losses. Self-locking function is through the manipulation of squeezing force under two working modes. This way makes use of the advantages of modeling language, that is, high-level abstraction. However, modeling language can also be used in describing detailed physical interaction. In 2D architecture, the realization of gear box function and self-locking function are integrated together. Because of the kinematic analysis, there are no artificial forces. Every force has its physical meaning. The functions of worm gear model are all performed through the interactions of these internal forces.

The internal interpretation is presented in Fig. 4.23. Mainly, three element components are used. Friction model is the same as used in behavioral architecture. A model, which is called converter, has the function like a windlass to convert translational movement into rota-

tional movement and vice verse. The only parameter of converter is the radius, r. Two instances of it are in 2D architecture. So, One has radius of worm r_w as parameter, while the other has radius of gear r_g. The core component, seen in the center of Fig. 4.23, is called contacting face. It simulates the reletive movements and force interaction between worm and gear. This contacting face represents the contact of movable object and ground in Fig. 4.23. Displacement and force analysis will be taken place in this component.

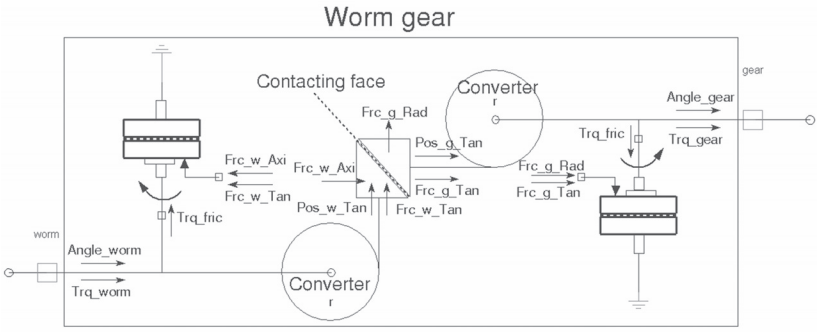

Figure 4.23: 2D architecturea of worm gear model

Friction model, which implements Coulomb friction, represents friction losses at rotational shaft and its bearing. Friction torque changes its sign as rotational velocity changes its direction. To avoid numerical problem, friction torque is linearly proportional to relative rotational velocity when rotational velocity is close to zero. How close speed is to zero is defined by a parameter called velocity threshold, which has usually an magnitude in milli or even micro. The meaning of this parameter is how fast friction torque responds to the change of velocity direction. Break-away friction is neglected in this friction model, because of its insignificance. The amplitude of friction torque depends on radius of shaft, friction coefficient and squeezing force. The squeezing forces for worm shaft and gear shaft have different sources. At the shaft of worm, one force presses against bearing from the tangential direction and another force presses bearing from the axial direction. At the shaft

of gear, these squeezing force are from tangential and radial directions. The magnitudes of these forces are calculated in the model of contacting face.

The model of converter implements function to transform translational and rotational movements. It has one parameter, r, and the governing equations are as below.

$$\varphi \cdot r = S \tag{4.13a}$$

$$M = F \cdot r \tag{4.13b}$$

where φ is angle change, S is displacement, M is torque and F is force.

With the instance of converter model at the both sides of worm and gear, angle and torque at worm φ_w M_w and at gear φ_g M_g are transformed into equivalent position and force in the tangential direction of worm rotational movement, S_w F_w S_g F_g. The conversion has the purpose to make it easy to build up equilibrium with forces in two orthotropic directions. It is also a reason why this is called a 2D architecture.The analysis within model of contacting face is divided into kinetic analysis and force analysis.

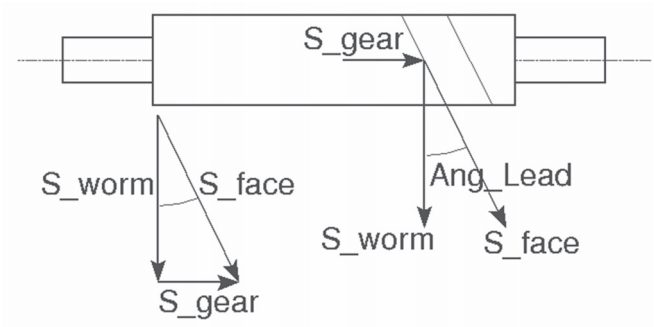

Figure 4.24: Kinetic analysis of 2D architecture at contacting face.
S_worm: S_w peripheral displacement of worm shaft at pitch circle,
S_gear: S_g peripheral displacement of gear shaft at pitch circle,
S_face: S_f relative displacement of worm and gear at contacting face,
Ang_Lead: φ_l lead angle of worm gear at pitch circle

a) Kinetic analysis

Figure 4.24 shows worm and its contacting face to gear. In figure, S_worm is the peripheral translational displacement of worm shaft at pitch circle, while S_gear is the similar displacement of gear shaft. S_face stands for the relative displacement at contacting face. The construction parameter, lead angle φ_l, has the meaning about how much gear rotates at one worm rotation. This angle is between the extension line of contacting face and radial direction of worm axis. With φ_l, the relation among these three displacements can be built as in Fig. 4.24. Mathematically, kinetic analysis in 2D architecture is shown in equation 4.14a.

$$S_g = S_w \cdot \tan(\varphi_l) \tag{4.14a}$$

$$\varphi_g \cdot r_g = \varphi_w \cdot r_w \cdot \tan(\varphi_l) \tag{4.14b}$$

$$\frac{\varphi_w}{\varphi_g} = \frac{r_g}{r_w \cdot \tan(\varphi_l)} \tag{4.14c}$$

$$\frac{\omega_w}{\omega_g} = \frac{r_g}{r_w \cdot \tan(\varphi_l)} \tag{4.14d}$$

$$i = \frac{r_g}{r_w \cdot \tan(\varphi_l)} \tag{4.14e}$$

However, if changing translational movement to rotational movement with pitch radiuses of worm and gear, then equation 4.14a turns to be equation 4.14b. The ratio of angle change is then as equation 4.14c. Rotational speed ratio is as 4.14d. The parameter of gear ratio can therefore be deduced as equation 4.14e. It shows that gear ratio depends on three construction parameters, φ_l and r_w and r_g.

b) Force analysis

There are two cases in force analysis. The first case is without consideration of friction at contacting surface. The second case takes friction into account. As shown in Fig. 4.25, three forces, F_n, F_{wAxiNf} and F_{wTanNf}, build up an equilibrium on the side of worm. The similar equilibrium can be built up on the side of gear too, involving F_n, F_{gRadNf} and F_{gTanNf}. The graphic equilibriums are shown in middle of Fig. 4.25. Mathematical representations of equilibriums are listed in equations.

$$F_{wTanNf} = F_n \cdot \sin(\varphi_l) \tag{4.15a}$$
$$F_{wAxiNf} = F_n \cdot \cos(\varphi_l) \tag{4.15b}$$
$$F_{gRadNf} = F_n \cdot \sin(\varphi_l) \tag{4.15c}$$
$$F_{gTanNf} = F_n \cdot \cos(\varphi_l) \tag{4.15d}$$

From the equations above, it can give the following relations.

$$F_{wTanNf} = F_{gRadNf} \tag{4.16a}$$
$$F_{wAxiNf} = F_{gTanNf} \tag{4.16b}$$
$$F_n = F_{wTanNf} \cdot \sin(\varphi_l) + F_{gTanNf} \cdot \cos(\varphi_l) \tag{4.16c}$$
$$\frac{F_{wTanNf}}{F_{gTanNf}} = \tan(\varphi_l) \tag{4.16d}$$
$$\frac{M_w}{M_g} = \frac{r_{worm} \cdot \tan(\varphi_l)}{r_{gear}} = i \tag{4.16e}$$
$$M_w = M_g \cdot i \tag{4.16f}$$

The analysis above show that normal force builds up a bridge between worm and gear. The ratio of tangential forces of worm and gear is depending only on lead angle, if no friction involves. If transforming to torque, the relation is the same as a gear box without internal losses, seen in Eq. 4.16f and 4.14e.

Under consideration of friction, friction force is firstly calculated as a product of normal force and Coulomb friction coefficient μ_c. Then, it is inserted in force equilibriums.

$$F_f = -F_n \cdot \mu_c \tag{4.17a}$$

The equilibriums with friction forces are graphically shown in the bottom of Fig. 4.25. Forces from worm and gear in different directions are calculated as in equations.

$$F_{wTan} = F_{wTanNf} - F_f \cdot \cos(\varphi_l) \tag{4.18a}$$
$$F_{wAxi} = F_{wAxiNf} + F_f \cdot \sin(\varphi_l) \tag{4.18b}$$
$$F_{gTan} = F_{gTanNf} + F_f \cdot \sin(\varphi_l) \tag{4.18c}$$
$$F_{gRad} = F_{gRadNf} - F_f \cdot \cos(\varphi_l) \tag{4.18d}$$

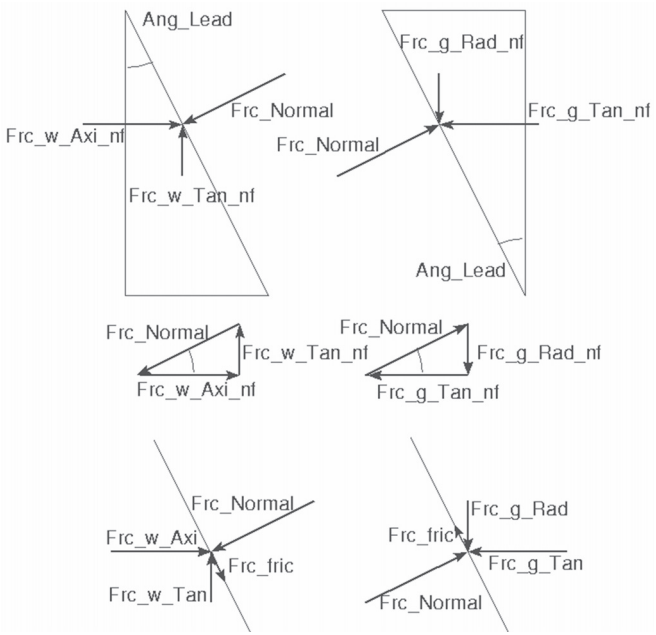

Figure 4.25: Force analysis of worm gear in 2D architecture
Frc_w_Axi_nf: F_{wAxiNf} axial force of worm without friction
Frc_w_Tan_nf: F_{wTanNf} tangential force of worm without friction
Frc_g_Rad_nf: F_{wAxiNf} radial force of gear without friction
Frc_g_Tan_nf: F_{wTanNf} tangential force of gear without friction
Frc_Normal: F_n Normal force of worm gear at contacting face
Frc_fric: F_f friction force of worm gear at contacting face
Ang_Lead: φ_l Lead angle of worm gear at pitch circle.

$$\frac{F_{gTan}}{F_{wTan}} = \frac{(1 - \mu_c \cdot \tan(\varphi_l))}{\tan(\varphi_l) + \mu_c} \tag{4.19a}$$

$$\frac{S_g}{S_w} = \tan(\varphi_l) \tag{4.19b}$$

$$\frac{V_g}{V_w} = \tan(\varphi_l) \tag{4.19c}$$

$$\frac{P_{gNf}}{P_{wNf}} = 1 \tag{4.19d}$$

$$\frac{P_g}{P_w} = \frac{(1 - \mu_c \cdot \tan(\varphi_l)) \cdot \tan(\varphi_l)}{\tan(\varphi_l) + \mu_c} \tag{4.19e}$$

With equations 4.16, 4.17 and 4.18, it gives equation 4.19a, comparing forces from worm and gear when friction is considered. Eq. 4.19a is actually more universal than Eq. 4.16d. When applying friction coefficent, μ_c, to be zero, Eq. 4.19a is reduced to be the same as Eq. 4.16d. It means that Eq. 4.19a covers both conditions with friction and without friction. From Eq. 4.14a, it gets the displacement ratio, seen in Eq. 4.19b. It is then easy to obtain the ratio of velocity, as in Eq. 4.19c. With known ratio of force and velocity, efficiency of power transmission is as in Eq. 4.19d and 4.19e for both conditions with friction and without friction. It is clear to see that, when no friction at contacting face, the power transmission efficiency of worm gear is 100%. With friction considered, power efficiency is a function of μ_c and φ_l. When friction coefficient μ_c transforms into friction angle φ_f, then power efficiency calculation in equation 4.19e changes in form 4.20b.

$$\mu_c = \tan(\varphi_l) \tag{4.20a}$$

$$\eta = \frac{P_g}{P_w}$$

$$\eta = \frac{\tan(\varphi_l)}{\tan(\varphi_l + \varphi_f)} \tag{4.20b}$$

This form of power transmission efficiency of worm gear is in accordance with the form in paper [92] and book [85]. It is necessary to point out that this calculation of power efficiency is limited in the case that worm

is driving gear with constant friction coefficient. It does not take into account other factors, for example, worm gear lubrication, temperature, speed dependent friction and so on. Friction coefficient used in equation is a representation of whole frictional influence.

Comparing to behavioral architecture, 2D architecture requires more parameters. These parameters are grouped into two sets. One set is related to the geometrical information of worm gear. The other set is related to the friction coefficient, at contacting face and at bearing. The transmission ratio and power transmission efficiency in behavioral architecture can be calculated through the combination of parameters in 2D architecture. The calculations are shown in equation 4.14e and 4.20b. Figure 4.26 lists parameters of 2D architecture and the sources for identification. The dimensional information can be obtained from design

Parameters	Identifications
Radius worm	Drawing
Radius gear	Drawing
Radius worm bearing	Drawing
Radius gear bearing	Drawing
Lead angle	Drawing
Friction coefficient of worm gear	Handbook; Empirical
Friction coefficient of bearing	Handbook; Empirical

Figure 4.26: Parameter identification of 2D architecture

and drawing. Here, radius of worm and gear means each pitch radius. It is always difficult to identify an exact value of friction coefficient, because it depends on lots of factors, such as matirial, temperature, lubrication and so on. Common methods are to obtain coefficients from handbook or to determine them empirically. When higher requirement is placed on accuracy, laboratory experiment can be set up to obtain more reliable value of friction coefficient.

Under driving mode, worm drives gear to rotate. Specific rotational velocity reduction is a result from lead angle and radius of worm wheel and gear wheel. Worm gear has great internal losses. A major part of the losses is caused by the friction at contacting faces. For example, when lead angle and friction angle are set to be 6°, power efficiency of worm gear with out considering bearing friction turns out to be about 49.4476%, according to equation 4.20b. Friction coefficient is in value of tan(6°), 0.1051. It is seen in this example that friction coefficient of contacting face has a significant influence on power efficiency under driving mode.

$$F_f = F_n \cdot \mu_c \tag{4.21}$$

Under self–locking mode, gear tends to drive worm. Friction force reverses its direction. Its calculation turns to be equation 4.21. Hence, signs of friction composition in equations 4.18 has to change accordly, + to − and − to +. Then, comparison of tangential forces from gear to worm can be built up, seen in equation 4.22a. Power transmission efficiency from gear to worm is then equation 4.22b.

$$\frac{F_{wTan}}{F_{gTan}} = \frac{\tan(\varphi_l) - \mu_c}{(1 + \mu_c \cdot \tan(\varphi_l))} \tag{4.22a}$$

$$\frac{P_w}{P_g} = \frac{\tan(\varphi_l) - \mu_c}{(1 + \mu_c \cdot \tan(\varphi_l)) \cdot \tan(\varphi_l)} \tag{4.22b}$$

When lead angle φ_l is kept unchanged and friction angle φ_f takes three values, the values of power efficiency changes in the way shown in Tab. 4.6.

The same lead angle and friction angle result that power efficiency is zero. It means that there is no movement tranferred from gear into worm. Therefore, self–locking function achieves. When friction angle is greater than lead angle, power efficiency has negative value, which is not realistic in reality. When friction angle is smaller than lead angle, a positive power efficiency is obtained. It means that power flows from gear into worm. It is expected in this case tangential force of worm is not

zeor. But, self–locking function can still achieve under this situation, because there is still great friction at worm bearing. If tangential force of worm can not overcome bearing friction, worm will not turn and self-locking function is still achievable. From another perspective, lead angle is like the force applying angle in the demonstration of self-locking principle. When lead angle is greater than friction angle, movement should be able to transfer from gear to worm. When lead angle is smaller and equal to friction angle, it is expected that self-locking function is activated.

Table 4.6: Power transmission efficiency under self–locking mode

Lead angle	Friction angle	Power efficiency
6°	5.8°	0.349%
6°	6°	0%
6°	6.2°	−0.349%

In the analysis of driving mode and self-locking mode of 2D architecture, it is seen that friction plays an important role. From one side, it is the reason for the great internal friction losses under driving mode. From the other side, it enables the realization of self–locking function.

4.1.2.5 3D architecture

3D architecture of worm gear model advances the analysis of 2D architecture from being on a plane to being in a space. For worm and gear, three orthotropic directions are considered, shown in Fig. 4.27. Here, Tan, Rad and Axi stand each for tangential, radial and axial direction of shaft. The analysis of angle, torque, displacement and force requires a new parameter in 3D architecture, that is, press angle φ_p.

The 3D architecture has a similar appearance like 2D architecture in Fig. 4.23. The same number of element models are used. Models of converter and rotational friction remain the same. What is different in friction model is that more forces are making up squeezing force. To the bearing on worm side, squeezing force is resultant from axial, radial and tangential force. It is the same with gear side.

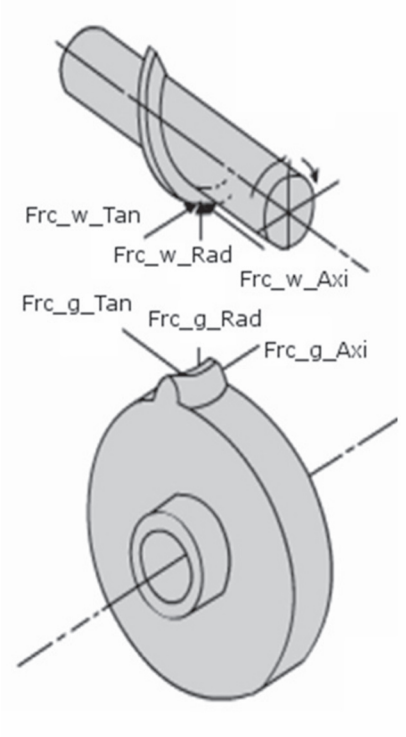

Figure 4.27: Driving mode of 3D architecture
Frc_w_Axi: F_{wAxi} axial force of worm
Frc_w_Rad: F_{wRad} radial force of worm
Frc_w_Tan: F_{wTan} tangential force of worm
Frc_g_Axi: F_{wAxi} axial force of gear
Frc_g_Rad: F_{wAxi} radial force of gear
Frc_g_Tan: F_{wTan} tangential force of gear

In the model of contacting face, the relation of worm and gear displacement remains the same as in 2D architecture. It is supposed that the interaction of worm and gear takes place only on the pitch circle. In this way, φ_p has no influence on the kinetic analysis of worm gear set. The equations are the same in 4.14 for 2D architecture. The most remarkable difference between 2D and 3D architectures lays on force analysis.

In 3D interpretation, normal forces at contacing surface of worm and gear is projected in three orthotropic directions, as shown in Fig. 4.27. With the introduction of φ_p, the relations between normal force and forces in orthotropic directions are as in equation 4.23 from a to f. It is obvious to find out the relations between orthotropic forces of worm and gear as in equation 4.23 from g to i.

$$F_{wTanNf} = F_n \cdot \cos(\varphi_p) \cdot \sin(\varphi_l) \tag{4.23a}$$
$$F_{wAxiNf} = F_n \cdot \cos(\varphi_p) \cdot \cos(\varphi_l) \tag{4.23b}$$
$$F_{wRadNf} = F_n \cdot \sin(\varphi_p) \tag{4.23c}$$

$$F_{gAxiNf} = F_n \cdot \cos(\varphi_p) \cdot \sin(\varphi_l) \tag{4.23d}$$
$$F_{gTanNf} = F_n \cdot \cos(\varphi_p) \cdot \cos(\varphi_l) \tag{4.23e}$$
$$F_{gRadNf} = F_n \cdot \sin(\varphi_p) \tag{4.23f}$$

$$F_{wTanNf} = F_{gAxiNf} \tag{4.23g}$$
$$F_{wAxiNf} = F_{gTanNf} \tag{4.23h}$$
$$F_{wRadNf} = F_{gRadNf} \tag{4.23i}$$

As the next step, friction force at contacting face is calculated in the equation 4.24.

$$F_f = F_n \cdot \cos(\varphi_p) \cdot \mu_c \tag{4.24}$$

Ideally, there is no relative movement of worm and gear on contacting face in radial direction. Therefore, in this direction there is no friction. Friction is on the pitch circle and along the relative movement. The cosinus projection of normal force is on the plane of tangential and axial forces. It is alos vertical to the pitch circle of worm and gear. So, it brings the friction force in contacting face on pitch circle. The friction force is then projected into the orthotropic directions on both worm and gear side. Under the consideration of friction, the final forces in all orthotropic directions are as in equations 4.25.

$$F_{wTan} = F_{wTanNf} - F_f \cdot \cos(\varphi_l) \tag{4.25a}$$
$$F_{wAxi} = F_{wAxiNf} + F_f \cdot \sin(\varphi_l) \tag{4.25b}$$
$$F_{wRad} = F_{wRadNf} \tag{4.25c}$$
$$F_{gTan} = F_{gTanNf} + F_f \cdot \cos(\varphi_p) \cdot \sin(\varphi_l) \tag{4.25d}$$
$$F_{gAxi} = F_{gAxiNf} - F_f \cdot \sin(\varphi_l) \tag{4.25e}$$
$$F_{gRad} = F_{gRadNf} \tag{4.25f}$$

With the analysis above, it gives the ratio of tangential force of gear and worm in equation 4.26a.

$$\frac{F_{gTan}}{F_{wTan}} = \frac{\cos(\varphi_p) - \mu_c \cdot \tan(\varphi_l)}{\cos(\varphi_p) \cdot \tan(\varphi_l) + \mu_c} \tag{4.26a}$$
$$\eta = \frac{P_g}{P_w} = \frac{(\cos(\varphi_p) - \mu_c \cdot \tan(\varphi_l)) \cdot \tan(\varphi_l)}{\cos(\varphi_p) \cdot \tan(\varphi_l) + \mu_c} \tag{4.26b}$$

With the displacement relation unchanged as in 2D architecture, power transmission ratio can be obtained through equation 4.26b. It is in the similar form as in book [93] and patent [94]. In the book and the patent, sinus of press angle φ_p is used instead of cosinus. The reason could be the definition of φ_p. However, it can be concluded that power efficiency in 3D architecture depends on friction coefficient μ_c, lead angle φ_l and press angle φ_p. If φ_p is applied to be zero, power efficiency of 3D architecture is in the same form of 2D architecture in equation 4.20b. When φ_p is designed to be 11.5°, $\cos(\varphi_p)$ has a value of 0.9799, which is very close to 1. Therefore, press anlge has an insignificant influence

on power efficiency.

The working principle of 3D architecture are actually the same as 2D architecture. Friction at bearing and contacting face brings great losses in worm gear set when worm drives gear to rotate, while under self-locking mode internal friction keeps worm still from being turned by gear. Power efficiency calculation under self–locking mode has a form as equation 4.27b.

$$\frac{F_{wTan}}{F_{gTan}} = \frac{\cos(\varphi_p) \cdot \tan(\varphi_l) - \mu_c}{\cos(\varphi_p) + \mu_c \cdot \tan(\varphi_l)} \tag{4.27a}$$

$$\eta = \frac{P_{gear}}{P_{worm}} = \frac{\cos(\varphi_p) \cdot \tan(\varphi_l) - \mu_c}{(\cos(\varphi_p) + \mu_c \cdot \tan(\varphi_l)) \cdot \tan(\varphi_l)} \tag{4.27b}$$

3D architecture needs one more parameter, press angle φ_p, than 2D architecture, which can be obtained from drawing. 2D and 3D architectures are similar but 3D architecture has the possibility to bring more details of force interaction in worm gear.

4.1.2.6 Verification

The verification of worm gear model is to test its functionality, especially under the two working modes. When worm gear is working in driving mode, it is expected to have designated internal loss and speed reduction. When the power efficiency of worm gear is set to be below 50% and gear tries to rotate worm, self-locking function should be activated. The simplest way to test self-locking function is to see whether worm has angular change when motor power is switched off. For verification, test bench is set up as in Fig. 4.28.

In the bench, worm is connected to DCPM motor and gear is loaded with rotational spring. The DCPM motor is powered by a piecewise linear voltage source. The voltage sequence is programmed in the way that motor is driven to rotate in positive direction for four second, then rest for one second, rotate then in negative direction for another four second and in the end stop. The characteristics of DCPM motor are 0.35 N stall torque, 5800 rpm no-load velocity and 23 A stall current.

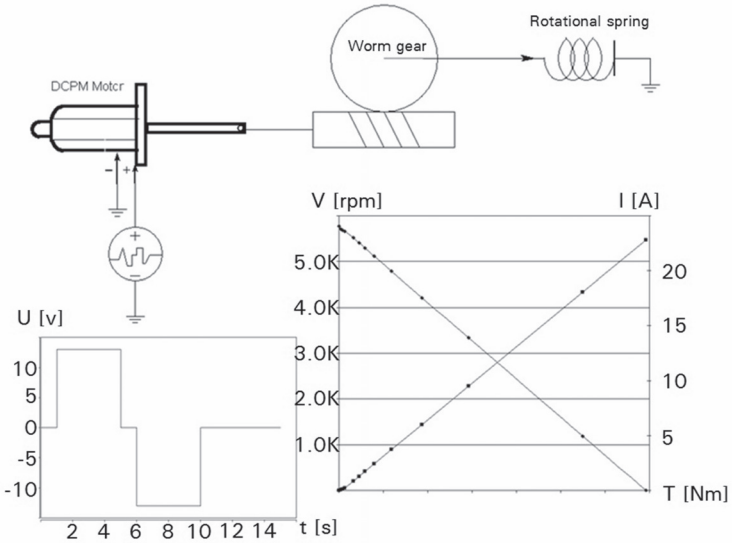

Figure 4.28: Test bench of worm gear

Worm gear model is parametrized in test bench to have a 1 : 73 reduction ratio. In the first simulation, the power efficiency is set 46%, meaning that self–locking function should perform. In the second simulation, the increased efficiency, more than 50%, should deactivate self-locking function. The simulation result is in Fig. 4.29. The upper curves are armature angle of DCPM motor over time. The bottom curvers are armature velocity of DCPM motor over time. When motor is powered to turn in positive direction, armature angle increases. One motor connected to worm gear with higher power efficiency has a higher value of angle change So, within the same period of working time, rotational velocity of one motor is higher than the other. The explanation is as following. Under the same load to gear wheel and the same rotational velocity, output power of worm gear is the same. With higher power efficiency, less power is required at worm wheel. When speed is the same to the two motors. Then the torque needed from motor is less. According to the motor characteristics, less torque means higher velocity, seen in figure 4.29. It is also true to obtain more angle change in

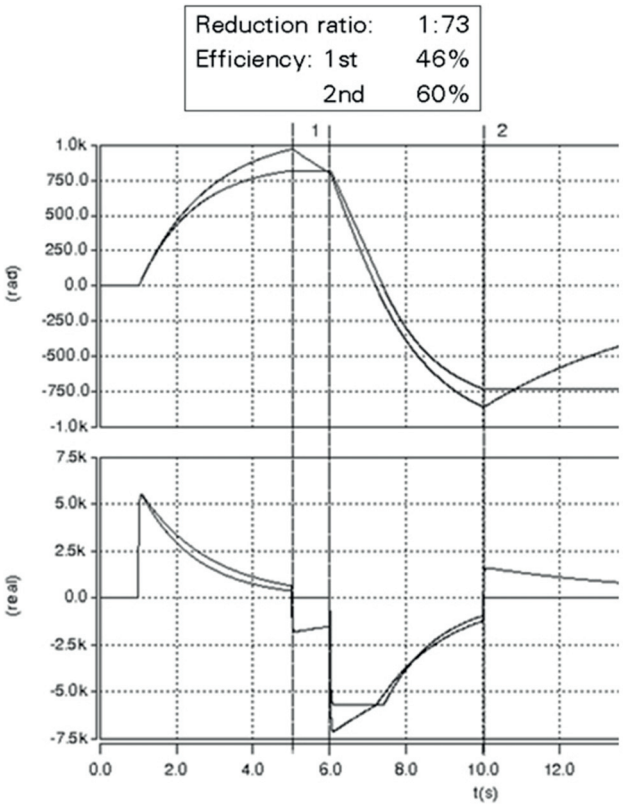

Figure 4.29: Parameter and self–locking function

the same period. At the time point of $5s$, driving power to motor is switched off and the stress in rotational spring begins to rotate gear. The worm gear with less efficiency holds its last position, while the one with higher efficiency rotates in negative direction. From the figure, one curve shows that angle decreases and velocity is not zero from $5s$ to $6s$. Afterwards, the motor is driven with negative voltage for another four second and then stops, self-locking function is present in one worm gear but not in the other one. This type of simulations proves that self-locking function is achievable in worm gear model by setting power efficiency less than 50%.

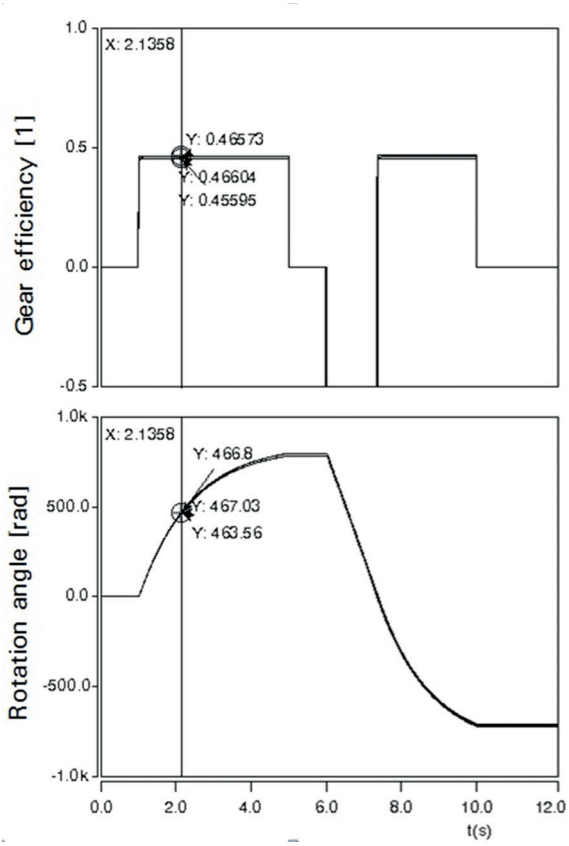

Figure 4.30: Comparison among three architectures

The verification is performed with all three architectures of worm gear model stated in previous section. Behavioral architecture can be directly parametrized by the two values in test bench. Reduction ratio is achieved in 2D and 3D architectures by proper values of lead angle, radius of worm and gear. Adapting friction coefficients of bearing and contacting face can reach the purpose to change power efficiency in 2D and 3D architectures. Through practices , it is found that power efficiency has a higher sensitivity to friction coefficient at contacting face.

The curves in Fig. 4.30 compare the simulated power efficiency and armature angle of three architectures. The power efficiency is parametrized in all three architectures to be 46.3%. The simulated power efficiency is calculated in model by comparing output power and input power of worm gear. In the comparison, the difference between simulated and designated power efficiency is less than 1%. The simulated result from behavioral and 2D architecture are more close to each other. 3D architecture is less close to them. The reason is that more bearing frictions are involved in 3D architecture.

4.1.2.7 Parameter identification and Validation

Three different realizations of worm gear model are presented and verified. Three architectures have different numbers of parameters. The identification methods are also different from each other.

For 2D architecture, all the parameters present in the parameter set of 3D architecture. So, parameterization of the two architecture can be treated in one process. Basically, parameters are from three sources.

- Drawings
- Handbooks
- Experiments

Most of parameters for the two architectures are regarding the geometrical information of worm gear and they can be obtained directly from drawings. The rest parameters are friction coefficients at bearing and at contacting face. One possibility to get friction coefficients is mechanical handbooks. But, it may not be suitable, because friction coefficient depends on lots of factors and the value from handbook fits to limited conditions.

More precisely, experiment can be set up to measure output torque at gear under certain driving torque at worm. The post analysis of measurements can bring a more trustable value. But, the problem of this experiment is that it costs efforts to set up.

The two parameters of behavioral architecture are ratio and power efficiency. The current worm gear used in WR systems has a gear ratio ranging from 73 to 86. Ratio of worm gear can be obtained through drawing. It is also possible to find out the ratio by counting the teeth on worm wheel and gear wheel. The key parameter of behavioral architecture is power efficiency. In industry practices, it is usually in the range from 40% to 50%. As mentioned before, self-locking function exists when efficiency is below 50%. But, to fulfill such function under different temperatures, from -30°C to 80°C, it is suggested that the efficiency should be not so close to 50%. In the other aspect, the efficiency should not be too low, because it could lead that closing time of glass is longer than customer requirements and implementation of a stronger motor is needed, which means additional weight in vehicle doors.

In this work, a method is developed to identify power transimission efficiency, making use of the standardized measurements of motor and drive characteristic curves. With known gear ratio, power efficiency can be obtained by comparing the two sets of characteristic curves. The concrete processes will be presented in the section of drive parameter identification. There, the quality of parameters obtained from this identification procedure is also proofed.

In the following sections of the thesis, behavioral architecture is used as the main implementation of worm gear model. The advantages of this architecture are that it has less parameters and these parameters can be identified with the current existing standardized measurement methods.

The validation of worm gear models requires the comparison of simulations of worm gear to measurements. One straightforward method is to make measurements of torque and rotational velocity of worm wheel and gear wheel. But such direct measurements are not available and the preparation of measurement costs much effort, One indirect method of validation is to compare the simulated and the measured drive characteristic curves. Model of DCPM motor is verified and validated by

comparing its characteristic curves in previous section. If drive model is also verified an validated with characteristic curves, then worm gear model is certainly validated. Therefore, the validation of worm gear model is bound to the validation of drive model. The detailed procedures and results will presented in the section of drive validation.

4.1.3 Rubber damper

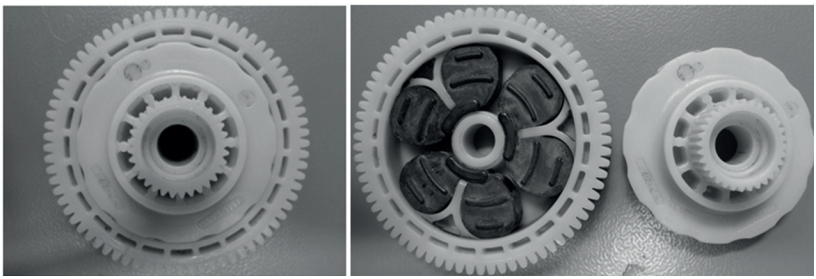

Figure 4.31: Gear and rubber damper

Currently there are two types of gear wheel used in WR drive. One type is one-piece gear and the other can be separated. The gear in Fig. 4.31 is the later one. When gear wheel is opened up, there are three sets of interconnected rubber dampers inside. The function of rubber damper is to reduce dynamical spikes and stationary tension on gear wheel. When glass hits upper frame of door and motor is stalled at the maximal torque, teeth damage on gear wheel could happen With implementation of rubber damper, such situation can be prevented. Compared with system using one–piece gear, stiffness of system using gear with rubber damper is a little lower.

The function of rubber damper in gear wheel is like a rotational spring. This spring connects between worm gear drive and shaft to WR mechanics. Because of its material property, shape and positioning, the effective stiffness of rubber damper is not linear. As to the non-linearity, stiffness of rubber damper is parametrized in model by a look-up table. The look-up quantity is angular deformation and the table gives stiffness as output.

The model of rubber damper realizes the similar equation as model of a normal spring. Difference is only that stiffness of rubber damper depends on deformation.

$$M_{rd} = c(\Delta\varphi_d) \cdot \Delta\varphi_d \tag{4.28}$$

Where M_{rd}: Deformation torque in rubber damper
$c(\Delta\varphi_d)$: Stiffness table of rubber damper, depending on deformation
$\Delta\varphi_d$: Angular deformation of rubber damper.

Table 4.7: Parameter definitions of rubber damper model

Parameter	Definition	Composition
$c(\Delta\varphi_d)$	stiffness of rubber damper	look–up table based on measurement data

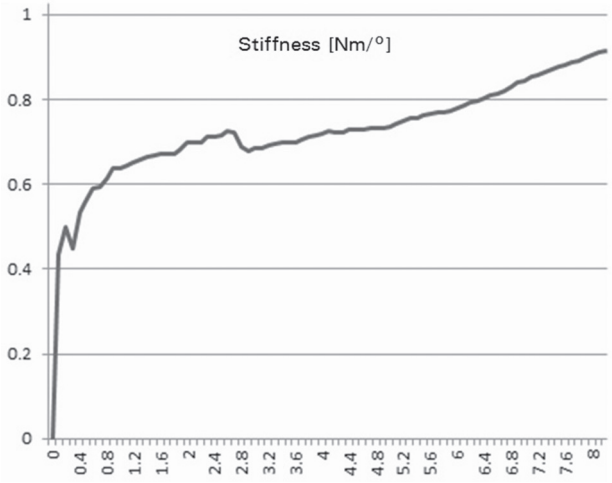

Figure 4.32: Measurement data
x-axis: Angle change in °
y-axis: Stiffness of rubber damper in Nm/°

In stiffness test, gear wheel is fixed in the way that the teeth connecting to worm do not move. A torque wrench is coupled to the gear shaft. Torque and angle change are recorded, while torque wrench is rotated.

Figure 4.32 is the measurement result of one gear wheel. To make use of the measurement, unit is changed from degree into radian and discrete angle change and stiffness are abstracted to form a table. In model of rubber damper, the table rebuilds the relation between angle change and stiffness in piecewise linear method. In this process, an appropriate discrete interval is chosen to make sure that look–up table is not too large and meanwhile sufficient information is stored so as to reproduce stiffness without great losses of accuracy.

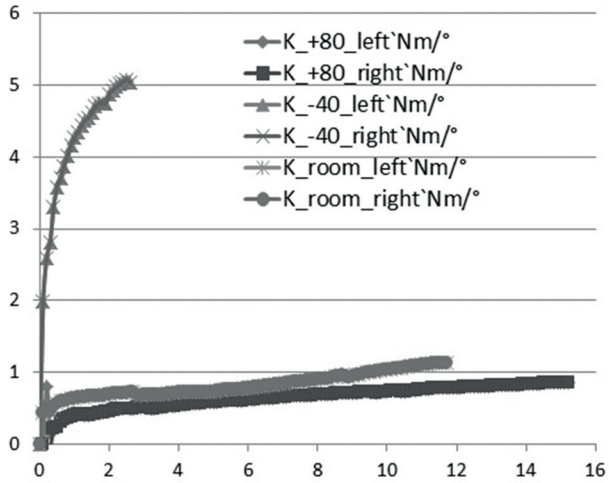

Figure 4.33: Comparison of rubber damper stiffness over temperatures
x-axis: Angle change in °
y-axis: Stiffness of rubber damper in Nm/°

The same measurements of rubber damper stiffness are conducted in left and right rotations and also under three temperature. In Fig. 4.33, it is seen that, under the same temperature, the stiffness does not differ from left and right rotation. However, temperature has a great influence. Under -40°C, rubber damper is quite stiff than under room

temperature. Under 80°C, rubber damper is softer than usually, but the difference to room temperature is not much. With these measurement data, stiffness tables can be built for rubber damper under different ambient temperatures. The parameter identification process has ensured the validation of rubber damper model. So, the validation is not presented.

4.1.4 Drive

4.1.4.1 Mathematical description, model and verification

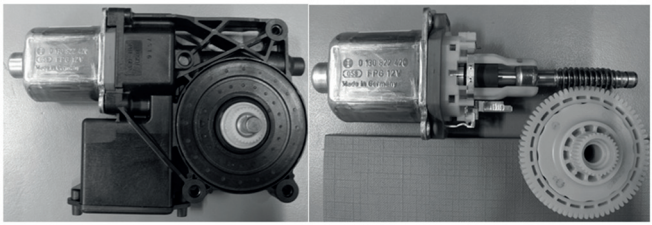

Figure 4.34: Motor and gear coupling

In the physical systems, WR drive is an assembly of DCPM motor and gear. On the left side of Fig. 4.34 is a WR drive, produced by Bosch. The right side shows how DCPM motor couples with gear, with worm gear housing removed.

The same to physical systems, modeling WR drives assembles models of DCPM motor, worm gear and rubber damper. The mathematical representations of DCPM motor are equations 4.1a and 4.1b. Under working mode of worm gear model, movement is transferred according to following equations.

$$\omega_w = \omega_g \cdot i \tag{4.29a}$$

$$M_w \cdot i \cdot \eta = M_g \tag{4.29b}$$

With the effect of worm gear added in these two equations of DCPM motor model, the mathematical representations of WR drive are then

$$U_a = R_a \cdot i_a + L_a \cdot \frac{d}{dt} i_a + k_e \cdot \omega_g \cdot i \tag{4.30a}$$

$$k_t \cdot i_a = M_c + Visc \cdot i \cdot \omega_g + J \cdot i \cdot \frac{d}{dt}\omega_g + \frac{M_g}{i \cdot \eta} \tag{4.30b}$$

The model of rubber damper has negligible influence on stationary rotational velocity and torque of gear wheel. Within the normal working range of drive, 1 Nm to 5 Nm, the deformation of rubber damper is in range between 1 degree and 6 degree under room temperature, shown in the measurement data in Fig. 4.32. During one stroke of WR, gear wheel turns almost 4 rounds, which is 1440 degree. The deformation of rubber damper here is almost incomparable. From another aspect, the load from WR firstly presses on rubber damper and then rubber damper presses on gear wheel. Actually, the torque going through rubber damper has the same value as the load to drive. There is then no torque losses made by rubber damper. In this sense, the mathematical description of WR drive does not consider the effect of rubber damper.

The quantity, M_c, in equations 4.30b indicates the Coulomb friction inside of DCPM motor. M_g is the load on gear wheel. If this load is zero, it is seen in equation 4.30b that there is no loss from worm gear housing. But, in reality, no-load current of drive is usually a little higher than the no-load current of DCPM motor. Such fact means that gear and gear housing bring additional friction in drive under no-load condition. It is explicable because worm gear housing leads to friction at bearings and traction force of grease between worm wheel and gear wheel can also contribute to friction effect. To represent this part of friction, a quantity is introduced, M_{gc}, as a constant friction loss in drive model. Then equation 4.30b is improved to be

$$k_t \cdot i_a = M_c + Visc \cdot i \cdot \omega_g + J \cdot i \cdot \frac{d}{dt}\omega_g + \frac{M_g}{i \cdot \eta} + M_{gc} \tag{4.31a}$$

Mathematical descriptions above provide basis to verify the model of drive. The equations are inputted into Mathematica® to find the analytical solution of rotational velocity and current over time. Simulation of drive gives numarical solution of velocity and current. The two calculation are provided with the same parameter set and the same working condition. The comparison between two calculations are presented in Fig. 4.35. It compares drive current and rotational velocity of gear wheel over torque. Quantitatively, velocity has a difference less than 0.07% and current has difference less than 0.7%.

Torque	Sim_Vel	Math_Vel	Difference_Vel %	Sim_Current	Math_Current	Difference_Current %
1.0057	75.041	75.091	0.066585876	2.3081	2.2942	0.60222694
2.0073	68.701	68.747	0.066912011	4.0628	4.0501	0.312592301
3.5031	59.233	59.273	0.067484352	6.683	6.672	0.164596738
5.0163	49.656	49.689	0.066413089	9.3337	9.3244	0.099638943
7.0058	37.064	37.088	0.064710958	12.819	12.812	0.054606444
9.0282	24.263	24.279	0.065900573	16.362	16.357	0.030558611
11.002	11.771	11.779	0.06791748	19.819	19.817	0.010091327

Figure 4.35: Verification of drive model

4.1.4.2 Parameter identification and validation

Parameter set of drive model is a collection of parameter sets of three component models. The methods of parameter identification of DCPM motor model and rubber damper model have been explained in their sections above. The parameter identification of worm gear model and drive model is achieved by comparing characteristic curves of DCPM motor and drive. The detailed processes of parameter identification is shown in Fig. 4.36.

Characteristic curves of WR drive are measured in the test stand shown in Fig. 4.37. Electrical wires supply power and also control signals to drive. Gear of drive is coupled to test stand as in picture on the right side. When measurement starts, drive is firstly powered with rated voltage, $13V$, so that drive starts to rotate into the max speed in one direction. Afterwards, torque is applied and it increases as linearly as possible. As torque increases, rotational velocity of drive decreases until drive is stalled at the max torque. During the process, voltage,

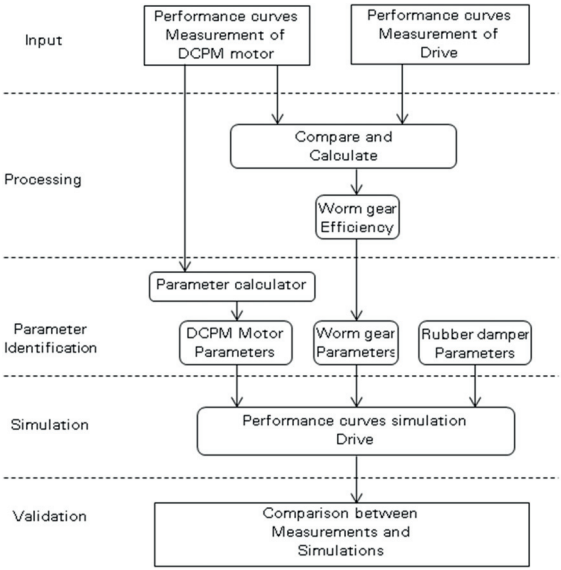

Figure 4.36: Validation procedure of drive model

current, rotational velocity and torque are recorded by test stand. One time of measurement takes about 2 seconds. The same measurement will be repeated when drive rotates in the other direction. At the end, measurement result will be presented.

There are altogether ten measurements of characteristic curves from five drives, shown in Fig. 4.38. These drives in measurements are type of Bosch FPG2 12 Nm and each has been tested in clock-wise and anti-clock-wise rotation. Unlike DCPM motors, characteristic curves of drives have more deviation between each other. There are irregular gaps between clock-wise and anti-clock-wise measurement, as well as between one drive and another drive. It is also clear to see that the vibrations in curves is non-periodic and curves have poor linearity. It can be resulted from two aspects, that is, drive and test stand. Center-to-center distance of worm wheel and gear wheel may not be able to be kept constant. Pitch circle on gear wheel may shift when load increases. On the other side, test stand have tolerance in measurements.

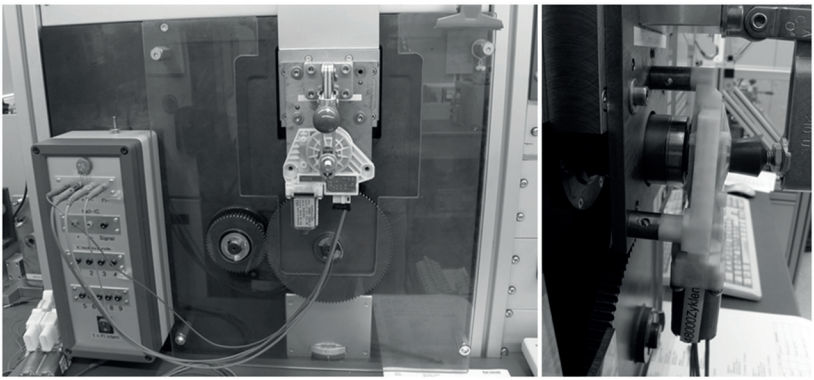

Figure 4.37: Test stand of drive characteristic curves

The measurements of characteristic curves of WR drive are processed in three steps. In short, they are cutting, fitting and calculating.

Step 1: cutting
The first step is to cut measurements to obtain data only in working range. Normally, drive needs 2 Nm to 4 Nm to lift up window glass. When obstacle is encountered, approximate 1 Nm is built up additionally as load. Considering tolerances of systems, working range of drive is extended to be from 1 Nm to 6 Nm.

Step 2: fitting
The second step is to linearly fit the cut data. Figure 4.39 shows one example of the cut data, its fitting curve and the comparison. The gap between fitting curve and measurement is inevitable. Detailed investigation will be not conducted, because the focus is the macro behavior of drives. So, fitting curves will be used to represent the macro behavior of drives. The fitting curve provides a basis to compare with the almost linear characteristic curves of DCPM motors. To be representative for a group of drives, the processes of cutting and fitting are applied to all measurements. From the cluster of fitting results, the boundaries and mean values are found, shown in Fig. 4.40. The mean value curve is used then in the next step to compare with characteristic curves of DCPM motor, which identify efficiency of worm gear.

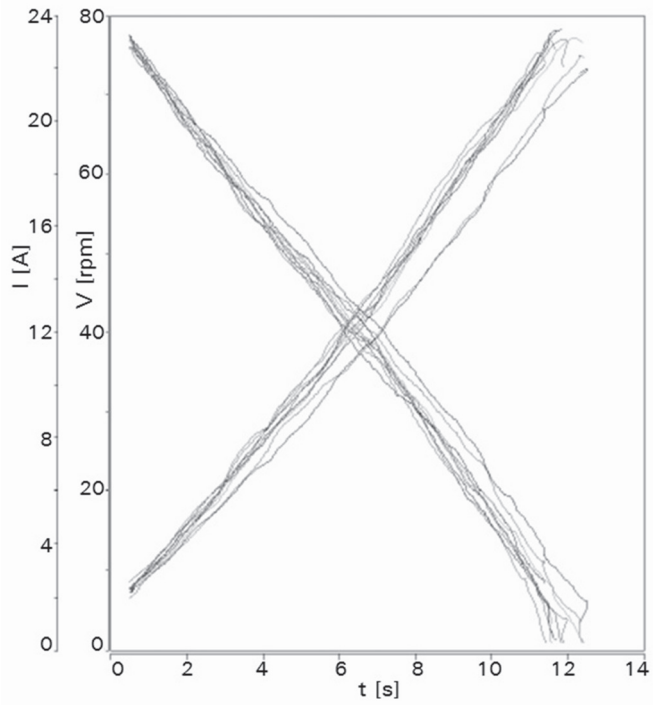

Figure 4.38: Measurements of five drives
x-axis: torque in Nm; y-axis 1: rotational velocity in rpm; y-axis 2: current in A

Step 3: Calculating

The third step is to calculate power transmission efficiency out of the processing result of meansurements. Any coordinates on the line of DCPM motor velocity can be expressed in a function with parameters of ω_{a0}, M_{aMax}, and slope, s_a. So it is the same with drive velocity curve. Here, a indicates armature and d indicates drive. The expressions are shown in Eq. 4.32.

$$\omega_a = s_a \cdot M_a + \omega_{a0} \tag{4.32a}$$

$$\omega_d = s_d \cdot M_d + \omega_{d0} \tag{4.32b}$$

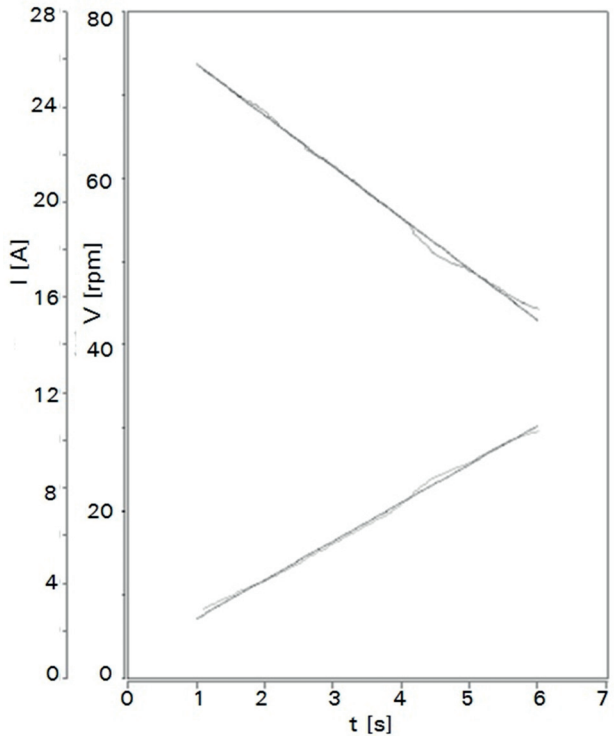

Figure 4.39: Cutting and fitting of measurement in working range
x-axis: torque in Nm; y-axis 1: rotational velocity in rpm; y-axis 2: current in A

With known reduction ratio of worm gear, it gives Eq. ?? and ??. Output torque at gear can be expressed by torqur at armature in the way of equation ??.

$$\omega_a = \omega_d \cdot i \tag{4.33a}$$

$$\omega_{a0} = \omega_{d0} \cdot i \tag{4.33b}$$

$$M_a \cdot i \cdot \eta = M_d \tag{4.33c}$$

Then, substitute Eq. 4.32b with Eqs. 4.35. We obtain,

$$\frac{\omega_a}{i} = s_d \cdot \frac{M_a}{i \cdot \eta} + \frac{\omega_{i0}}{i} \tag{4.34}$$

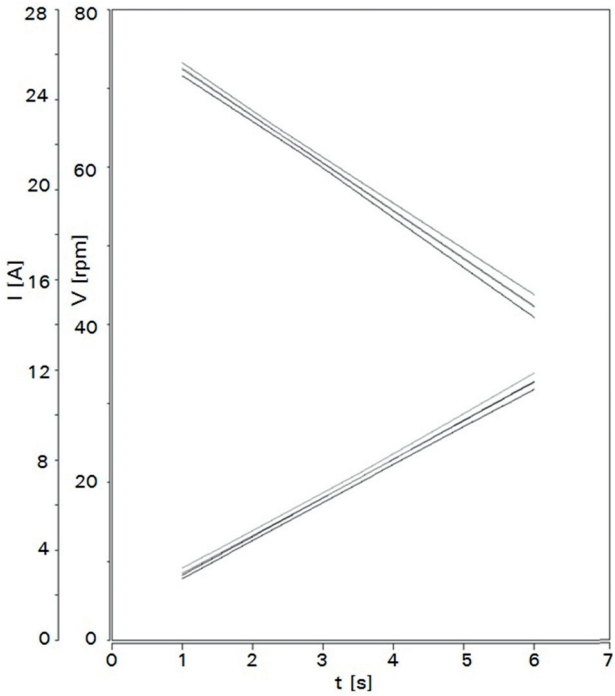

Figure 4.40: Fittings and boundaries of meansurement
x-axis: torque in Nm; y-axis 1: rotational velocity in rpm; y-axis 2: current in A

And divide Eq. 4.34 with Eq 4.32a, it gives 4.35a.

$$S_a = S_d \cdot i^2 \cdot \eta \tag{4.35a}$$

$$\eta = \frac{S_a}{S_d \cdot i^2} \tag{4.35b}$$

With it,efficiency of worm gear is expressed to be a function of gear ratio, slopes of velocity curves of DCPM motor and drive. With known gear ratio and slopes, power efficiency can be calcualted.

In the case of Bosch FPG2 $12Nm$ drives, worm gear ratio is known to be 73. Slope of armature speed over armature torque is -14639.24 and slope of drive speed over drive torque is -6.00. The two slopes can be

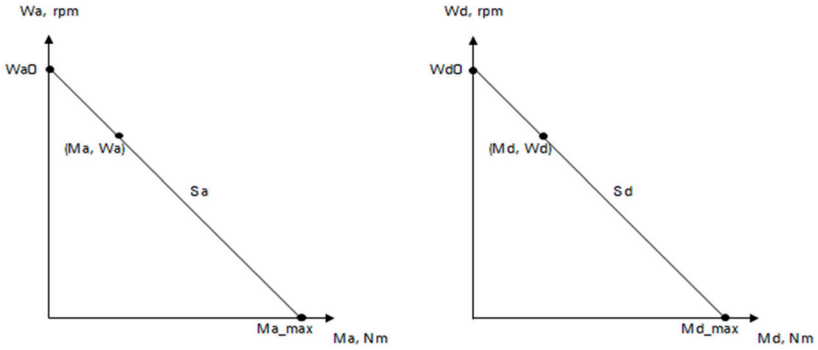

Figure 4.41: Identification of power efficnecy
Left: Rotational velocity over torque of DCPM motor
Right: Rotational velocity over toruqe of drive

abstracted from their fitting curves. Applying these values to equation 4.35b, power efficiency is calculated to be 0.45162397. Until this step, one of the most important parameters are found for worm gear. The next step is to check, whether this set of parameters are valid or not.

The simulation of drive characteristic curves is carried out. Principally, the setup of simulation is the same as the test bench in verification of worm gear model. So, the setup is not shown here. The simulation result is presented in Fig. 4.42. The two long lines are result from simulation, while the short lines are fitting results of measurements. Clearly, there is a gap between the two sets of curvers. The fact is that the gap is constant over the range from 1 Nm to 6 Nm. In another word, the two set of curves are parallel. In a close look, simulated drive has a higher rotational speed and lower current consumption compared with measured drive at the same point of output torque. It means that the simulated drive is more efficient and more powerful. In the mathematical description of drive models, there is still a unidentified parameter, that is, Coulomb friction loss in worm gear housing M_{gc}. This gap can help to identify its value. In Fig. 4.43, the torque difference of the two curves is about $0.4097Nm$. This value is applied to parameter M_{gc}. Drive characteristic curves are simulated again.

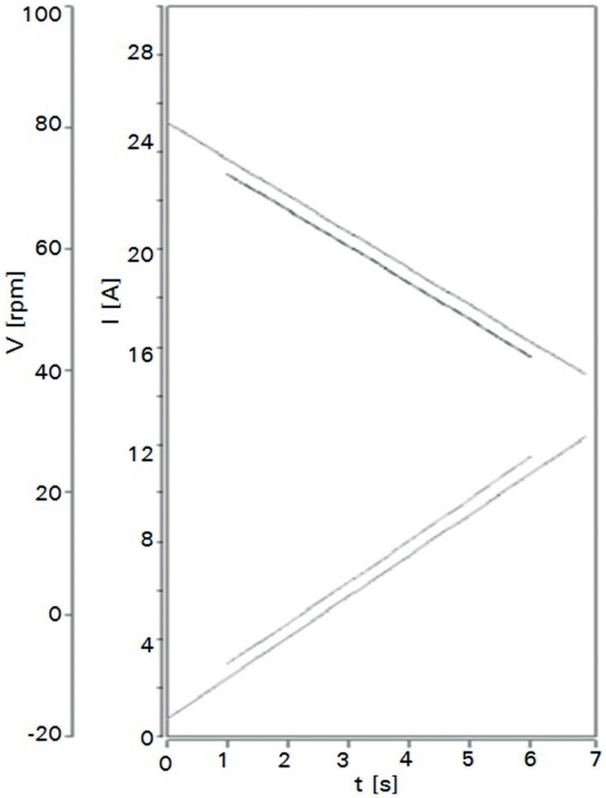

Figure 4.42: Torque difference

A quantitative comparison between simulated and fitting characteristic curves is in Fig. 4.44. The difference in rotational velocity is less than 0.23%, while in current is 3.6%. Within the working range, this comparison result can already satisfy the requirements to drive models.

In the end, the simulated characteristic curves of WR drive is compared with measurements. The two bold curves are results from simulation. The rest curves are measurements. The working range is marked with two vertical lines in Fig. 4.45, from 1 Nm to 6 Nm. Within working range, simulated curves overlap measurements. In the range of low torque, simulated results fit to measurements also in a fine way. Simu-

Figure 4.43: Torque difference

Torque gear N*m	Sim Velocity gear	Velocity gear fitting	Difference velocity	Sim Current	Current	Difference current
1.0077	72.357	72.351	0.008292218	3.0951	2.9826	3.634777552
2.046	66.16	66.118	0.063482467	4.8424	4.7289	2.343879068
3.001	60.529	60.385	0.237902493	6.449	6.3335	1.790975345
4.041	54.229	54.13	0.182559147	8.2017	8.1148	1.059536438
5.0168	48.316	48.266	0.103485388	9.8448	9.8064	0.390053632

Figure 4.44: Quantitative comparison of simulated characteristic curves and fitting of measurements

lated curves do not deviate from the extension of measurements much. As torque turns bigger than $6Nm$, the gaps in velocity and current turn also bigger. In this range, simulated current has a stronger deviation, compared to simulated velocity. The reason is that additional friction losses are brought into drives as load becomes more. The additional friction goes into contacting face of worm wheel and gear wheel and it goes also into bearings in worm gear housing. This part of friction is not in drive model. It leads that simulated drives are stronger and more efficient than real drives.

The identified power transmission efficiency can not represent the real efficiency in this range of strong torque. There are several methods to improve the coincidence in this range. One possible solution is to implement a torque-dependent power transmission efficiency of worm gear. Another possibility of improvement is to make M_{gc} dependent on output torque. As output torque becomes greater, Coulomb friction torque gets greater at the same time. It is also possible to introduce another parameter as additional friction torque When high load is applied.

Currently, the focus of simulating WR systems places on the working range. It is defined in the section of mathematical model of drive. In this range, the comparison shows that simulated curves go through the

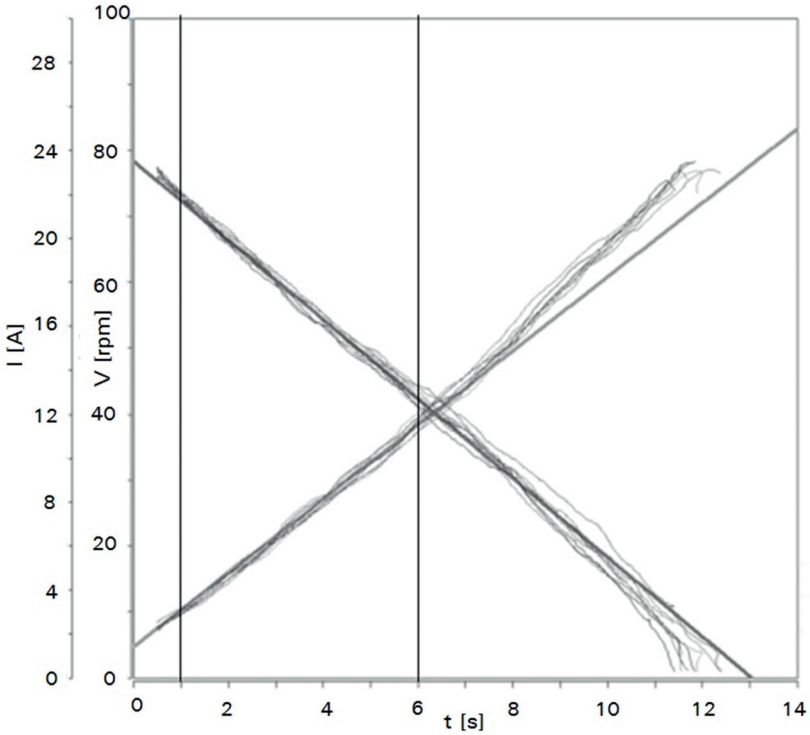

Figure 4.45: Comparison between simulation and measurements

channel formed by measured curves. It proves the validation of simulation models for WR drives. Therefore, the drive model can represent a group of WR drives within working range in simulations.

As mentioned in validation of DCPM motor model, it is possible to find lots of different combinations of parameters. The simulation with them can all fit very well with measurements. It is still true with drive model. If the working range changes a little bit, the fitting of measurements will result into a different curve. A slight difference in the curve slope will have a big impact of the calculation of power efficiency. As a result, comparison between simulations and measurements will have another outcome. Whether the outcome is good or bad depends on the criteria of evaluation. Between the complexity of models and the evaluation of

outcomes, a balance should be kept. This work presents a realization to build, verify and validate a drive models. Several proposals of improvement are also explained. Manual preparation of drive model is not advisory, because it deals with works in many steps. With measurement data of DCPM motor and drive available, automatic procedures can be created to cut, fit data and calculate necessary parameters, so that a library of WR drives can be built with good efficiency.

As a summary, drive model is created by integrating DCPM motor model, worm gear model and rubber damper model. The rotational velocity over torque is the most important criterion to determine the validation of drive model. The comparison shows that simulated speed curve has a good fitting to measurements in working range. It proofs the reliability of drive model so that it can be used in simulations later.

4.2 Rail guided cable driving window regulator Mechanism

In chapter two, three types of WR mechanisms are presented. In this section, the focus is placed on rail guided cable driving window mechanism (rail WR), because it is currently the mainstream. Although there are several variants, they are built up mostly by the standardized components. Therefore, this section begins with components modeling, followed by modeling mechanisms.

4.2.1 Components

Rail WR mechanism consists of common components of cable, cable drum, bowden cables, pulleys, sliders, compressing springs and rails. Component model places focus more on its influence on movement transformation and friction losses. The properties of mass and the inertia of them are neglected, because the kinetic energy of them are insignificant, in comparison to motor armature and window glass. The stiffness of cable is also not taken into account. At the end of production, cable in WR is in tension. During life time, tension in cable

decreases slowly. But cable elasticity is still greater than the rest of system. So, cable in model is taken as a rigid body.

Table 4.8: Kinetic energy of motor armature and window glass

Armature	$8.0e-06\,\mathrm{kg/m^2}$	Rot. Speed	$398\,\mathrm{rad/s}$	E_k	$0.637\,\mathrm{J}$
Glass	$3\,\mathrm{kg}$	Speed	$0.12\,\mathrm{m/s}$	E_k	$0.021\,\mathrm{J}$

4.2.1.1 Cable drum

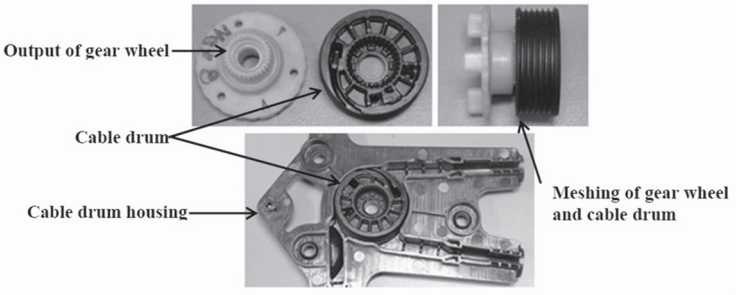

Figure 4.46: Cable drum

Cable drum connects drive and cable. It transforms movement, so that cable drives window upwards or downwards. Seen in Fig. 4.46, cable drum clenches drive gear tightly through its inner pinion. Each side of drum locks one end of cable. The channels on periphery guide cable to wrap over drum. Cable goes through two channels formed in cable drum housing to connect other components. Drive is also screwed on cable drum housing, so as to fix the relative position of drive and cable drum.

a) Mathematical description and model

In a simple way, cable drum can be imagined as a composition of two windlasses, with each windlass connecting to one cable. The two windlasses have the same radius. So, cables from two side have the same position and displacement all the time, when cable deformation is neglected. The resultant torque is then the sum of torque from two windlasses. Another effect which has to be considered is friction losses. The

sliding friction takes place between shaft and drive gear The two cable forces F_{c1} F_{c2} results a normal force F_{cn} pushing cable drum against drive gear and as consequence drive gear is pushed against shaft. When drive runs without cable drum, the friction torque M_{cf} at shaft is very small because the normal force F_{cn} pressing gear against shaft is minimal. Only when drum with wrapped cable meshes drive, there is noticeable friction torque at drive shaft. The amplitude of friction losses depends on the normal force F_{cn}, friction coefficient μ_{gs} and radius of gear shaft r_{gs}. Normal force has dependency on cable forces F_{c1} F_{c2} and angle between two cables α_c.

$$S_{cd} = \varphi_{cd} * r_{cd} = S_{c1} = S_{c2} \tag{4.36a}$$
$$M_{cd} = M_c + M_{cf} \tag{4.36b}$$
$$M_c = r_{cd} \cdot (F_{c1} - F_{c2}), (F_{c1}, F_{c2} \geq 0) \tag{4.36c}$$
$$M_{cf} = \mu_{gs} \cdot F_{cn} \cdot r_{gs} \tag{4.36d}$$
$$F_{cn} = \sqrt{{F_{c1}}^2 + {F_{c1}}^2 - 2\cos(\alpha_c) F_{c1} F_{c2}} \tag{4.36e}$$
$$\eta_{cd} = \frac{M_c}{M_{cd}} \tag{4.36f}$$

where
S_{cd}: peripheral translational displacement of cable drum
φ_c: angle change of cable drum
S_{c1}: peripheral translational displacement of cable 1
S_{c2}: peripheral translational displacement of cable 2
M_{cd}: torque of cable drum to drive
M_c: torque resulted from cable forces
M_{cf}: torque resulted from friction in cable drum
η_{cd}: ratio between resultant torque and driving torque

Eq. 4.36 are the mathematical description of cable drum. The model is shown in Fig. 4.47. The model has a short list of parameters. The name of parameters and their definition are in Tab. 4.9.

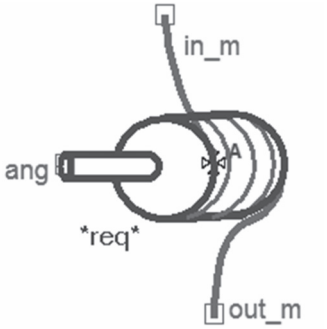

Figure 4.47: Model of cable drum

Table 4.9: Parameters of cable drum model

Parameter	Definition
r_{cd}	wrapping radius of cable
r_{gs}	radius of gear shaft
α_c	angle between two cables
μ_{gs}	Coulomb friction coefficient between gear and shaft

b) Parameters and identification

Basically, three sources or methods are provided for parameter identification.

- Drawings
- Handbooks
- Experiments

The identification of the dimensional information succeeds with technical drawings. To increase the creditability, it is also not a big effort to make measurement in the real component or in the assembly of WR, with tools like vernier caliper and angle gauge. However, it is always a topic how to ascertain a precise value of friction coefficient.

Mechanical handbook and tribology data bank provide one way to identify friction coefficient. In WR drive, drive gear is usually made of Polyoxymethylene (POM). Gear shaft has two variants, the traditional is from steel and the new-coming is from Polypropylene (PP).

Friction and wear between plastics and steel usually depend on factors of hardness and roughness of steel surface, load and sliding surface temperature. The dry friction coefficient between POM and steel has a range from 0.15 to 0.20 [95]. For plastic material coupling, the adhesive behavior, which is related to energy loss at contacting surface, is a factor for friction. The relation is determined often by experiments. Another important factor, which should be considered, is lubrication. In gear housing, grease is smeared at contact between worm and gear and at contact between gear and shaft. With using grease, friction coefficient between gear and shaft decreases further [95].

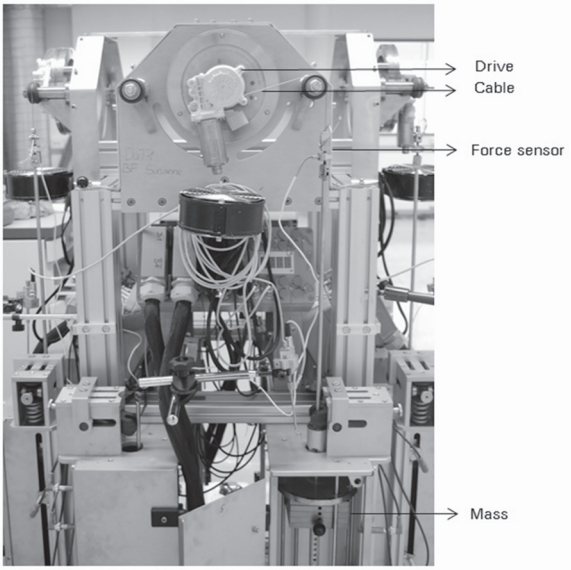

Figure 4.48: Drive test stand

As supplement, measurement can be designed and conducted to find friction losses or coefficient at drive gear and its shaft. Ideally if torque generated by drive and effective torque to pull cables are known, the difference between the two torques is then the loss resulted by friction. The effective torque can be calculated by equation 4.36c. But the generated torque can be measured indirectly and afterwards calculated. In

the test stand in Fig. 4.48, drive together with cable drum is fixed on the fixture. One cable is wrapped on cable drum and is pulled by mass around a pulley with ball bearing. The pulling force in cable is measured by force sensor. While drive is powered to turn in two directions, the current and voltage are recorded. With measured cable force and known radius of cable drum, effective torque is available. To obtain the generated torque, measured current and voltage are mapped through drive characteristic curves, which defines relation among drive velocity, current and torque. With the torque difference known, friction coefficient can be calculated. The value of friction coefficient varies itself from motor to motor and from project to project. In the simulation model of cable cable, the friction coefficient is guided to set in range from 0.06 to 0.20.

4.2.1.2 Bowden cable

Bowden cable (bowden) is used in WR system with the purpose to regulate the course of cable so as to bypass other components in vehicle doors. It is preferred not to employ bowden, because bowden brings friction loss. The friction loss in bowden is the effect to be studied and described in model. The shape and bending of bowden are not taken into consideration.

a) Mathematical description and model

Based on the assumption that cable is rigid and does not have mass, the two ends of bowden have always the same position changes and the forces are calculated according to captstan equation [96, 97] or belt friction equation. Seen in Fig. 4.49, a bowden is from point A to point B with wrap angle α and friction coefficient μ between coupling material. When cable is pulled to move into bowden at B and out at A, pulling force F_a has relation to F_b as Eq. 4.37a.

$$F_a = F_b \cdot e^{\mu \cdot \alpha} \tag{4.37a}$$

$$F_r = F_a - F_b = F_b \cdot (1 - e^{\mu \cdot \alpha}) \tag{4.37b}$$

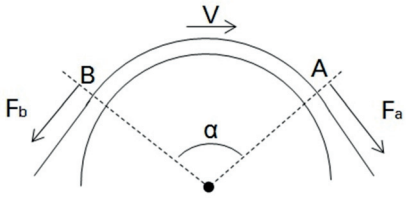

Figure 4.49: Forces in bowden

To be valid when cable is pulled from point B, the relation has then form 4.38a.

$$F_a = F_b \cdot e^{\mu \cdot \alpha \cdot sgn(V)} \tag{4.38a}$$

$$\eta = \frac{F_b}{F_a} = e^{-\mu \cdot \alpha \cdot sgn(V)} \tag{4.38b}$$

b) Parameters and identification

The two parameters of bowden model are wrap angle α and friction coefficient μ. The value of wrap angle can be identified with design of WR and drawings.

Similar to drum, it is quite complicated to determine value of friction coefficient in bowden, because it depends on lots of different factors, such as

- Coupling materials. Basically, the two coupling materials have fundamental influences. In WR application, inner tube of bowden is from POM and polyethylene (PE). Cable is normally from steel.
- Winding pattern, surface coating and treatment of cable
- Wears. As wears increase during lift time, friction coefficient increases.
- Temperature. Temperature is another important factor, when one of the coupling materials is plastic.

The friction loss in bowden is measured. From it, friction coefficient can be estimated. The left side of Fig. 4.50 shows that a bowden is fixed on test stand, with a wrap angle as 180°. The two ends of cable are

each pulled by a servo drive. In one run, cable is pulled from left side and the servo drive on the right side serves as load. In the next run, the situation reverses. The force sensors in servo drive measure all the time pulling forces in both side. Such test is carried out with several samples of bowden from one type under three temperatures. The processes of measurement data show the dependence of friction coefficient in bowden on temperature. On the right side of Fig. 4.50, we see that friction coefficient is relatively constant at 0.08 over a temperature range from $20°C$ to $80°C$. Under $-30°C$, friction coefficient increases dramatically to 0.20. Such result provides a basis to assign value of friction coefficient in bowden model.

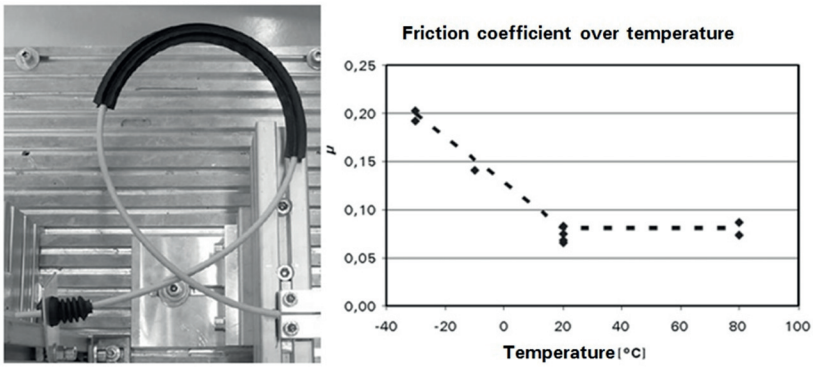

Figure 4.50: Bowden measurement and friction coefficient

4.2.1.3 Pulley

The sub assembly of rail and pulleys is used to change the path of cable and to guide the movement of sliders, shown in Fig. 2.1. Generally, there are two types of pulleys in WR systems.

1. One type is non-rotatable pulley. It means that pulley does not rotate as cable slips. It deals with dry friction, because relative movement is between cable and pulley. Modeling such type of pulley is similar to bowden in the last section, with wrap angle and friction coefficient as parameters.

2. The other type of pulley is rotatable pulley. Pulleys are riveted on rail and rotate along cable around shaft. Model of rotatable pulley is presented in this section.

a) Mathematical description and model

Compared to glass, mass of pulley is hundred times smaller and the buildup of kinetic energy in pulley is so small that it can be neglected. Hence, mass of pulley is not considered in model but only the friction between pulley and its shaft.

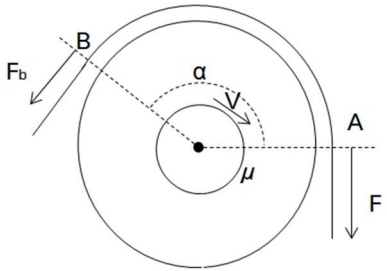

Figure 4.51: Pulley

When cable moves around pulley from point B to point A in Fig. 4.51, F_a indicates the force from the driving side, while F_b indicates the force from the driven side. The relation is described in Eq. 4.39a, where F_f is the effective friction force. It is calculated in Eq. 4.39b. Calculation of normal force F_n is similar to the one in drum.

$$F_a = F_b + F_f \tag{4.39a}$$

$$F_f = \frac{F_n \cdot \mu \cdot sgn(V) \cdot r_{in}}{r_{out}} \tag{4.39b}$$

$$F_n = \sqrt{{F_a}^2 + {F_b}^2 - 2\cos(\alpha)F_aF_b} \tag{4.39c}$$

$$\eta = \frac{F_b}{F_a} \tag{4.39d}$$

Where μ: friction coefficient between pulley and its shaft
V: velocity of cable
r_{in}: radius of pulley shaft
r_{out}: wrapping radius of cable over pulley
α: wrapping angle of cable over pulley
η: ratio of cable force
Because cable is seen as rigid, the positions of A and B are equal.

b) Parameter identification
Model of pulley involves parameters, radius of shaft r_{in}, radius of pulley r_{out}, wrap angle of cable α and friction coefficient between shaft and pulley μ. The values of the first three parameters in simulation can be determined by checking technical drawings. Wrap angle in real systems may have deviation from design, but it can be easily measured and calculated. As a result, its impact on normal force is insignificant. In contrary, friction coefficient has more influence. Similarly to drum and bowden, friction coefficient can be identified in one way through tribology data bank, with known coupling material and lubrication. Further, we designed and carried out experiments to investigate friction in different types of pulleys.

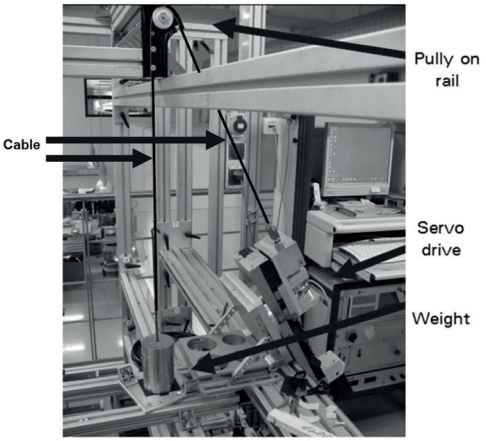

Figure 4.52: Pulley measurement

Setup is shown in Fig. 4.52. One cable around pulley is pulled by weight, while the other is connected to servo drive with force sensor. In one run, weight is pulled, while pulling in the other run. Pulling and being pulled are repeated for several cycles. From one test, the average ratio of cable forces η was 0.96, with wrap angle α as 162°, outer diameter r_{out} as 40mm and shaft diameter r_{in} as 12mm. It gives friction coefficient 0.069.As pulley wears against cable and shaft, friction coefficient increases. In simulation, this value is suggested to set in range from 0.04 to 0.15.

4.2.1.4 Compressing spring

Compressing spring can be named in another way to be "compensation spring", shown in Fig. 2.1. Normally a WR system has two compressing springs. Although they can be applied in different location in systems, they have the same functions. One of the most important functions is to keep the system slack constantly in the defined range. During lifetime, plastic parts, like cable drum and pulley, wears strongly because of friction. The decrease of pulley and cable drum diameters leads to cable prolongation. In this case, cable could go out of pulley canals, which is fatal to WR. Without compensation of cable prolongation, the accuracy of glass position can not be kept and it is critical for systems regulated by electronics, especially for short stroke function in frameless doors. Additionally, compressing spring assists the movement of cable at start up after system is for long time stalled in cold environment. For this purpose, strong spring is usually employed.

From another perspective, compressing spring has influence on system stiffness, because its deformation is visible in comparison with other plastic and metal components. Meanwhile, the deformation also indicates the tension distribution in systems. Regarding the questions how the indication works and why, it is too complex to explain without the context of whole WR systems. Therefore, the discussion of such doubts will be continued in the next section "Mechanism". Here, the focus is the elasticity of compressing spring.

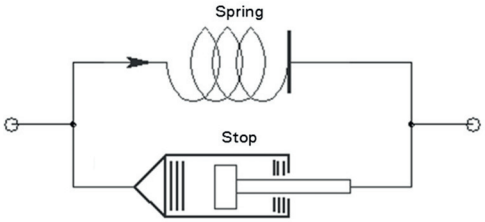

Figure 4.53: Model of compressing spring

In WR mechanism, compressing spring has two working cases. In one case, spring is in normal linear range. In the other case, spring goes into block. In normal loading range, compressing spring has stiffness ranging from 1000N/m to 6000N/m and elastic force ranging from 25N to 140N. In block, coils touch each other and effective stiffness increases exponentially. The transition from working range to block and back to working range is described in model of compressing spring. It can be realized by parallel connection of a translational spring model and a stop model, in Fig. 4.53. The stop model restricts translational motion of a slide in two direction with two stops. When slide moves within defined range, no force is applied. When slide goes out of range, it hits stop. The interaction force between slide and stop is equal to the product of stop stiffness and deformation. In such combination, stiffness of compressing spring in normal loading range is set to stiffness of spring model, while block stiffness and max deformation are assigned in stop model.

4.2.1.5 Slider

In WRs, slider is a multi-face connector, shown in Fig. 2.1 and 4.54. Its interfaces are

- Two cables. One comes from upper side and the other one goes into lower side.
- Window glass
- Guide rail.

The motion in cable are either lifting up or pulling down. It is transferred from cable to glass under the constrain of path formed by rail. Slider exerts itself to move glass with as less as possible deviation from the defined track, as the unwanted interaction between glass and sealing could lead to dramatic system load and also acoustic issues.

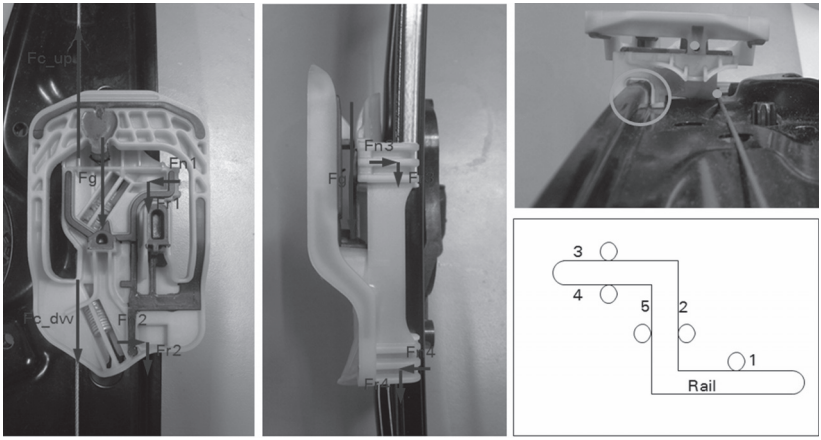

Figure 4.54: Slider

a) Mathematical description and model
Basically, slider plays a role as force distributor. In the case of lifting glass up, the force equilibrium is as Eq. 4.40,

$$F_{c\_up} = F_{c\_dw} + F_g + F_r \tag{4.40}$$

where F_{c_up}: Upper cable force
F_{c_dw}: Lower cable force
F_g: Force from glass
F_r: Dry friction force.

Glass force contain not only the gravitation force but also forces resulted from the interaction between glass and door. The interaction force contains sealing friction force and reaction force, when glass en-

counters obstacle, and so on. Friction force is the representative force for all frictional losses from the interaction between slider, cable and rail. With a close look, frictional force incorporates forces induced in different contacting spots between slider and rail, shown in Fig. 4.54. It is the direct outcome of the design of guide rail. Slider fits around rail through two pads. The material of pad is not the same as the slider material. It provides a low friction coefficient against rail. To obtain a small contacting surface, pad touches rail with tiny hemispheres. Contacting spots are supposed to be limited at the five positions, in bottom right corner of Fig. 4.54. Due to the fact that cable forces and glass force are not on the same line of action, torque is produced to bend slider against rail. These bending torques could be in two sections, which result to normal forces between slider pads and rail. The normal forces are marked with n and shown in left and middle pictures of Fig. 4.54, for example, F_{n1} and F_{n2}. During slider moving along rail, corresponding Coulomb frictions forces are expected.

b) Parameter identification

In model of slider, upper and lower cable forces will be automatically calculated in simulation when slider model interacts with pulley models through cable. Glass force will be supplied from door model, in which glass force, sealing friction force and other forces are all calculated. The friction force in slider model is the only force, which is left to be settled.

A straightforward idea to determine overall friction force is to sum up all frictional forces, with known cable forces, glass force, necessary dimension information and friction coefficient. Dimension information regarding slider can be abstracted from drawing. Friction coefficient between pads and rail can be searched in tribology data bank. The friction coefficient has a range from 0.05 to 0.15 for the WR in picture. However, it is not sure that contacts always take place at the same time on all five spots at each pad. One of the reasons for it is that slider is designed to have slack between pads and rail, so as to achieve an easy assembly. Furthermore, many factors have influence on the clearance between pads and rail and hence effect the presence of normal

forces. The factors are like tension in cables, production process and so on. From the other side, it is for sure that huge efforts are going to involve in verification and validation of each friction forces, if slider model is built based on detailed anaylsis of forces. These effort includes searching suitable force sensor, amounting sensor in slider, setting up measurement environment, analyzing measurement result and so on.

Another approach is to sum all frictional effect in one. Its dependency can be experimentally determined with tests and measurements. From one side, it saves the burden to investigate each single single friction force. From the other side, the parametrization is simplified for the later usage of slider model. The characteristic friction of difference designs of sliders can be integrated into the corresponding classes in model. Once a type of slider model is selected in simulation, the characteristic friction is taken into effect at the same time.

To determine the dependency of friction, we built up and carried out measurement as in Fig. 4.55. In the picture, it is a WR for front door at passenger side. Guide rail marked with 2 is close to A pillar in cars, so it is named rail A. It is the similar with rail B. Window regulator is fixed on a plate. The situation of fixing points is the same as in real doors. Glass is replaced by an aluminum dummy, since there is not guidance of door sealing. The dummy applies forces to slider A and B with a constant ratio. The ratio simulates the load distribution on sliders. As to the presented case, approximate 60% of force from load spring is distributed to slider B, while 40% is to slider A. During testing, the motion is supplied by a wrench. As wrench is rotated, cable forces on top and at bottom of rail B, driving torque and load force are measured. Besides measurement with load, system is measured also under no load.

One measurement result and its analysis are shown in Fig. 4.56. The measurement of two cable forces at rail B under no-load condition helps to obtain a basic imagination of the starting point of sliding friction. Here, the friction force for slider B is about 5 N, calculated by subtract-

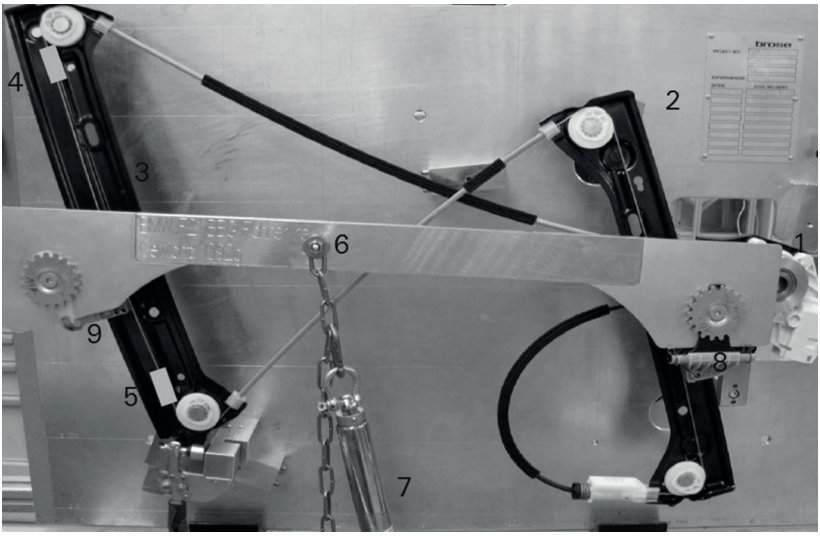

Figure 4.55: Slider friction measurement
1. Torque wrench and sensor 2. Rail A 3. Rail B 4.5. Cable force sensor 6. Aluminum dummy 7. Load spring and sensor 8. Slider A 9. Slider B

ing bottom force from top force. Predictably, as the driving torque increases, all other measured variables increase. Due to the poor resolution of force sensors, which is about $\pm 30\,\mathrm{N}$, only measurement data in middle and high range of torque are used. The purpose is to minimize the impact of measurement error.

The measurement result in Fig. 4.56 shows the cable force difference over the change of load force. The basic linear fitting shows already a good quality with a squared residual of 0.9992. A quadratic function fitting does not improve the fitting quality dramatically. Therefore, linear fitting is selected to describe the dependency. In the next step, load force on slider B is seperated from whole load force, with known distribution ratio. And, friction force in slider is obtained by substracting cable force difference with load force on slider B. With load force and friction force on slider B, a linear dependency is built.

Drum torque @Nm	1.18	6	7	8	9	10	11	12	13	14	15
Load force @N	0	152	189	221	247	281	310	347	386	410	449
Cable force Bpillar top @N	82.6	271	310	347	375	413	448	490	534	568	605
Cable force Bpillar bot @N	77.3	148	162	177	189	205	216	230	246	265	276

Cable force Bpillar diff @N	5.3	123	148	170	186	208	232	260	288	303	329
Cable force diff @N	8.83	205.00	246.67	283.33	310.00	346.67	386.67	433.33	480.00	505.00	548.33

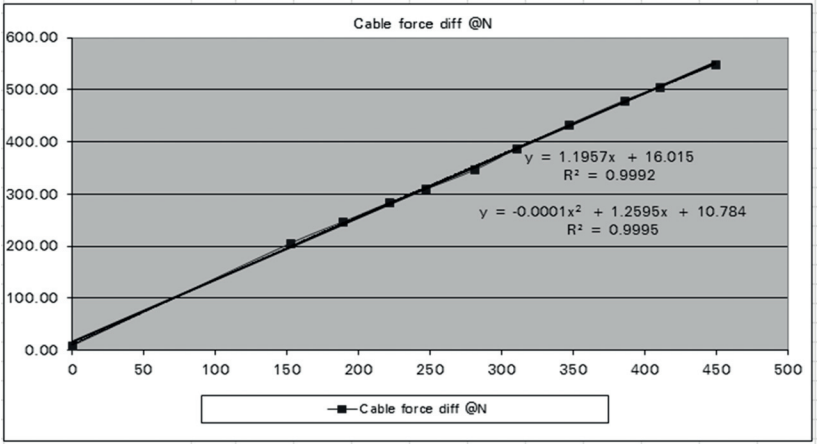

Figure 4.56: Slider friction measurement result
x-axis: Load force, force from load spring. y-axis: Cable force difference

In the implementation of slider model, each type of sliders are associated with two characteristic coefficients and distribution ratio. The measurement described in this section is repeated with other sliders, so that a library of slider models can be built up. Distribution ratio is determined with consideration of complete WR system design.

4.2.1.6 Remarks on component modeling

a) Modeling guide rail
Rail is not modeled as a component for simulating WR system. However, its most dominating features are included.

Firstly, rail is not always in longitudinal direction. Reduction angle is named to describe how much rail is deviated from longitude. The reduction angle is used for the purpose to calculate the projection of load force from glass in the longitudinal direction, while most forces in other

components are computed in the cable moving direction. As sliders are the interfaces to glass, all force from glass comes into slider. Therefore,reduction angle of rail is packed as a parameter in slider model. Longitudinal forces can be calculated then within slider models.

Secondly, rail has the function to limit stroke. When window glass touches the upper sealing of door, there is still a distance between slider and the top of rail. But, when glass moves down into door, the bottom of rail stops slider. In return, it stops glass. The stroke–limiting and stopping function is simulated with a stop model.

Thirdly, rail interacts with slider and friction is already modeled in slider model. It is not necessary to implement the friction interaction once again in rail model. And deformation of rail and its interaction with door plate are insignificant and then neglected.

Based on the reasons above, rail is not a component model for WR, but its effects are considered.

b) Identification of friction coefficient

Component modeling has the focus on the friction losses, which is influenced by factors, like wrap angle, outer and inner radius and friction coefficient. Friction coefficient has greater influence than other factors, like shape of bowden, length of cable and etc..

To measure the friction losses, efficiency is calculated in each component models. The accuracy of efficiency lays on the quality of parameters. With regard to wrap angle and radius, drawing is a stable source, but with tolerance. In production and assembling process, deviation could be brought in. However, with other parameters constant, such deviation has quite limited influence on efficiency for models of pulley and drum. For bowden model, the impact of wrap angle on efficiency is slightly greater. But, identification of bowden wrap angle is a combination of drawing and measurements, so as to reduce deviation. It is similar with radius of pulley and drum.

In contrary, friction coefficient has a higher degree of impact. The determination of its value is all the time complicated. It has been mentioned in the previous section that handbook could provide information on friction coefficient between certain coupling materials. But it reveals less information about the influence of geometry of the coupling subjects. An example is shown in the left picture in Fig. 4.57. It demonstrates a drum clenching gear of drive around shaft. F_1 and F_2 are the two cable forces. As the cable forces are not acting on the same line, it leads that the friction between drive gear and shaft does not even distributed on the contacting surface. Here, the bending of shaft is neglected. And the similar effect happens also to pulleys.

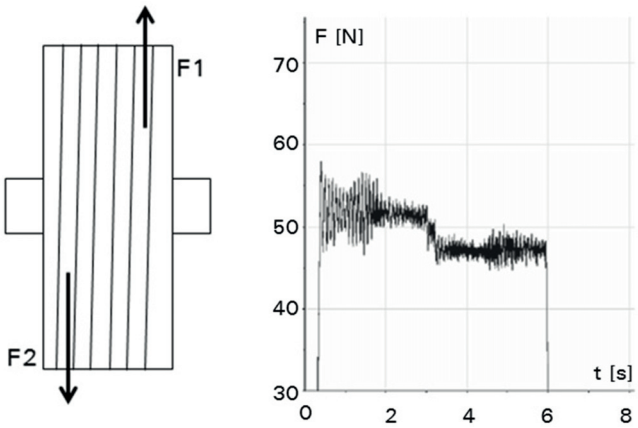

Figure 4.57: Cable drum tilting around shaft

As a supplement to handbook, frictional losses can also be measured in the similar geometrical and dynamical setup as in real systems. On the right side of Fig. 4.57, it is the measurement of cable force on pulley. One end of cable is pulled constantly with 50 N mass. The force of the other end is applied by a servo drive and metered with sensor. In the first half, cable is pulled by servo drive. In the other half of measurement, servo drive just lets the cable be pulled in the opposite direction. The noise in measurement result is from servo drive and force

sensor. The data is processed with filtering and averaging to obtain a mean value of cable force. With it, friction coefficient is derived, which represents the whole effective frictional losses.

It is presented here two methods.In the simulation models, a range is provided to guide end users to set a reasonable and suitable value. Meanwhile the possibility is also available for users of simulations to carefully tune parameters, so as to obtain the desired behavior.

4.2.2 Mechanism

4.2.2.1 System stiffness

Besides the friction losses in each single components, system stiffness is another important property considered in modeling WR. System stiffness defines the overall stiffness of WR mechanism. The stiffness refers to the one measured between cable drum and slides in the direction of glass moving upwards. During strokes, glass speed and motor rotation speed are relatively stable. Therefore, stiffness of WR does not play an important role. However, in the case that obstacle is encountered between glass and door frame, system stiffness has great influence on how quick electrical drive can sense the change in velocity and force and as a result how quick electronic system responds to the possible danger. Hence, it affects the performance of the safety functions.

An evaluation of responding time can be estimated as

$$\tau_{wr} = 2\pi\sqrt{\frac{M_2}{C_{wr}}} \tag{4.41}$$

where,
M_2: Mass of glass, the same as in analytical model in chapter 3
C_{wr}: System stiffness of WR mechanism
τ_{wr}: Evaluation of responding time of WR.

If system stiffness is higher, the state changes quicker in system, according to equation 4.41.

System stiffness, C_{wr}, is sum of stiffness distributed at every components in WR mechanism. Some components have higher stiffness, while other have lower ones. For example, metal and most plastic components are stiff and no visible deformation is seen. Cable is also quite stiff, after it is tensioned by pre-load and load forces. Compressing spring is the softest component, but when it goes into block state, the block stiffness is also very high.

Besides component stiffness, working conditions also make system stiffness difference from one case to another case. For example, one stroke can be divided into several segments. In each segments, system stiffness may distinguish from each other. One reason for it is that the load from glass to WR mechanism changes. Furthermore, when trapping event happens at various transverse positions, WR mechanism behaves with a different system stiffness. For instance with a front door, it makes difference when glass touches obstacle close to A pillar, B pillar or in middle of them.

It is difficult to make a clear analysis how stiffness of WR mechanism is made up from component stiffness, not only because of the facts mentioned above but also because of cable itself, which is the medium to transfer tension from electrical drive to glass. In different section of cable, the tension is not the same. The effective stiffness of cable is glass position dependent. An example is slider, where the upper cable force is greater than the lower cable force during glass moving upwards. At the same time, cable is pulled into drum from upper port and feeded from lower port. The tension in cable at upper port of drum is much higher than at lower port. In this manner, the tension is enough to drive upper compressing spring into block, which means high stiffness, while lower compressing spring demonstrates still its normal working stiffness. The tension in cable depends on more factors, for example, preloaded tension, friction losses through components, glass load and its distribution on two sliders in the case of double rail WR systems.

Even though stiffness of mechanism depends on lots of factors, it is necessary to have insights on its range. Generally, system with high stiffness leads to high trapping force, with the same setting applied. The direct outcome of high stiffness is that system respond is fast and delay is short. But when the anti–trap function needs a little longer time to react and reverses electrical drive, it results into more damage in trapping event in form of higher trapping force. Normally, a moderate system stiffness is preferred to cooperate with anti–trap function. In trapping event, a number of springs connects with each other in series, representing the stiffness of door, obstacle, mechanism, drive and door plate, on which WR is mounted. In such system, the components with lower stiffness plays more important role in determining the final stiffness. According to USA law, 65 N/ mm spring is required to measure trapping force. System stiffness needs to be cared in case of anti–trap failure, because system stiffness is low in comparison with 65 N/ mm. To avoid the complexity and maintain safety functionality, measurement of system stiffness is carried out at selected trapping spots.

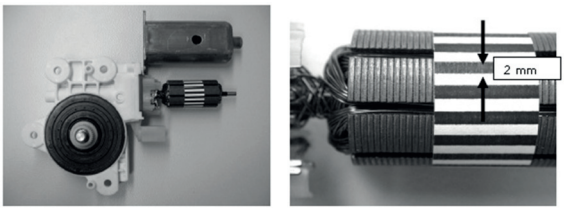

Figure 4.58: Measurement of motor rotation

In the measurements, WR is powered with electrical drive to perform trapping event. Obstacle is imitated by spring–like force guage, which records trapping force. Under the assumption that there is not system slack among drive, mechanism and glass, motor rotation is observed to represent glass movement by optical sensor with a light barrier attached on winding, shown in Fig. 4.58. It provides increased accuracy. Another method to measure motor rotation is to use the combination of Hall sensor and 4–pole ring magnet on motor rotor.

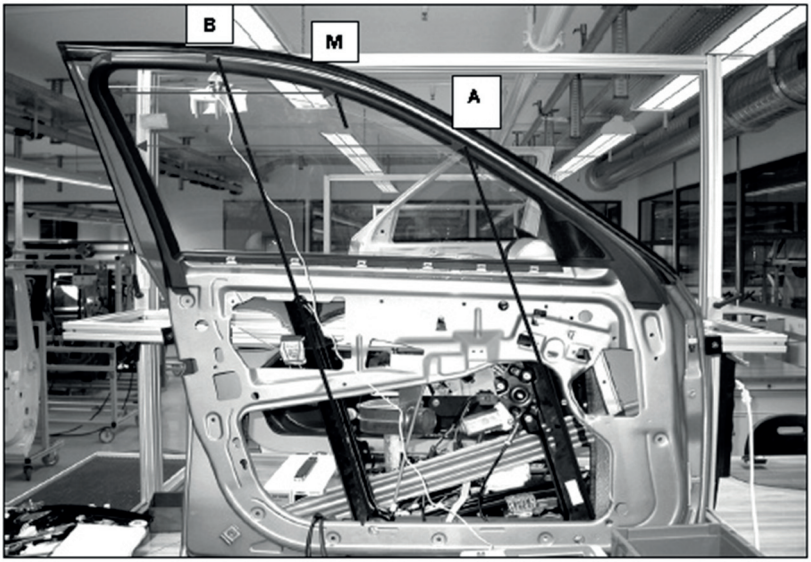

Figure 4.59: Locations of trappings and measurement force

The force gauge is placed each time at upper door frame over rail A, rail B and middle position between them, as shown in Fig. 4.59. In the measurement, anti–trap function is so configed to obtain a trapping force, which is more than 100N, for example in Fig. 4.60. The displacement of glass is converted from motor rotation with known drive gear ratio and drum radius. To obtain the best linearity from measurement result, trapping force is selected in range from $50N$ to $100N$. With it, a resultant stiffness can be calculated.

With measured resultant stiffness, system stiffness of WR can be calculated with Eq. 4.42. Door frame has usually high stiffness, so it is ignored. When drive is with rubber damper inside, its stiffness is a factor, which is measured and modeled in previous chapter.

$$\frac{1}{C} = \frac{1}{C_1} + \frac{1}{C_2} + \frac{1}{C_3} \tag{4.42}$$

where C: Resultant stiffness of measurement
C_1: Stiffness of force gauge
C_2: System stiffness of WR
C_3: Stiffness of rubber damper in gear wheel of electrical drive

With the example in Fig. 4.60, measured stiffness is 6.9N/mm, force gauge is 10N/mm and rubber damper has stiffness of 0.8Nm/°, which is converted to be 114.591N/mm. It yields that stiffness of WR mechanism is about 27.6236N/mm. In simulations, it is suggested to set value of system stiffness in range from 20N/mm to 40N/mm.

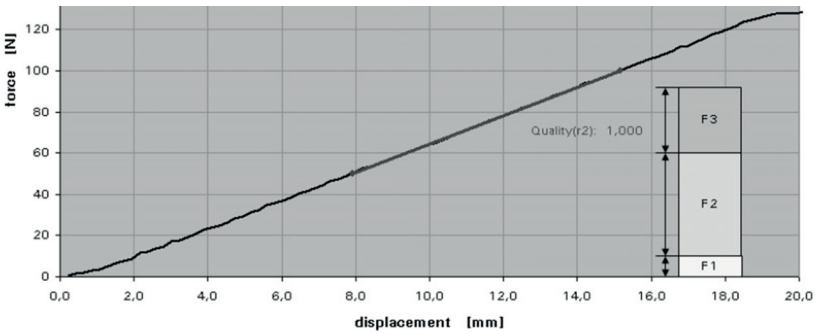

Figure 4.60: Measurement result and analysis

System stiffness has great influence on the dynamical behavior of WRs, not only during trapping event, but also at start–up of WR. The dynamical behavior of WR at start–up is observed through rotational speed of electrical drive. Typically, we see the vibration of drive speed at start–up over a short period. Figure 4.61 demonstrates two variants of speed vibration. The upper curves has a different amplitude of the first peak and a number of following vibration. The bottom curve does not have any vibration despite of the first peak. In the context of WR, stiffness of compressing spring plays an active role in affecting the system stiffness and hence affecting the speed vibration. To this purpose, the cases of speed vibration will be first classified and each will be discussed. Then model of compressing spring will be extended.

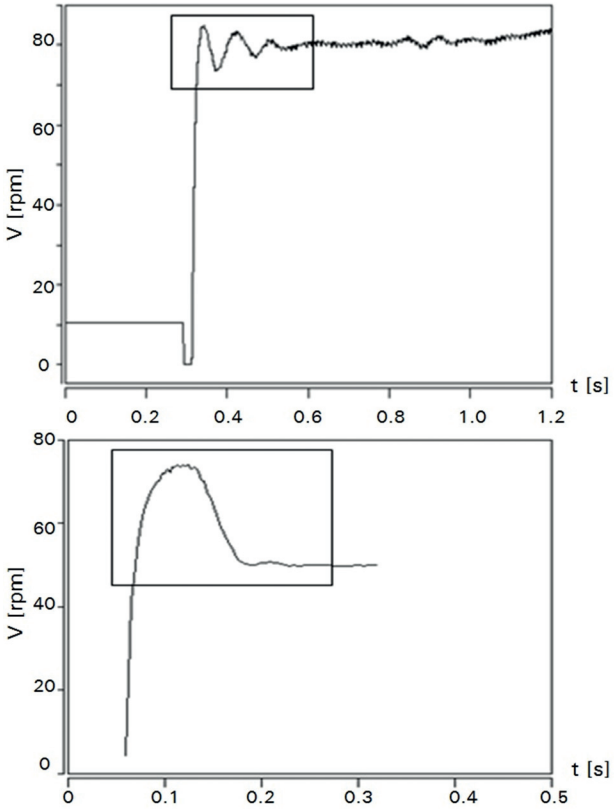

Figure 4.61: Motor speed at start–up
x-axis: time (s); y-axis: rotational velocity of electrical drive

4.2.2.2 Extension of compressing spring model

a)The model of compressing spring has to be extended.
First reason is the implementation of system stiffness. Instead of decentralizing in components, system stiffness is implemented as a property of compressing spring model, to keep model complexity in reasonable level and save parameter identification effort. As a result, system stiffness replaces block stiffness in compressing spring model in previous section 4.2.1.4.

The second reason is to set up tension and maintain tension during lifetime in the close loop cable system. There is always tension in cable system, even when the WR mechanism is detached from glass and electrical drive. The tension ensures that cable does not go out of the designated path. As cable goes around or through different components, tension is uneven, depending on its tendency and moving directions and its location in mechanism.

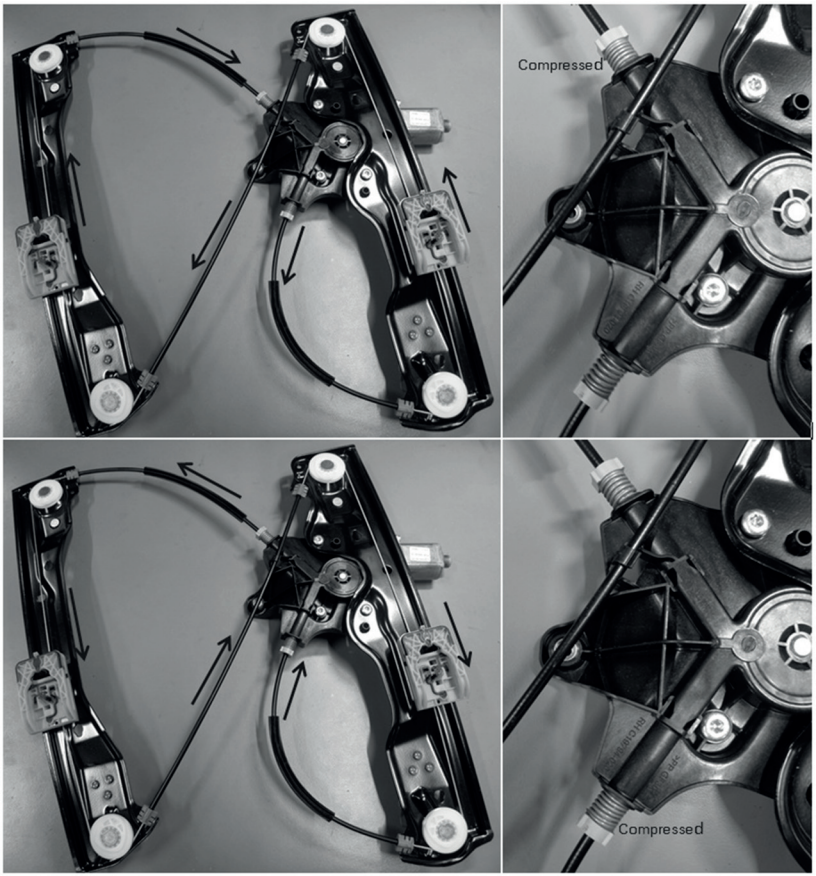

Figure 4.62: Cable moving directions and compressing spring states

The third reason is indication of tension in cable system. Cable tension is in form of force. Without cutting a bowden cable and inserting a force sensor, it is difficult to obtain the magnitude and variation of cable Here, compressing spring provides an "eye" to the tension distribution in mechanism, with its states of being pressed or released. Shown in Fig. 4.62, during moving upwards, the upper cable of cable drum is pulled into drum, acting as the main driving power. And the lower cable is pulled out of drum to feed in the cable loop. Therefore, in the upper cable there is greater tension, while it is less in the lower cable. Such tension distribution is indicated by the two compressing spring in the way that the upper spring is compressed and the lower is relatively at ease. In the other moving direction of glass, tension reverses and deformation of compressing spring reverses too.

One of the main purposes of compressing spring is to compensate the prolongation of cable over service cycle. So, the two compressing springs in mechanism are designed to be compressed all the time, although tension may shifted. In Fig. 4.62, it is a newly produced mechanism, therefore, it is not so obvious to see the deformation changes in springs.

b) Implementation of extension

Under such background, the realization of tension setup is to bring initial deformation in compressing springs. To achieve it, a spacer model is inserted in the previous model of compressing spring, see Fig. 4.63.

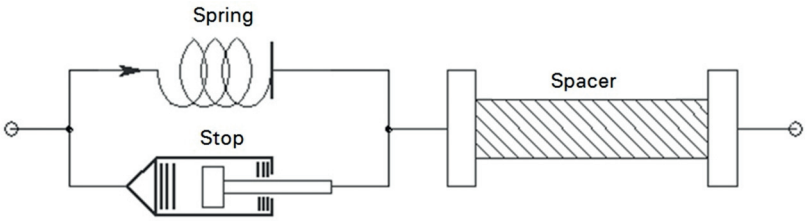

Figure 4.63: Extended model of compressing spring

Slack is not considered in modeling WR. Therefore, when cable drum is at zero degree. Position of slider is zero. Position of the two pins of

compressing spring are the same. Under the existence of spacer with a non-zero length, the normal translational spring has then a non-zero deformation. It brings a force to pull cable. In the way, tension is set up in a close loop cable system.

As the parameters of compressing spring are known from drawings, the tension in various applications of WR mechanism can be adjusted by setting the length of spacer. The sum of spacer length in two compressing spring model defines the total initial tension in mechanism. When WR drives glass up and down, the tension will automatically accordingly distributed, as shown in Fig. 4.62.

c)The improvement has meanings
Practically, without compressing spring model, simulation would encounter numerical problems, because the assembly of models results in rigid system. If the improvement is not carried out, simulation could also run, but the tension built up in cable loop is not able to represent real mechanisms. The credit on simulation decreases greatly.

Start from	Operation 1	Operation 2	Operation 3
Opposite direction	Down 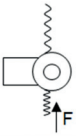	Stop	Up 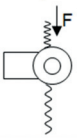
Same direction	Up 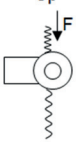	Stop	Up 

Figure 4.64: Startup from opposite and same directions

From another aspect, improvement of compressing spring model and tension setup in cable loop provide reasonable explanation to the phenomena of drive speed oscillation during system starts up in various situations, shown in Fig. 4.61. One thing in common is that these variants in Fig. 4.61 are all motor speed observed when glass is driven

upwards. It is interested, monitored and investigated because trapping event takes place when glass moves up. Comparison of the left two curves shows that one misses first peak and the other has it. The cause of difference is the operation sequence of start-up process. One sequence is named as start from opposite direction and the other is named as start from same direction. Starting from opposite direction means that WR is firstly operated to go down, then stop and go up, while starting from same direction does not involve operation direction change. That means it always moving up. Graphically, the two operations and the states of the two compressing springs are illustration in Fig. 4.64. When operation changes from going down to going up, lower spring gets to relax from being compressed and upper one gets compressed from being relaxing. This transition does not require much power from drive and can be finished in a short time. Therefore, the motor speed increased sharply. And it leads to the first peak, shown in the top left curve in Fig. 4.61 In case of starting from same direction, tension does not require to redistribute. So, motor senses load from regulator mechanism directly. As a result, the motor speed in the bottom left curve increases relatively slow. From this sense, motor speed curve can be divided into two parts. One part is the first speed peak, resulted from tension rebuild in cable loop, and the second part is the speed oscillation after the first peak, which is system oscillation. The implementation of system stiffness and the extension of compressing spring model provide the access to rebuild motor speed oscillation in simulation with concentrated parameters.

4.2.2.3 Variants of rail window regulator

Model of WR mechanism is an assembly of component models. The example in Fig. 4.65 is an model assembly for double rail WR mechanism. On the left side, component models interconnect with each other in the order of the real systems. The assembly has two pins, with names “shaft” and “glass”, to connect electrical drive and window glass. On the right side, it is the macro model. Instead of wiring component models, the connection in macro model is organized in VHDL source file.

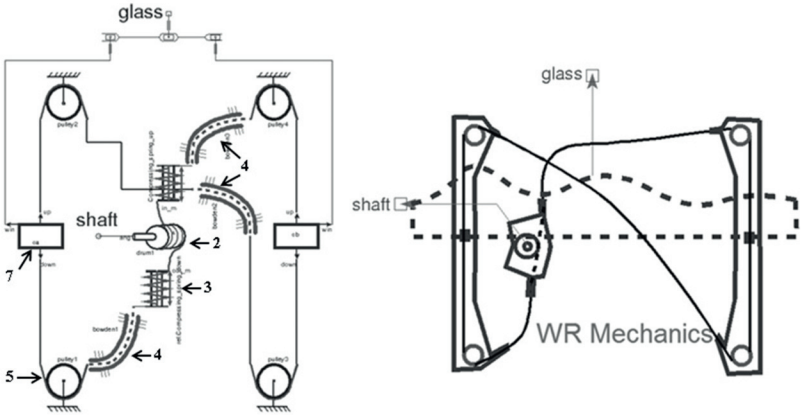

Figure 4.65: Model assembly of window regulator mechanism
2. Cable drum housing 3. Compensation spring
4. Bowden cable and cable 5. Pulley 7. Glass slider(carrier)

The model assembly has great meaning in explaining model content, while it is more convenient to use macro model in system simulations.

The variants of cable driven WR mechanism can be firstly grouped by number of rails. There are double rail and single rail mechanism. The further classification of each groups depends on whether bowdens are deployed and also its quantity. Mostly, double rail mechanism comes with three bowdens, as in Fig. 4.62 and 4.65. When regulator is integrated to door plate, bowden then can be removed. When the bowdens between drum and pulley are dismissed, the compressing springs in between will shift into rail slider in real system. Similar situation with bowdens is also common for single rail regulators.

Although there are many variants of WRs, modeling of WR mechanism can be easily adjusted by reconnecting components models in the order of real systems. For example, in modeling of bowden–less WR system, model of compressing spring is simply moved to be next to slider model, in the same way as the real system. The model of WR mechanism have always one pin to connect with mechanical door model. Such design of fixed interface makes it convenient to alter model in system simulations.

4.3 Additional components for window regulator system in working environment

4.3.1 Mechanical system of car door

Figure 4.66: Front and rear door

As to WR system, the mechanical structure of car door has the function to constrain the movement of glass in designated path. The path is formed by sealing grooves at A, B and C pillars, shown in Fig. 4.66. When glass moves in sealings, the friction applies to glass, then it is transferred into WR mechanism and in the end it becomes the load of electrical drive. The model of door is built in the way that it has one pin to interface WR mechanism and another two pins, representing each top edge of glass and upper door frame. Under the working condition without trapping event, one pin to interface mechanism is enough. When trapping event happens, obstacle is pressed between glass edge and door frame. For this reason, the other pins are inserted and between them the model of anti-trap gauge is placed, which will be explained in the following section.

4.3.1.1 Sealing friction and upper frame stiffness

Two important behaviors of mechanism car door are modeled, that is, sealing friction and upper frame stiffness. Sealing friction, as discussed

before, is the mechanical load to WR mechanism. Regarding upper frame, different car manufacturers have various designs of frame sealing. It means that frame sealing has different stiffness. Frame sealing has influence on choosing motor gear wheel, either one piece gear wheel or gear wheel with rubber damper inside. When the upper frame sealing is very stiff(in another word, hard), after being stalled in upper frame for long time, it leads to deformation in gear wheel. As a result, electrical drive may not be able to pull down glass again. In this case, rubber damper is necessary in gear wheel to reduce the stiffness.

In a normal car door with frame, it contains four sealings, top frame sealing, sealings at A pillar and at B pillar, and horizontal sealing. In regards to rear door, difference are sealings at B and C pillars. Despite of these differences, the modeling principle is the same, here, a front door is taken as an example. The classic method to calculate dry friction between objects is

$$F_r = F_N \cdot \mu \tag{4.43}$$

where F_N: Normal force
μ: Friction coefficient
F_r: Friction force

Because glass usually goes up and down in low speed, between $0.08\,\mathrm{m/s}$ and $0.1\,5\mathrm{m/s}$, the viscous friction is not considered. When material of glass and sealing rubber are determined, it is assumed that friction coefficient is constant over the whole stroke of glass movement. In calculating friction, it is well known that friction does not depend on the contacting area or length. In the case of sealing, the friction does not directly depend on contacting length but in directly, because normal force between sealing and glass is length dependent.

The initial contacting length between glass and sealing is L_0, as in Fig.4.67. When the glass moves in the direction V for a short time, the contacting length increases for L_Δ. The same movement is demonstrated in cross section. When the sealing is in relaxing state, in another word, glass is not between sealing, the inner and outer lips of sealing

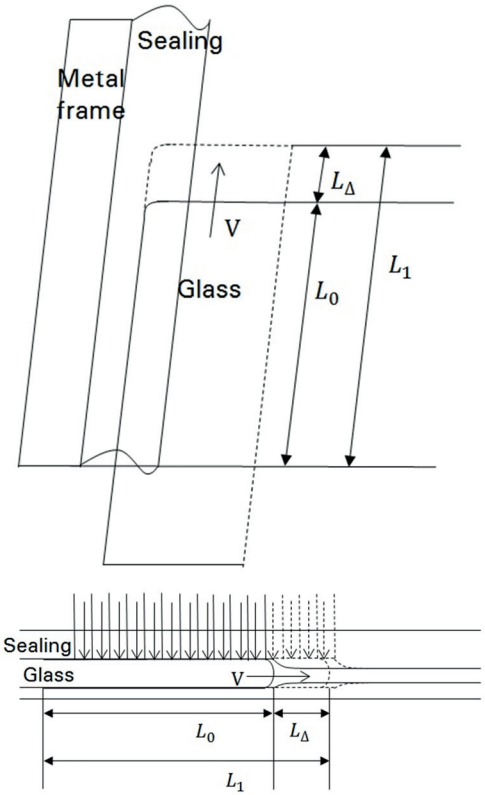

Figure 4.67: Glass movement in sealing and normal force

have a relatively small slot. When glass is between sealing, the slot is widened. The rubber sealing then presses on glass. Sealing is made of the same material and in the same shade, therefore, it applies the same stress under the same strain. If the sealing is cut into many identical segments as in Fig. 4.67, then each segment would apply the same pressure on glass. As glass goes further and the contacting length increases, the pressing force, which is at the same time normal force, increases. In this manner, the normal force of sealing friction is dependent on the contacting length. As a result, the sealing friction than depends also on the contacting length.

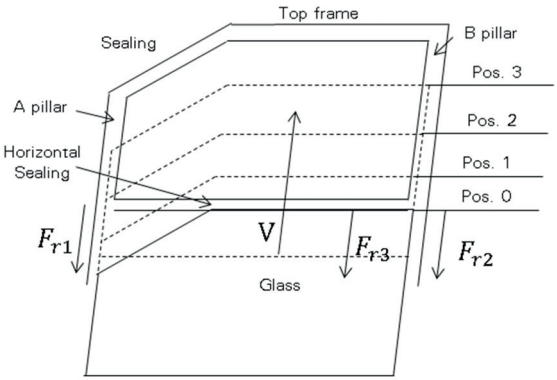

Figure 4.68: Sealing friction force

Length-dependent friction can be applied to sealing at A, B and C pillars and also horizontal sealing. With the front door in Fig. 4.68 as an example, F_{r1}, F_{r2} and F_{r3} indicates each friction at A and B pillars and horizontal sealing. The change of friction force depends each on their contacting length between glass and sealings. As glasses goes from the bottom to the top, the change of each contacting length depends on the initial contacting length and also the length of the edge of glass. It can be imagined that, as in Fig. 4.68, F_{r3} starts from initial value to increase and reaches the maximal value when glass gets to position 2. When glass reaches position 3, maximal F_{r1} is achieved. Then only after glass gets to the top frame, F_{r2} has its max value. Despite of this example, there are lots of variants, depending on whether it is front door or rear door, initial contacting length, edge length of glass and so on. To identify the overall sealing friction through friction in each sealing, it deals with describing glass geometry and it is effort costing. However, no matter how complicated it is, it is clear that overall sealing friction force increases, as glass goes upwards. It is not only a conclusion from the analysis above but also from many applications of WR projects and measurements of door friction force. Fig. 4.69 shows measurement of sealing friction force by lifting glass with force sensor.

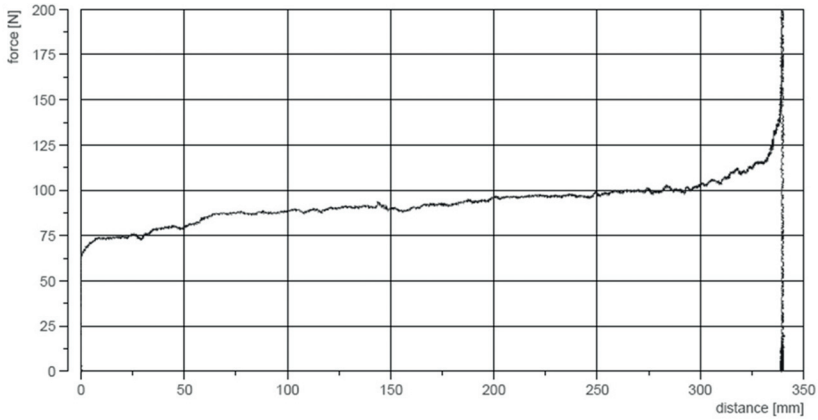

Figure 4.69: Measurement of sealing friction force
x-axis: Displacement of glass in mm, with glass fully opened state as zero position y-axis: Friction force

Based on the analysis above, consideration of identification effort and experiences from measurements, the complete friction force between glass and sealing is modeled as a piecewise function depending on the position of glass. When glass is at the bottom, friction has a relative low value. When glass goes shortly into sealing of top frame, friction has a higher value. The direction of friction force is determined by velocity of glass. To avoid numerical errors in simulation, a positive speed threshold is set, which has a value smaller than $1.0e-03\,\mathrm{m/s}$. When glass speed is greater than positive threshold, direction is negative. When smaller than negative threshold, then direction is positive. Between positive and negative threshold, direction changes linearly depending on the ratio of glass speed and threshold.

The modeling of friction between glass and top frame sealing is a little different. When glass approaches top frame sealing and goes into it, the contacting length between them increases gradually from zero to max in a short time. It depends on the angle between glass moving direction and sealing. Usually the intrusion of glass into top sealing is between 20 mm and 40 mm. The further glass goes into top sealing,

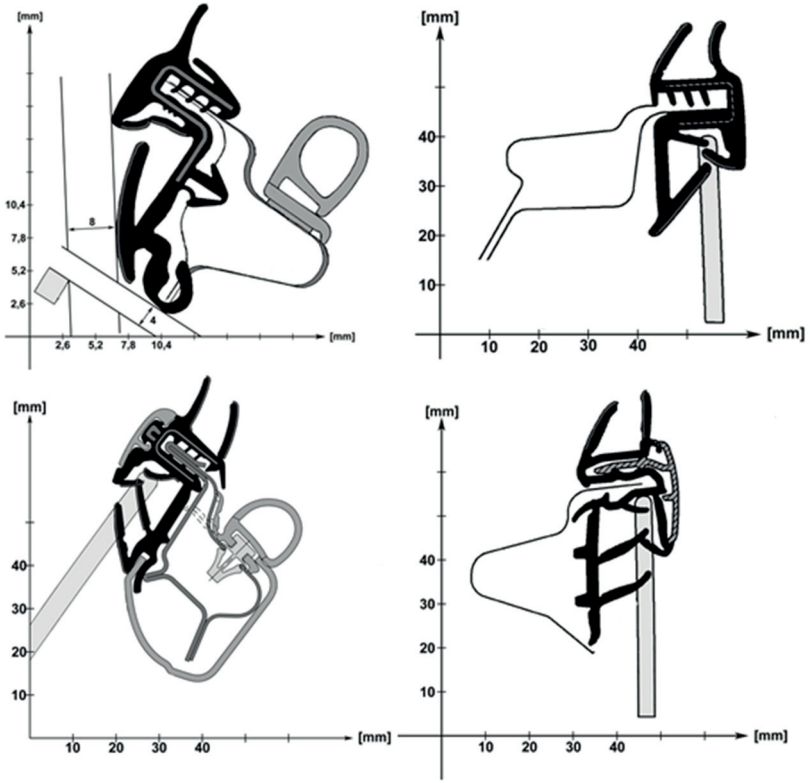

Figure 4.70: Sealings of top frame

the more friction there is, because glass edge presses on more rubber branches inside sealing, as shown in Fig. 4.70. During this process, it deals with another property of sealing, that is, the stiffness of sealing. Each branch in each form in sealings has its stiffness. As glass goes into sealing, it deforms branches. At first, the outer one is deformed and then the inner one. Glass encounters more and more resistance in form of increasing sealing stiffness until glass is stopped by the hardest component, metal frame of door.

To model such phenomena, the sealing intrusion is virtually divided into three ranges. In the first rang, friction and sealing stiffness are

small. In the next two ranges, friction and sealing stiffness increase. To stop glass, door frame is represented by a spring with stiffness at mega order. The possibility is left to end users of simulations to specify the length, friction and stiffness of each range, according to different designs, as in Fig. 4.70. The stiffness can also be identified through tests. In the test, the glass is driven by WR towards sealing with an electrical drive. The electrical drive is more powerful than nominal one, so as to reach longer linear range in measurement result. During measurement, torque and rotation angle of cable drum are monitored, as in Fig. 4.71. With known radius of cable drum, torque and angle can later converted into force and displacement. It can then be used to calculate stiffness. In the Fig. 4.71, the change of slope, marked with number 1, 2 and 3, indicates the increase of stiffness, as glass moves into top sealing.

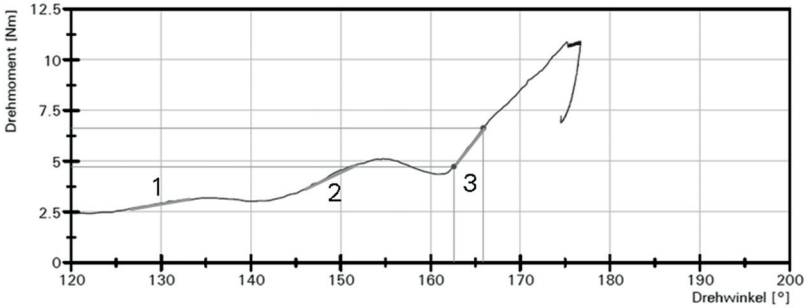

Figure 4.71: Measurement of sealing stiffness
x-axis: Angle; y-axis: Torque

4.3.1.2 Glass mass and tilting angle

As discussed in modeling sealing friction, the geometry of door frame is not taken into account. So it is the same with glass. Despite of it, mass of glass is taken into account of modeling. In the realization of door model, glass is represented by a mass model. Its parameter can be identified by weighting glass. Another modeled feature is the angle between glass movement direction and vertical direction. Within the

same door, it is also the inclination for rail and A(B or C) pillar. The usage of this angle in modeling is to calculate the vertical projection of force from glass to rail sliders. In the extreme case, it provides designers information how much force sliders have to sustain. Normally this information is provided by car manufacturers. In case of unavailability, angle measurement can be conducted.

4.3.2 Drive speed measurement system

The real time measurement of electrical drive speed provides WR electronic controlling devices an eye on the position of glass. There are currently two main methods to measuring drive speed. One is based on ripple current[98] and the other one is Hall sensor[99, 100]. Most mechanical commutation dc motors are capable to produce ripple current. By counting the number of ripple peaks in certain time, ECU(Electronic Controlling Unit) can calculate the angular displacement of armature and also the rotational speed. Applications with Hall sensor are widely used in WR systems of Brose. Therefore, speed measurement system with Hall sensor is discussed in this section.

The measurement system consists of a four-pole ring magnet, attached on armature, and a Hall sensor. The working mechanism is, as the rotation of ring magnet along with armature, Hall sensor senses the change of magnet field and as a result its output voltage changes at the same time, shown in Fig. 4.72. If ring magnet turns one revolution, output of Hall sensor changes four times and gives two pulses. By counting either the number of changes or the number of pulses, angle and speed can be attained. If two Hall sensor are aligned next to each other with a small gap to ring magnet, there will be a phase shift between their outputs, when armature is rotating. Such phase shift indicates the direction of rotation. In reality, two Hall sensors are packed in one micro chip and the analog output of sensors is firstly processed by the conditioning circuit on the chip and then digitalized. Depending on the size of register, electronic position of glass increases or decreases as Hall signal changes. An example of voltage output of Hall sensor and electronic position is

shown in Fig. 4.73. The disturbance in Hall signal can be cause by brush commutating, electrical components in bruch holder and magnet alternating in armature widing.

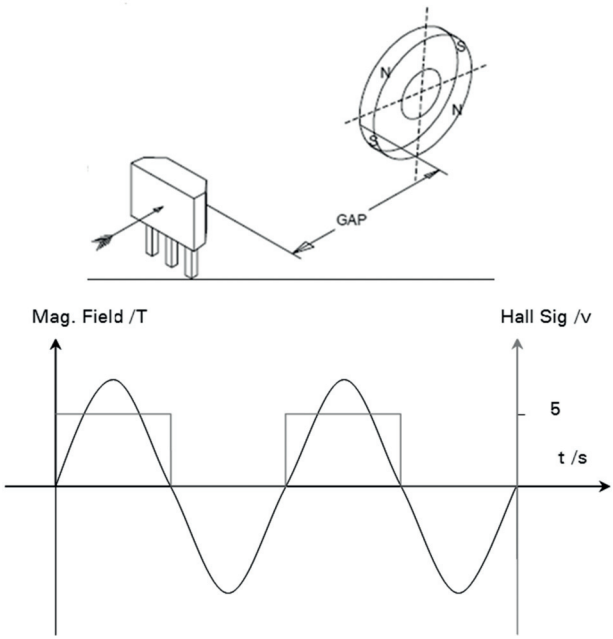

Figure 4.72: Ring magnet and Hall sensor

Modeling Hall sensor on chip level is not the task of this work. To describe the changing of magnet field to obtain the alternating Hall signal is technically possible with VHDL but too costly. The strength of VHDL here is to describe the correct behavior. In real system, the input to Hall sensor is the change of field, the reason of changing magnet field is the rotation of ring magnet attached the rotating armature. Therefore, in model of Hall sensor, the input is directly the angular displacement of armature. No matter whether the real output of Hall sensor is analogy or digital signal, it will be in the end digitalized. For this reason, the output of Hall model is digital signal, “0” or “1”. The parameter of Hall sensor model is the distribution ratio of poles on ring

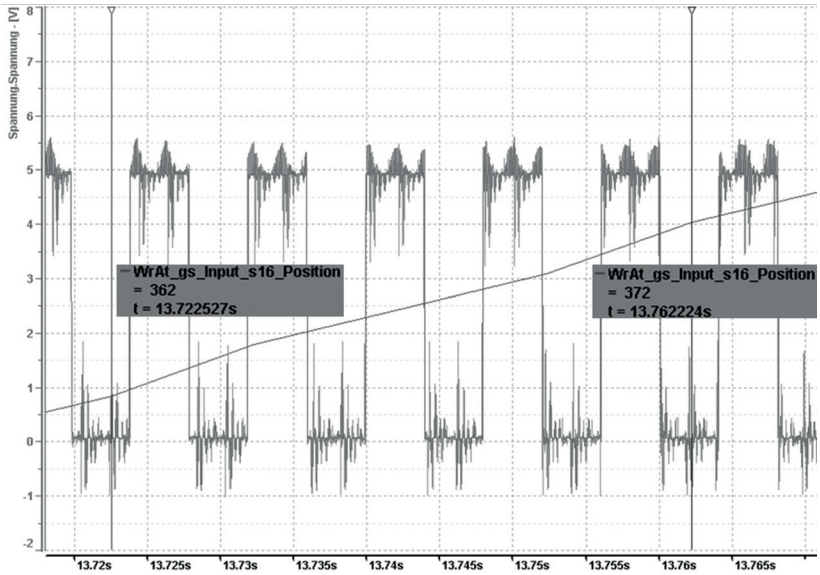

Figure 4.73: Measurement of Hall signal
x-axis: Time; y-axis: Voltage of Hall signal

magnet. The poles are required to be as equally as possible distributed, so as to achieved a duty ratio of Hall signal close to 0.5. So, the uniformed distribution ratio of each pole on a four-pole ring magnet is close to 0.25. The more exact ratio can be obtained in the test report from suppliers. The form of parameter is a sequence of four numbers, which have little deviation from 0.25. The correct realization of Hall sensor behavior is to alter Hall output at the time when the rotation angle crosses the boundary of one pole. It must be reliable when armature rotates in each directions and also when armature changes its direction. To accomplish the requirements, two dynamic thresholds are implemented. One is the real time threshold to limit the max value and the other one is for the min value.

The initial angle of armature is always zero. The two threshold are set with a product of 2π and the values of the first and the fourth numbers in parameter sequence. At this moment, armature has two possibility

of rotation direction. Once armature turns and later crosses one of the angle threshold, it means, in real system, that one pole is passed. The actions are, output of Hall sensor alters, and, the values of thresholds adjusts automatically depending on the crossed threshold. Actually, the values of threshold are shifted, meaning, in the case that top threshold is crossed, the bottom threshold takes value of the top and the value of the top is calculated based on the 2nd number in parameter sequence and assigned. In the case of the other rotational direction, shifting takes place reversed. This way of realizing Hall sensor is simulated and shown in Fig. 4.74. In the system with two Hall sensors, information of rotation direction is also output. In modeling, rotation direction is simply a differentiation of armature angle.

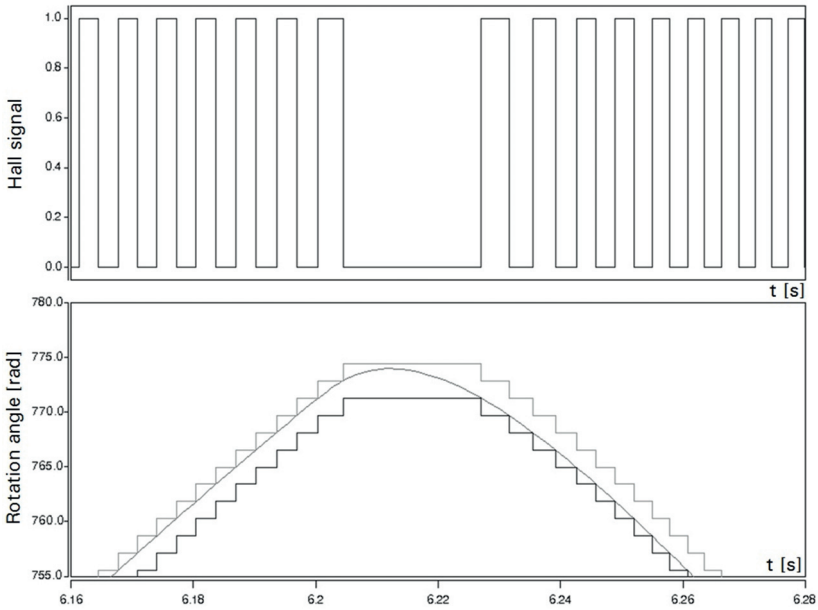

Figure 4.74: Rotation angle, dynamic threshold and Hall signal

4.3.3 Electronic system and electrical switch

4.3.3.1 Hardware, software and algorithms

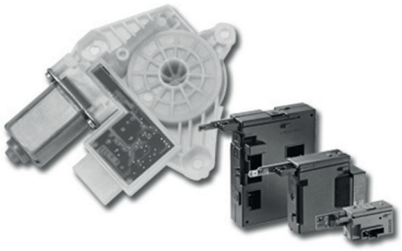

Figure 4.75: Window regulator electronics

Electronics of WR systems can be quite different from each other. As the complexity of controlling increases, size of electronics increases, because more components are required. The simplest controlling electronics may deal with only instructing glass to go upwards or downwards with a relay. And, if electronics has anti–trap function, then there must be a Electronic Control Unit (ECU), power regulation circuit and other necessary components. If electronics is integrated with controlling functions of other devices in door, even more components are involved and the size of the whole pack is obviously bigger, as shown in Fig. 4.75. The fact is that, different car manufacturers have their own requirements and function specification of WR electronics and, depending on cars and target market, number of available functions in electronics are also varying. It is possible but very time- and effort costy to model all kinds of electronics. Therefore, a general purpose electronics is modeled in this work. This electronics is the basis of all other complicated controlling systems. It involves the basic glass controlling functions and also anti-pinch functions.

A general purpose electronics of WR have generally three components, hardware, software and anti-trap algorithms. Hardware is carrier of software and anti-trap algorithms is one module of software. Hardware is the interface of power supply, normally 13 V, and motor power. If

switch signal changes, electronics firstly analyzes it and than execute through relies. Hall signal and direction from motor are always input to hardware, so that electronics can observe the state of motor and glass all the time. The interface of hardware is shown in Fig. 4.76.

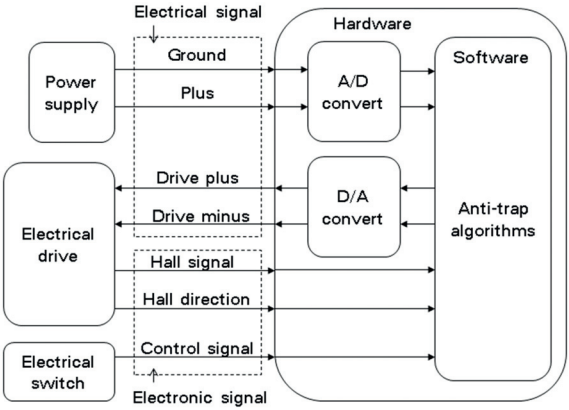

Figure 4.76: Interface among hardware, software and algorithms

In reality, electronic hardware prepares signals for software as specified. The actual carrier of software in hardware is ECU. As an electronic component, ECU inputs and outputs only electronic signals. Therefore, power suppler and Hall signal are all digitalized by it. The controlling signal to motor is sent from software to a driving circuit, which then changes the state of relay. As a result, electrical motor moves glass in desired direction. The driving circuit is actual a electronic switch, on one side it interfaces ECU and on the other side it interfaces relay. In Fig. 4.76, it is marked as D/A converting circuit. Software has normally many modules and each module has a specific function. Anti-trap algorithms is one of the most important module. To secure the know-how, this part of software code is not directly implemented in simulation but as a dynamic linked library(DLL). The model of software in simulation provides an interface with this DLL. DLL receives real-time information of power supply, Hall signal, direction and switch signal and determines whether pinching event happens and makes decision whether

motor should be reversed or not. As it deals with Know-How of Brose, the detailed content in each single models can be not revealed. But, with the interfaces and signal flows, people could get a basic idea of the mechanism of WR electronic system.

4.3.3.2 Electrical switch

Electrical switch is the device which people touch directly to control an electrical power WR. Depending on the design of WR system and the functionality of its electronic systems, switch varies. Basically, window can be opened or closed by constantly pressing on buttons of switch. With comfort function in electronics, one press on switch will automatically lift up or down glass. According to project requirements, there are combinations of these electronic functions.

In simulation, model of switch has the meaning to send different combinations of instruction, so that WR system runs in various working cases. In this manner, users of WR simulations can reproduce different operation situations and hence observe the behavior of system. Therefore, model of switch provides the possibility to create a sequence of instruction, which are sent into electronics. In this sequence, it does not make any difference between non-automatic and automatic operations.The instruction 0 is to stop, 1 is to go up and 2 is to go down. There are two types of controlling sequence defined in model, one is time dependent and the other is position and voltage dependent. Both sequences are made of controlling units. The unit of time dependent sequence consists of two real number, the first number marks time to begin operation and the second number marks the operation. For example, $(0.1, 1)$ indicates that instruction is set at time point 0.1 s to drive glass go upwards. A sequence, like $(0, 0), (0.1, 1), (4.5, 0)$, means WR does nothing at $0s$, begins to move up since 0.1 s and then stops at 4.5 s. The controlling unit of position and time dependent sequence are made of four elements. They are in sequence target position, voltage offset, reserved element and timeout register. Under the setting that battery voltage is 13 v and initial position of glass is 0, a unit,

like $0.500, 0, 0, 0.6$, gives instruction to drive glass to go up to 500 mm with 13 v and, if glass position stops changing for $0.6s$, the current instruction is cancelled and the next instruction unit will be executed. For instant, the sequence of $(0.500, 0, 0, 0.6), (0.100, 2, 0, 0.1)$ is to lift glass up with 13 v and then pull down glass with 15 v after the first instruction becomes invalid.

4.3.4 Anti-pinch force measurement system

Figure 4.77: Anti-pinch force measurement gauge and springs stiffness (from left to right): 5 N/ mm, 10 N/ mm, 20 N/ mm and 65 N/ mm

In short, anti-pinch force measurement system is called anti-pinch gauge. It is designed to imitate obstacle during pinch events and also to measure the pinch force. The European laws require that the pinch force has to be measured by instrument or test rod with a stiffness of 10 N/ mm. In America, the required stiffness is 20 N/ mm, when test rod is 25 mm or larger in diameter, or 65 N/ mm, when test rod is smaller than 25 mm in diameter. Car manufacturers may make the request that pinch force is measured by all these spring rate or one of them. In Fig 4.77 is a force measurement gauge. In test, it is hanged on the edge of glass and moves upwards along. When its rod touches door frame, a pinch event is simulated and pinch force is measured. Pinch force is required to be below 100 N, which is written in regulations.

The model of anti-pinch gauge has three pins. One pin is to connect with glass, so as to obtain the position of glass. Another pin connects to sealing. The third pin, which does not have physical meaning, sends out the amplitude of pinching force. Between pins of glass and sealing, behavior of a spring is implemented. Therefore, one of the parameters of the model is stiffness of measuring gauge. Another important parameter for this model is the position, where pinch event takes place when glass is rising. As mentioned before, the top contour of glass is curved. When force gauge hangs on glass and moves along, pinch force may not be on the same direction as the moving direction of glass. For this reason, a parameter, named "pinch angle", is implemented. The identification of this parameter can be achieved by measuring in CAD models.

Chapter 5

Integration of components in window regulator system and applications of simulations

5.1 Models of generic rail guided cable window regulator system

The component models, which are built up in the last chapter, are interconnected with each other so as to form the simulation model (bench model) of WR systems. For each component model, a graphic symbol is also created. The shape of the symbols is like its modeling object and has defined pins for interconnection. The bench model of WR system are a result of interconnection of component models. Figure 5.1 is an example of double rail WR.

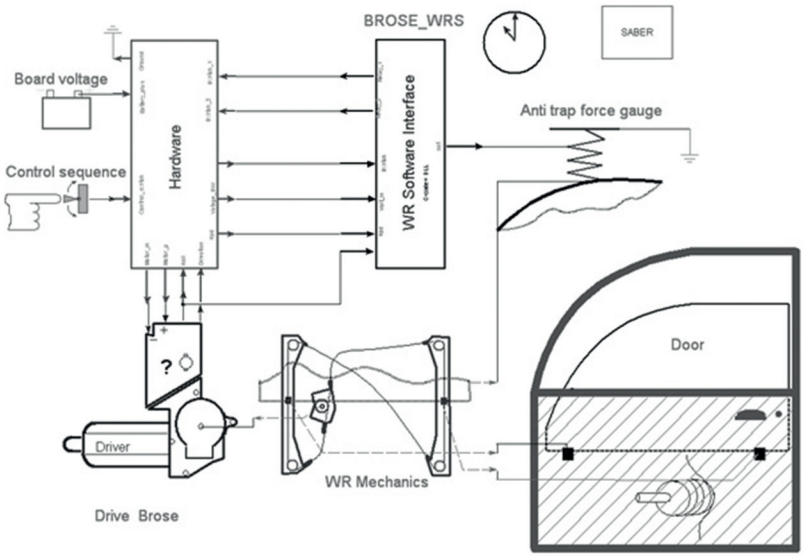

Figure 5.1: Model of rail guided cable driven window regulator system

In the bench model, the gear of drive is connected to cable drum of mechanism. Other pins of drive model are electrical and electronic ones. The electrical pins are voltage plus and minus. The electronic pins are Hall signal and rotational direction from Hall sensor.

Hall sensor is modeled as an individual component in last chapter, because it is an important component and serves as "eyes" of electronic controlling system. In realizing model of WR systems, model of Hall sensor is packed in drive model, since the information of the armature rotation is from model of drive. In reality, Hall sensor has separate voltage supply lines, as the voltage is lower than electrical drive voltage and current is also very little. In modeling, these two voltage supply lines are omitted, because the focus of Hall sensor is the behavior of angle change detection.

Electrical drive can be seen as a component, which joins electrical components and mechanical components together.

a)On the electrical side

The core component is electronic hardware. As shown in Fig.. 5.1, model of hardware interfaces control sequence, software, drive and battery. The reason why model of battery is not discussed in component modeling is that it is relatively a simple model, consisting of only an ideal voltage source and a resistance. The arrows around hardware model indicate the signals flows. Voltage is supplied to hardware and later to drive. Each command in control sequence is passed into hardware and then through hardware to software. Amplitude of voltage is digitalized into register and then passed to software. So are the signal of Hall and direction. Hardware informs software of time with a register. When the size of resister and the oscillation frequency of hardware are determined, the maximal time, which the register can represent, is fixed. The value of this register is also sent to software. With all these information, software analyzes the state of system operation and decides the command to be executed in the next step. It is realized by sending hardware two software signals. They control two relays. The combinations of the two controlling signals lead to motor driving glass upwards, downwards or stop.

b)On the mechanical side

Gear of drive connects to drum of mechanism. In reality, mechanism interfaces glass with one or two sliders, depending on number of rails and applications. In model, the number of pins between mechanism and glass is unified to be one, so that one bench model suffices for both models of single and double rail WRs. For this purpose, a model of lever is placed between the two sliders in double rail WR. The position of slider is the same as the bottom position of glass. As the glass geometry is not considered, the top edge of glass has then the same position of its bottom. Therefore, the pin of glass is placed at the top edge of glass in model of door. The second pin of door is sealing, which simulates the hard stop of glass. Between glass and sealing, mode of anti–trap gauge is placed. The quantity of force is sent to software, where all necessary information are collected and written in files for

analysis. This function does not exist in real software module, but we make use of the power of programming to help in saving necessary simulation results.

In the Fig. 5.1, there are another two components, used to observe simulation processes. They are not related to mechatronic modeling of WR. Therefore, they are not at focus.

The advantage of uniformed interconnections among component models is reusability. The number of pins and their definition are essential to functionality of WRs. Different WRs can be simulated with the same bench model. For example, a single rail WR model can replace the double here and simulate, without editing any pins. It saves the effort of maintenance. A graphic illustration is straightforward and easy for end users to understand the simulation contents. When users work often with the same simulation of WRs, maintenance of symbols can be further saved.

Model of WR is in one way demonstrated here in graphic symbols. In another way, the bench model is coded in VHDL language and saved in textual file. The file of bench model is seen as a structural container, which will not be modified so often. The different variants of each single component models shares the same model name and layout of pins, but has its own application name and its characteristics, which can be in form of a parameter set or a different realization of component model. For example, the realization of drive is the same and the drive from different suppliers have only different parameters. In contrary, the realizations of mechanism and software are different from each other, which can be not described by parameters. Despite of differences, models are all saved in files. In this way, a library is built up in tree structure to organize simulation models and resources.

5.2 Simulation environment: BroSAnT

The practical output of this work is a complete set of WR models, which will be used in simulation environment, Brose Simulation Analysis Tool (BroSAnT), shown in Fig.. 5.2. BroSAnT[101, 102, 103] is an implementation of system simulation in house at Brose. It simulates complete WR systems.

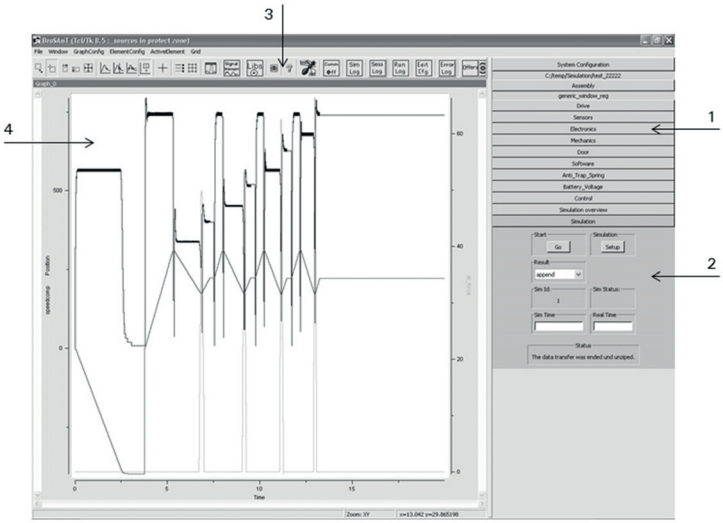

Figure 5.2: Brose Simulation Analysis Tool (BroSAnT)
1. Simulation configuration 2. Simulation control and statues
3. Result analysis tools 4. Result viewer

The goal of BroSAnT is to provide engineers from different development functions a view of system behaviors, even if engineers do not have any deep knowledge of simulation technology. BroSAnT utilizes the famous IT solution, server and client. Server in this case is responsible for mainly holding simulation source (models and library structure) and carrying out simulation computation. The client, shown in Fig. 5.2, is a graphic user interface, to configure simulation, receive simulation result and represent the result with basic analysis functions. The advantage of

centralized maintenance that the Know-Hows, which is saved in models, are secured. And the effort of maintenance relevantly low, compared to distributed solution. In another aspect, the cost of simulation software is low, because one or two licenses installed on server are sufficient to cope with the simulation request. The extendability of BroSAnT is also high. New simulations can be standardized and included in simulation library, so as for a further and wide usage. At the moment, the focus of simulation types are the following two.

5.2.1 Types of simulations

The fist type of simulation is drive characteristic lines. Drive characteristic lines are the basic information to evaluate the mechatronic performance of electrical drive. In modeling drive in chapter 4, they have been shown with an example of Bosch 12Nm drive, like in Fig. 4.45. From the curves, one can see the linearity of drive. With known load to drive, working point can be found. Working point is the essential criterion, to select a proper power class of motor to be used in WRs. Therefore, it is of meanings to carry out such simulations.

The second type of simulation is called generic window regulator. This type of simulation builds up virtually a complete WR system, as stated in section 1 of this chapter. Graphically, the components involved in this type of simulations are shown in Fig. 5.1. In environment of BroSAnT, selecting this type of simulation, users should configure WR system by choosing components from each sub library, for example, type of mechanism, software and so on.

By default, one simulation consists always of two processes. One process is electronic normalization and the other process is user defined sequence. With the normalization process, electronics in WR can determine the starting position of glass. For electronics, the position of glass is zero, when door window is completely closed.To normalize electronics, glass is driven with nominal voltage, 13 V, to go upwards from the state of being fully open. During this process, position counter

counts in the negative direction, from zero to negative values. After glass is stalled in the top frame for more than 500 ms, electronics sets the position counter to zero and normalization is completed. Afterwards, as glass goes downwards, electronic position counter increases its values, until glass is stalled again at the bottom. The change of position counter and physical position are opposite to each other, shown in Fig.. 5.3.

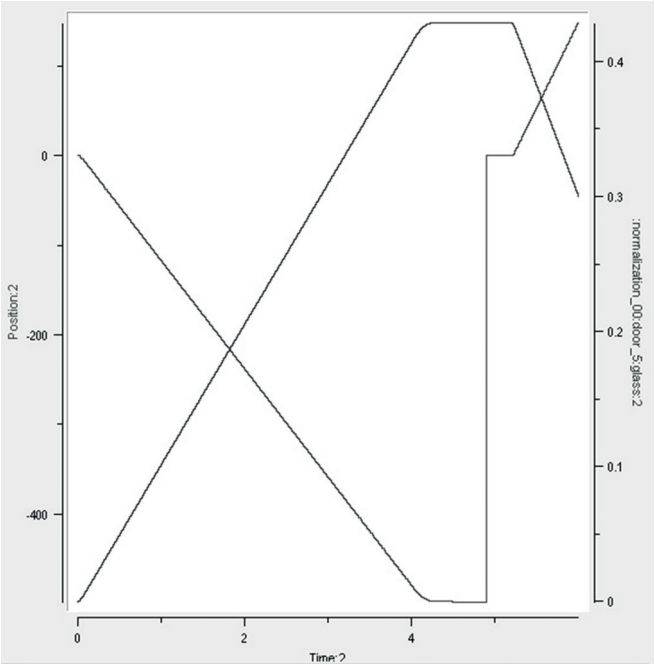

Figure 5.3: Electronic normalization process
x-axis: Time; y-axis: Electronic position (red), glass position (green)

After normalization, WR runs according to the controlling sequence defined in model of controlling switch. Without modification, switch instructs WR to go upwards under varied voltage, for instant, 9 V, 11 V, 13 V and 16 V, to test anti–pinch function. Fig. 5.4 shows the changes of several important signals during a pinch event of WR system. In the Fig., it is seen that pinch event happened at position of about

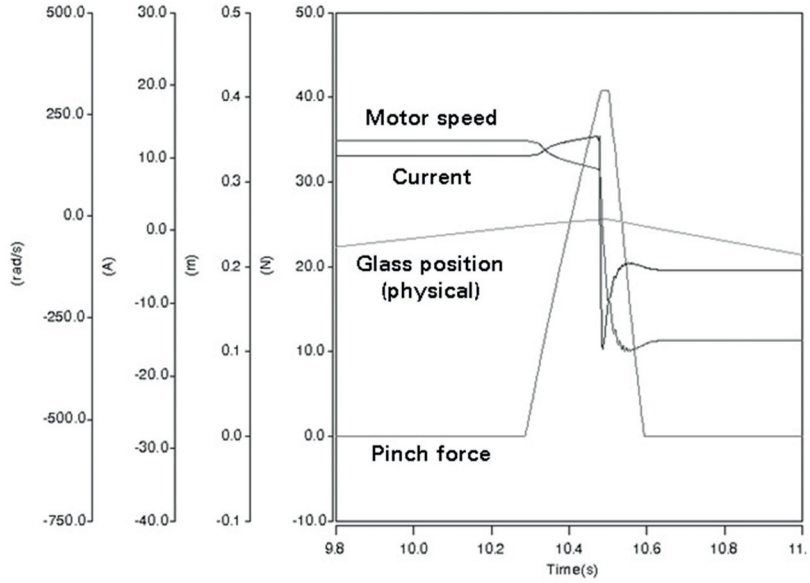

Figure 5.4: User defined simulation sequence: Anti–pinch process x-axis: Time; y-axis: Motor speed, current, glass position and pinch force

250 mm away from the bottom. After glass touched obstacle, motor speed began to decrease and motor current increased. Meanwhile, pinch force, measured by force gauge, began to increase. As the pinch went further, motor speed decreased further and then it crossed threshold. As a result, electronic controlling system sent instruction to motor to reverse. After the reversing instruction was sent, pinch force increased still a little because of inertia. It then decreased, since the motor began to reverse.

In simulating anti–pinch function, users have the possibility to set voltage, pinch position, spring stiffness, software parameters and so on. It can also be set by users that only the normal runs of WR under different voltage. To achieve it, pinch position is to be set higher than top frame. The simulation of generic WR provides chances to observe system behavior under various working cases.

5.3 Applications of simulation

The quality of simulations depends on the quality of parameters. The more accurate the parameters are, the better quality one can obtain from simulation. We provide models and tools of simulations to users. Users are at the position to find reliable input information for simulation, such as parameters and measurements, so as to make the best use of the power of simulation.

From another side, applications can be very different from cases to cases, depending on purposes and issues during development. Here, several examples are presented.

5.3.1 Selection of electrical drive

Simulation is helpful tool to aid the development of WR systems. One of its applications is to select appropriate electrical drive to be set in WR. An appropriate drive means that it should have enough power to fulfill the basic function to lift up and down window glass. The lifting period for a normal passenger car should be between 3.5 s and 4.5 s. For WRs in truck, lift period is longer because of longer stroke. It is obvious that drives with more electrical power can always achieve. However, they are more expensive and sometimes heavier. When magnet stays the same, more power means more windings and as a result heavier and more material cost. Stronger magnet, for example of rare earth magnet, is certainly more expensive, in comparison with ferrite magnet. From economic point of view, proper electrical drive is beneficial for both system suppliers and car manufacturers. Electrical drives are usually developed and produced in a discrete sequence of power classes, for instant, 8.5 Nm, 10 Nm, 12 Nm and 13.75 Nm. Therefore, more specifically, simulation helps in picking up proper power class of electrical drive for WR application.

Out of experiences, working point of electrical drive in WR should not be higher than 40% of its maximal output torque at room temperature, to ensure that window closing can be fulfilled at all temperature

condition, from $-40°C$ to $80°C$. At $80°C$, speed–torque curve of drive becomes steeper, no–load speed increases for about 20% to 30% and maximal torque decreases for about 30%. Load to drive decreases, because friction between door frame and glass becomes less. At $-40°C$, speed-torque curve becomes flat, shown in Fig. 5.5. Meanwhile, sealing friction increases greatly, as rubber turns harder. Efficiency of WR mechanics becomes less, since bowden friction increases at low temperature. As a result, working point of electrical drive shifts to right in Fig. 5.5. In this case, drive speed is much lower than the speed at room temperature. As a result, there is risk that closing window may not be fulfilled. To make sure that working point is lower than 40%, it is then important to estimate load to drive, which is the friction from sealing and mechanism during lifting.

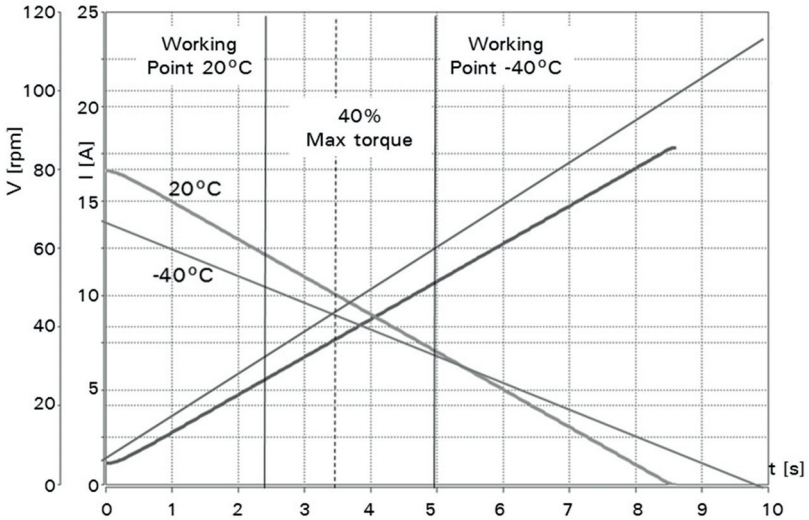

Figure 5.5: Working point of electrical drive
x-axis: Torque; y-axis: Velocity and current

Fig. 5.6 is the measurement of sealing friction force. The force sensor was attached to lower edge of glass, where glass is clipped into slider of WR, and measured force during glass was lifted, with electrical drive

detached and mechanism moving along. The three-time measurement shows that two measurement coincide each other well. The measurement, which has lower force, is resulted from the rotation of glass during lifting. With such measurement, friction force between glass and sealing can be estimated by subtracting gravity of glass and loss in mechanism. In the shown case, glass mass is around 2.55 kg, so gravity is about 25 N. Loss in mechanism is constant and friction of slider on rail is the major component for it. Here, the slider friction is about 15 N and complete frictional loss in mechanism is about 20 N. Then, sealing friction at bottom is about 15 N and at top it is about 40 N. The force sensor used in this measurement has a tolerance of ± 10 N.

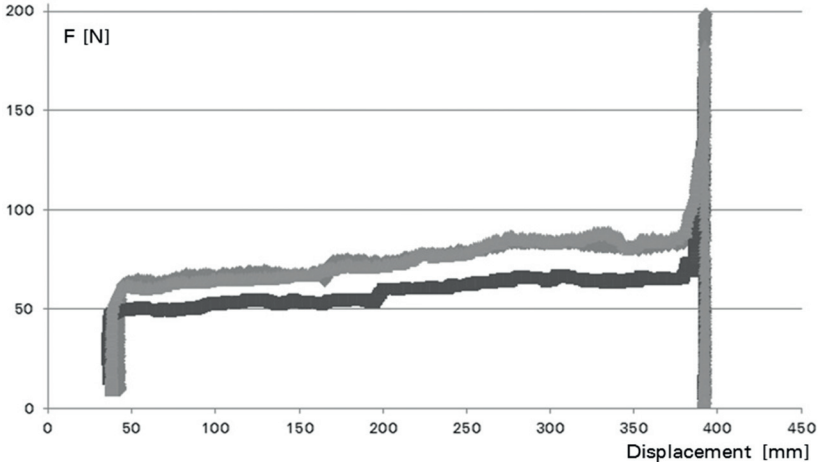

Figure 5.6: Load from door
x-axis: Glass position; y-axis: Force to lift glass

To increase credit, driving torque at cable drum is measured, shown in Fig.. 5.7. The measurement is prepared in the manner that electrical drive is replaced by torque handle. The handle was rotated by hand to lift up WR. During lifting, sensors in handle recorded angle and torque. The result is more trustable, because it is more close to the working situation of WR and electrical drive. Furthermore, the resolution of torque is $1m$ Nm. In Fig. 5.7, it is seen that torque at bottom is

around 1.4 Nm and torque at top is around 2.5 Nm at room temperature. 2.5 Nm is taken as driving load for selection of electrical drive. The torque from this measurement can be converted into force with cable drum diameter. In this case, diameter is 44 mm. With the same method above, sealing friction can be estimated, at bottom it is about 15 N and at top about 65 N.

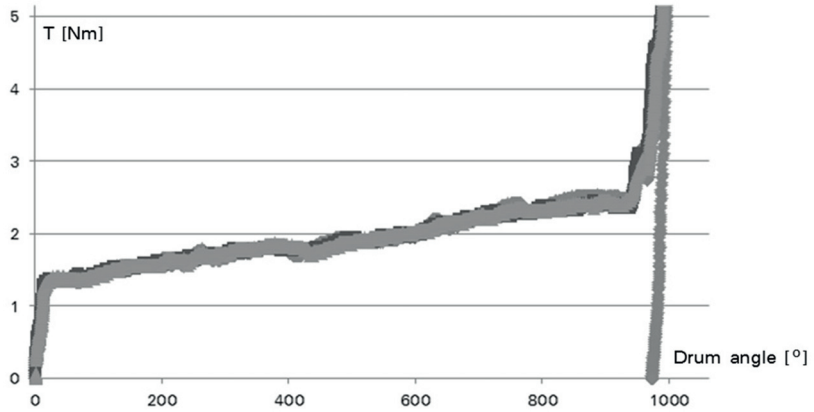

Figure 5.7: Driving torque during lifting
x-axis: Angle of cable drum; y-axis: Torque

An electrical drive with 8.5 Nm maximal torque is appropriate for the WR in the measurement above. The 40% boundary of this drive is 3.4 Nm, which is around 1 Nm away from 2.5 Nm. However, the worst case has to be considered. Electrical drive has a wide tolerance band. Its maximal torque at room temperature can be 15% different from the nominal value, then maximal torque can have a low value of 7.2 Nm. 40% of the low value is around 2.9 Nm, which is still safe to be used. The wide tolerance band is a result of production process, which has often a normal distribution. Under this distribution, the number of motors, which is close to the low value of torque, is limited.

Above, a complete procedure of selecting drive with consideration of load is presented. With reliable information of friction losses in door

and mechanism, power class of drive can be accurately chosen. Friction force, as shown above, can be obtained from measurements, which is the most direct method. In real development and applications of WRs, engineers are mostly customer oriented and they have already imagination about the range of friction losses for carry-over design or design with few changes. Measurement can be saved for these cases. Measurement is still necessary in case of complete new design. but it does not occur in a higher frequency. With simulations, lots of measurements can be saved and proper drive can also selected. Engineers, at the same time users of simulations, can create a WR in computer, config the friction in door, select desired WR mechanism, in which sliding friction and friction of bowden and pulley should be conFig.d, and then test drive with different power classes. A proper drive can be chosen with consideration of this 40% boundary and also other conditions.

If electrical drive is built into WR system, there are not so many good possibility to measure friction forces and driving torque. However, one can measure current and rotational speed of drive during stroke through electronic system as an indirect way to check the performance of drive. With measured working current and speed, working value of drive load can be determined through drive characteristic lines. With the method mentioned above in this section, an electrical drive with nominal torque 8.5 Nm is selected to be mounted in the WR system, the door friction force and driving torque of which were measured and shown above. The simulation model of this drive family can be created with the method stated in section 4.1. For a single drive, its characteristic lines can be measured and its parameter set can be calculated and then created for single application.

With selected drivel, the real WR system is built up. Measurement of drive current and rotational speed was carried out during lifting glass from being completely open to being completely closed. The result is shown in Fig. 5.8. The same process is simulated and the result is presented in Fig. 5.9.

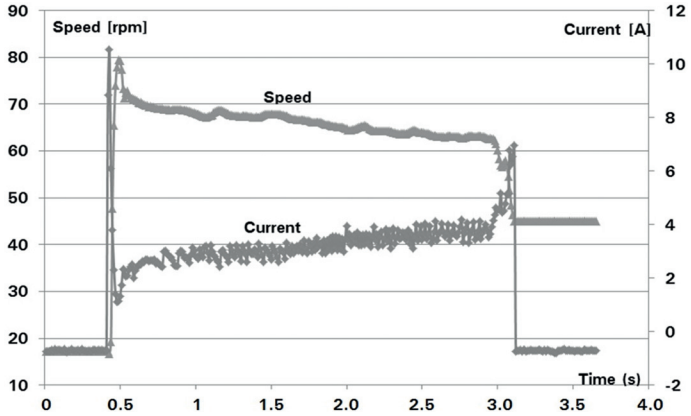

Figure 5.8: Measurement of drive current and speed during lifting x-axis:Time; y-axis: Rotational speed and motor current

The measurement on system shows that the drive speed and current are each about 72 rpm and 2.5 A, when glass is at bottom, while speed and current are each about 63 rpm and 4 A, when glass was about to go into sealing. The simulation shows little differences in speed and current in comparison with real measurement. Meanwhile, simulation supplied information of torque course during lifting, which is also comparable to the measurement in Fig. 5.7. Such comparison provides an examination to the capability of using simulation as an supporting tool in choosing power class of electrical drive in development of WR systems.

In practices of simulations, information regarding components are stored in library. These information are either from measurements or from experiences. Components are also separated into two catalogs, one is standardized components, for example a family of drive, the other is single component for special case, for example a particular drive. At early phase of development, users build up simulation with existing components. The possibility is provided for them to modify parameters so as to reach the reasonable states in simulation, since users are mostly customer oriented. As the development of WR goes further, more information regarding system design are available, for example

of prototype or series product. Parameters can then be improved so that component and system behavior are closed to reality. And such improvement is then a basis for the future applications of simulations and developments. In this sense, library of simulation components is "living". It grows as being used in practices and becomes more robust as more applications.

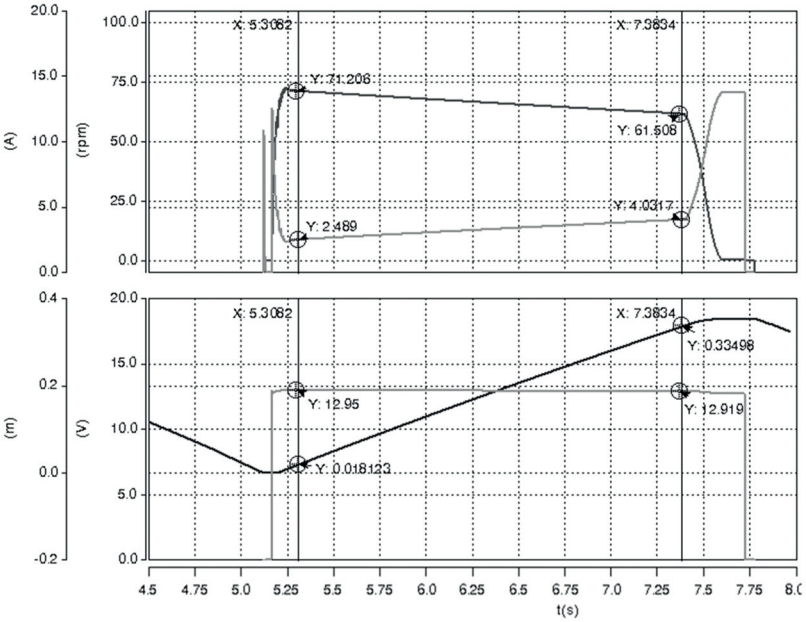

Figure 5.9: Simulation of drive current and speed of stroke

5.3.2 Examination of anti–pinch function in early phase

While electrical drive fulfills that working torque should be lower than 40% of its maximal torque, it has still the rest 60% torque, which is used to close window glass firmly. For example of a 12 Nm drive in WR with 40 mm drum diameter, closing force of glass is $(12 \times 60\%)/0.02 = 400$ N. Such force is enough to injure severely body of an adult or get a child

killed, when there is no anti–pinch function available in power WR system. Therefore, it is important to have anti–pinch function correctly developed and checked in an early phase and later its robustness examined. Simulation models developed in this work provide aids in this aspect.

The trust of simulation increases, when simulation result is compared to measurement, the differences are in accepted range and the differences have reasonable explanations. To improve the credit of simulating anti-pinch function, pinch forces under driving voltage of 9 V, 13 V and 16 V are compared between real measurements and simulations. The WR system is the same as the one in the last section. So, simulation models are well parametrized. The pinch forces in system are measured at the position of 40 mm below the lower edge of top door frame. The pinch position is in the middle of the two pillars. The physical measurements have to be performed separately, because driving voltage has to be adjusted every time after one measurement. The measurement result of pinch force in real system is shown in Fig. 5.10.

With parametrized models, anti-pinch function can be tested under different voltage in one simulation, which is realized through configurating control sequence. As shown in Fig.. 5.11, WR went through firstly normalization process and then into process of three anti-pinch events under designated voltage sequence. The forces of simulation are each 54.4 N, 58.7 N and 61.6 N. If the resolution of force measuring gauge, about 0.5 N, is considered, results of simulation are close to real measurement. The more such kind of comparison is conducted, the more trust users can put on simulations. The precondition of comparison is the availability and quality of information to parametrize models, such as electrical drive, mechanism, door and so on.

For particular investigation of system behavior, effort can be spent on searching for accurate parameters for simulations. For general purpose, simulation of anti-pinch function serves as a tool for engineers to foresee the functionality of anti-pinch functions. During the concept phase, in-

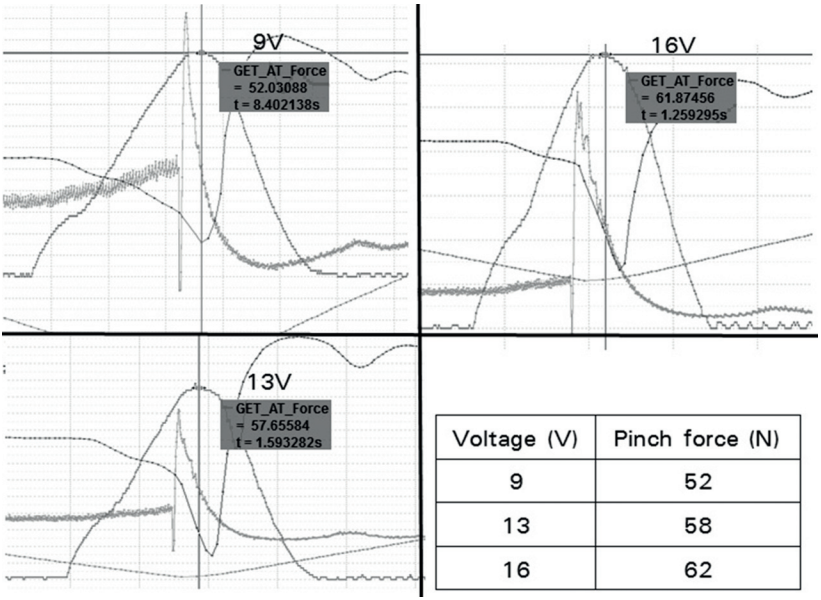

Voltage (V)	Pinch force (N)
9	52
13	58
16	62

Figure 5.10: Measurement of pinch force under 9 V, 13 V and 16 V

formation regarding customer door is limited, design of WR mechanism is on sketch and selection of electrical drive is ongoing. However, engineers want to know amplitude of pinch force, so as to optimize design easily. Simulation fills the gap. As the development goes further and further, more information is available and more robust simulation can be built.

5.3.3 Investigation of design parameters

Simulation of WR system can be used to investigate the influence of design parameters, to see what kind of outcome each parameter can bring to system and how much. Simulation can bring result in short time and the cost is low, in comparison with prototype. Here, an example is demonstrated with cable drum. Cable drum is the component to convert rotational movement and torque into translational movement and force. The conversion ratio is its diameter, which has influence on pinch force, shown in Fig.. 5.12. As diameter of drum decreases from

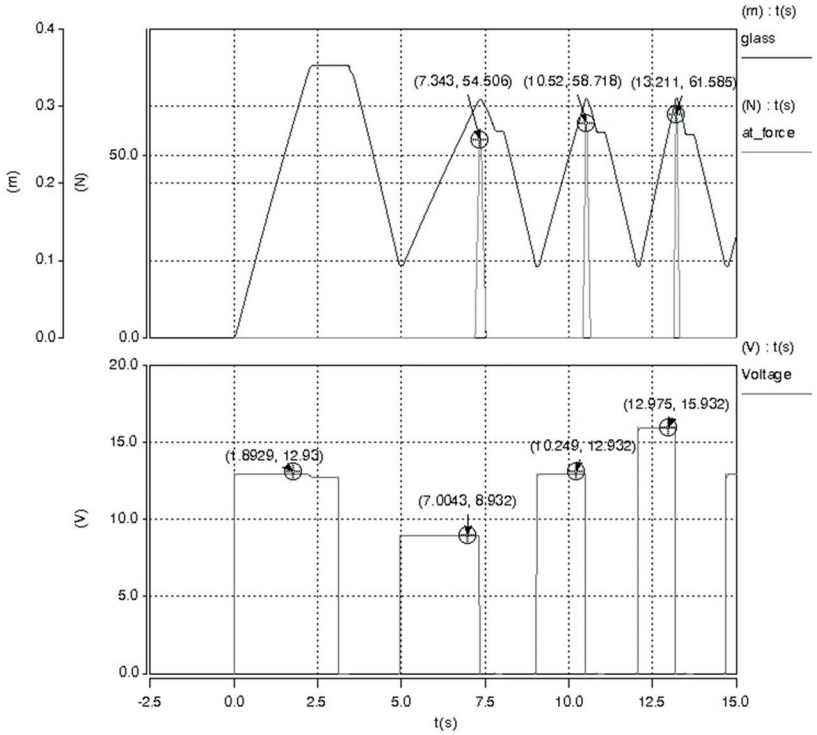

Figure 5.11: Simulation of anti-pinch event under 9 V, 13 V and 16 V

48 mm to 44 mm, pinch force increases. An simplified explanation is that increased drum diameter needs less pinch force to get enough additional torque, which produces speed drop in drive to trigger anti-pinch function. More accurately, it involves the calculation of force chain in WR mechanism.

From another side, car manufacturers have requirements to WR systems. One of them is the stroke time. Diameter of drum has influence on the feeling, whether glass is lifted up too slow or too fast. Engineers can make use of WR system to probe different drum diameter and select proper ones. Furthermore, drum diameter effects also its revolutions, under the fixed lifting stroke. The number of revolutions determines then the numbers of cable winding and the thickness of drum.

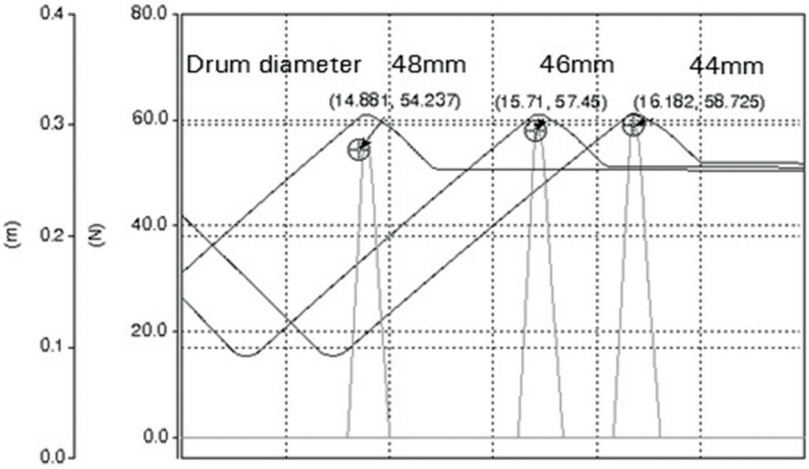

Figure 5.12: Simulations with drum diameter 44 mm, 46 mm, 48 mm

Table 5.1 shows stroke time and drum revolution simulated with several drum diameters. All the parameters can be investigated and its influence can be quantified, for example, inertia of motor armature, friction losses in mechanism and friction in door. The content of investigation can be different from each other, but principle is the same. Another application of simulation can be virtual tuning of software parameters and experimentation of new software functions, since parameter and function changing in computer environment are easy to execute. In summary, simulation of WR system or its components provides possibility for investigation and examination of system behavior.

Table 5.1: Influence of drum diameter

Drum diameter (mm)	Stroke time (s)	Drum revolutions
40	3.35	3.20
42	3.22	3.04
44	3.11	2.90
46	3.00	2.77
48	2.91	2.65

Chapter 6

Summary and outlook

WR systems are mechatronic systems, because, during operation, internal interactions are between mechanical, electrical and electronic components. To have a better understanding of these interactions and also system behavior, WR systems are modeled with method of system simulation in uniformed modeling language, VHDL-AMS. Advantages are

- Design of interfaces between component models does not cost much effort. It follows the natural connections.
- Structure of model library is simple and maintenance is easy.

Modeling WR systems is based on modeling its components. And component modeling relies on models of sub components. The separation of macro components accords with component functions and features. The electrical and electronic components in the systemWR are drive, electronic hardware, switch and so on. Mechanical components are WR mechanism, door and so on. Each component of these is modeled either directly or on the basis of models of sub components, depending on the complexity of components and function separation. For instance, model electrical drive is an assembly of models of sub components, models of DCPM motor, worm gear and rubber damper. Rail WR mechanism is modeled by integrating models of cable drum, compressing spring, bowden cable, pulley, rail slider and so on.

It is not limited that these component models are used only for purpose of simulating WRs. With adapting, they can be utilized in simulating other products. Furthermore, when the focus of investigation is placed on the behavior of components or it is about to study a special case of component, component models are handy and helpful.

Since the objectives of this work is to bring improved understandings of system and component behavior, most of component models are created based on their physical principles. Some are modeled by describing their behavior. For example, it is illustrated in modeling rail slider. Due to the complicated geometry and mounting situation, friction between slider and rail is represented by a single parameter. It is identified with designated measurements. Another example is sealing friction, principle is clear but glass geometry is not considered. Therefore, piecewise linear model is used.

What is achieved in this work? Without losing focus on systems, major part of components are studied, described and modeled in this work.

- Electrical and mechanical behavior of drive are considered in modeling. Its parametrization relies on measurement of characteristic lines. In this work, a method is developed to determine power transmission efficiency of worm gear. It is achieved by comparing characteristic lines of DCPM motor and drive.
- Most components of mechanism are modeled by describing mechanical processes, with focus on frictional losses. It is well known that it is difficult to determine an accurate value of dry friction coefficient, since it depends on lots of factors, such as, temperature, lubrication, materials and so on. In models, friction coefficients are mostly from the measurements, which imitate actual working situation of components in WRs. In this way, credit is increased on parameters.
- Modeling of electronic functions is restricted to describe simple operation control and anti–pinch functions. These functions are the basis for other variants of electronic components in reality.

And real electronic components may have function to communicate with other parts in car and control other components, like door mirror. These function are not focus of this work. Therefore, models of hardware and software are kept simple and do not have many variants. Although simple, it has the same anti–pinch algorithms and parameters as in real software. It enables that engineers test anti–pinch functions and tune parameters in early phase of product developments.

- In applications, simulation of complete WR system serves as an aiding tool to improve understanding of system behaviors. Concretely, it is useful to study influence of design parameters. There design parameters can be a mechanical dimension, friction in door and so on.
- The options and freedom are provided for users of simulations to explore new applications and usefulness of WR system and component simulations.

Modeling and simulation are living processes. Models are always under improvements, with purpose of being more robust and being more close to reality.

- From one side, it is pursed that models are to cover up more natures, which are at the moment mainly electrics, mechanics and electronics.
- From another side, it is hoped that models and simulations can better predicate system behaviors.

However, a prerequisite to achieve the points above is a clear objective.

The following points are still open further investigation.

1. Influence of ambient temperature

The background is that WR systems are required to be feasible at temperature from $-30°C$ to $80°C$. The system behavior at $-30°C$ is different from at $20°C$ and $80°C$. It is resulted by the fact that charac-

teristics of electrical drive and friction at different locations in system change. To bring temperature effect in simulation of WR, influence on each property has to be studied. For example, resistance of electrical drive changes along with temperature and, as a consequence, motor constants, ke and kt, vary accordingly. In the end, such changes are reflected on drive characteristic lines. Sealing is also strongly effected by temperature. Rubber at low temperature becomes hard and brings more frictions. As a result, drive consumes more current and speed is lower.

2. Condideration of certain geometrical information
Certain geometrical information has effects on system behavior. Therefore, to promote models and simulations to a higher level, certain dimension should be taken into account. For instance, pinching force varies when horizontal pinching position shifts between two pillars. With an example of single rail WR, when pinch event takes place just above slider, pinching force has a normal value. When pinch event occurs close to pillar, force may increase because of glass tilting. As to the question how much the increase of friction is, it is necessary to introduce horizontal pinch position and glass dimension in modeling. These information may not be directly included into models, because it deals with geometrical calculations and it can burden simulation speed. They can be processed in a pre–step, supplied to models and then simulations with simplified values.

3. Collaboration with other component simulations
System simulation of WRs can be further strengthened by collaboration with other component simulations. Surely, component simulations can not provide an overview of system behaviors. However, component simulations have a better view of dominating factors, which influence component most. Some of these factors can have also strong effects on systems. By making use of component simulations, it saves effort and time to search for significant parameters of components. Parametrization of component models becomes easier when result and experiences from components simulations are available. For example, stiffness of

mechanism is made of stiffness of all its components. Proposed in this work, it can be experimentally measured. With existing 3D models, mechanism can be simulated with finite–element method. With consideration of influence of all components, system stiffness can be evaluated in finite–element simulation. It can then be an input parameter for system simulations. It does not only save the parametrization effort but also increase the robustness and credit of system simulations.

Appendix A

Content and structure of models in modeling language VHDL – Model of DCPM motor as an example

The buildup of models in VHDL consists mainly of two parts. The first part is the entity declaration. The second part is architecture of the declared entity. In entity delaration, model name, its interfaces to other models and parameters are defined. One model, or one entity, can have several architectures. One architecture is one realization of a model. Depending on objects, the realization can be description of behavior, physical principles or processes, integration of other components and so on. Here, model of DCPM motor is provided as an example.

```
library IEEE;
use IEEE.MATH_REAL.all;
use IEEE.ELECTRICAL_SYSTEMS.ALL;
use IEEE.MECHANICAL_SYSTEMS.ALL;
```

At the beginning of model, library and packages are imported.

```
entity dcpm_motor is
  generic(
  ke   : real:= 21.7e-03;
  kt   : real:= 15.0e-03;
  laa   : real:= 0.09e-03;
  ra   : real:= 0.57;
  j   : real:= 9.85e-06;
  IA0   : REAL := 0.0;
  rad_armature0    : REAL := 0.0;
  vel_armature_radps0 : REAL := 0.0);
  port(
  terminal plus, minus : electrical;
  terminal armature: rotational);
end entity dcpm_motor;
```

Model is declared as an entity.
Clause “generic” declares parameters of model.
Clause “port” declares pins and its natures.

```
architecture simple of dcpm_motor is
  quantity ua across ia through plus to minus;
  quantity rad_armature across trq_armature through
     armature;
  constant N2W : REAL := 2.0 * MATH_PI / 60.0;
  constant W2N : REAL := 60.0 / (2.0 * MATH_PI);
  quantity vel_armature_radps : REAL;
  quantity vel_armature_rpm    : REAL;
  quantity acc_armature_radpss: real;
  quantity IA_DOT   : REAL;
  quantity power_inp_elec:real:=0.0;
  quantity power_outp_mech:real:=0.0;
  quantity dcpm_motor_eff:real:= 0.0;
```

Realization of model is started with “architecture”. At the beginning of architecture, associated across and through variables, necessary constants, useful quantities for calculation and later analysis are defined.

```
begin
  UA == RA * IA + Laa * IA_DOT + Ke*
     vel_armature_radps;
  kt*ia  ==  j * acc_armature_radpss + trq_armature
     ;
  if DOMAIN = QUIESCENT_DOMAIN and rad_armature0 /=
     REAL'LOW use
    rad_armature == rad_armature0;
  else
    rad_armature'DOT == vel_armature_radps;
  end use;
  if DOMAIN = QUIESCENT_DOMAIN and
     vel_armature_radps0 /= REAL'LOW use
    vel_armature_radps      == vel_armature_radps0;
  else
    acc_armature_radpss      == vel_armature_radps'
       DOT;
  end use;
  if DOMAIN = QUIESCENT_DOMAIN and IA0 /= REAL'LOw
     use
    IA == IA0;
  else
    IA'DOT == IA_DOT;
  end use;
  vel_armature_rpm == vel_armature_radps * W2N;
  power_inp_elec == IA * UA;
  power_outp_mech == vel_armature_radps *
     trq_armature;
  dcpm_motor_eff == power_outp_mech /
     power_inp_elec;
```

```
end architecture simple;
```

Realization of model is achieved with Eqs. and restricting conditions.

Model of DCPM motor is built up with the four parts above. Other models are created in the same structure.

Appendix B

Comparison of parameter identification methods for model of DCPM motor

One source of motor data is the component specification. As a technical and qualitative control of components, car manufacturers require component data sheet according to defined specifications during product development processes. The specification requests component data from various aspects, for example, electrical, mechanical, chemical, climatic requirements and component related characteristics. From these requirements, it is possible to extract characteristic values. The advantage of component specification as parameter source is

1. Data is formalized in database or spreadsheet
2. Time-saving in searching

However, such convenience is based on the precondition, that the component specification and data sheet are available for a wide range of motors. In industry, the situation depends on car manufacturers, some

request motor data sheet, while others do not. A second problem is the credit on data sheets. Component suppliers, system suppliers and car manufacturers may not have the same understanding on the same parameters and the methods to define and identify values of these parameters may be also different. The comparison of calculation result with values from data sheet and measurement result may have an unexplainable difference. It is not seldom that the industrial measurements do not have enough precision for scientific purpose.

Kleis [104] described DCPM motor in two Eqs. B.1 and gave a brief explanation of parameter identification method. The Eq. of electrical characteristic from Mr. Kleis is the same as in this work, see in Eq. B.1a and Eq. 4.1a. In the mechanical description, the part of Coulomb friction, static friction, is neglected in Eq. B.1b, compared with Eq. 4.1b.

$$U_a = k_e \cdot \omega_a + R_a \cdot i_a + L_a \cdot \frac{i_a}{t} \tag{B.1a}$$

$$k_t \cdot i_a = Visc \cdot \omega_a + J_a \cdot \frac{d}{dt}\omega_a + M_{la} \tag{B.1b}$$

With static tests, it is possible to measure current and rotational velocity under no-load and stall conditions, so as to obtain values of i_0, no-load current, ω_{a0}, no-load velocity, i_b, stall(block) current and M_b, stall torque. Because of static tests, the effects of inductor and inertia are zero. By applying the no–load and stall values into Eq. B.1, the four unknown parameters are calculated by the Eq. B.2.

$$k_e = \frac{U_a - R_a \cdot I_a}{\omega_{a0}} \tag{B.2a}$$

$$R_a = \frac{U_a}{I_B} \tag{B.2b}$$

$$k_t = \frac{M_B}{I_B} \tag{B.2c}$$

$$Visc = k_t \cdot \frac{I_0}{\omega_{a0}} \tag{B.2d}$$

The calculation of motor parameter is well known in textbook[105]. Internal friction loss of motor is only viscous friction. Calculation of parameter, k_e, is based on the assumption that the performance curves are completely linear and the influence from $L_a \frac{d}{dt} I_a$ and $J \frac{d}{dt} \omega_a$ is neglected. In calculation of k_t, I_0 is neglected. With known measurements under no–load and stall conditions, this method is quick to use. However, the quality of this method is not evaluated through verification and validation of parameter values and mathematical model.

The third method of parameter identification is a tool from Saber® Synopsys®. The full name of the tool is "The DCPM Motor Tool". The tool is coupled with Saber® simulator and its motor model, dc_pm2. The DC Eq. in dc_pm2 model are the following.

$$U_a = R_a \cdot I_a + k_e \cdot \omega_a + V_b \tag{B.3a}$$

$$J_a \cdot \frac{d}{dt} \omega_a = k_t \cdot i_a - M_d - DZi \cdot abs(\omega_a) - M_l \tag{B.3b}$$

To characterize, it needs a list of parameters ,see in Tab. B.1. Along with the list of parameters, a number of laboratory measurements methods are suggested for determining values of critical parameters, such as armature resistance, winding inductance, k_e, k_t, brush drop, motor inertia, friction and damping. Besides voltage source and current meter, equipments like current source, pulse generator, torque transducer and rotational speed meter, are required to carry out these measurements. The accuracy of conventional multimeter may not be satisfactory, because some of motor parameters require Milli or even micro resolution. The procurement of suitable equipments may bring additional cost. To improve the reliability of parameter values, measurements should repeated at several armature positions and at several motors. Analysis of measurement data are necessary. Average value should be found out and later taken as parameters. The tool and laboratory methods proposed by Saber® are well formed. With them, parameter quality can be improved. But it costs, at the same time, relatively more effort.

Table B.1: Parameters of Saber® tool

Parameter	Definition
r_a	armature winding resistance
L_a	armature winding inductance
k_e	Back EMF constant
k_t	Torque constant
sft	static friction torque loss
dft	dynamic friction torque loss
rcw	compensating winding resistance
lcw	compensating winding inductance
dzi	viscous motor damping constant
J_a	motor inertia
bd	brush drop voltage
ibd	brush drop leakage current
p	number of poles

Another example of DCPM motor modeling and parameter identification is from teaching material in university [1]. In the teaching material, DCPM motor is described by the following Eq. B.4.

$$V = I \cdot R + K_v \cdot \omega \tag{B.4a}$$

$$T = K_m \cdot I \tag{B.4b}$$

If the Eqs. above are expressed in SI UNITS, K_v and K_m are equal,

$$\omega = \left(\frac{V}{K}\right) - \left(\frac{R}{K^2}\right) T \tag{B.5a}$$

V : *voltage*

R : *winding resistance*

T : *total torque acting on rotor of motor*

Under the condition that V, K and R are time constant, it reveals that speed of rotor is a linear function of torque applied on it. Despite of the fact that the model is easy to understand, the limitations of this motor model are also stated clearly in the teaching material. The

[1] Characteristics of DC Motors, Prof. Bundbar P. Birnie, Department of Materials Science and Engineering, Rutgers University

torque on motor is lumped into one term, which includes output torque and internal friction losses. Inductance and inertia are assumed to be zero. For a practical usage, more information is required for motor characteristics.

Identification can be achieved within less time and effort, if component specification and data sheet are available. One of the drawbacks of it is that definition of the same parameters may differ between suppliers and customers. The other three methods describe DCPM motor with electrical and mechanical characteristic Eqs. at different complexity. The number of involved parameters increases as complexity increases in Eqs.. Based on the need of precision, methods of parameter identification have to be developed correspondingly. Verification and validation are necessary to prove the reliability of parameters and to increase the credit on models. However, it always depends on in which detailed degree models are required. By comparing several methods above, it is concluded that requirement determines ways to model DCPM motor, to develop parameter identification methods and to verify and validate. For the purpose to give collage student an simple introduction of principle, a highly simplified model is enough and it is not necessary to compare with real measurements. If the motor is used as actuator in high precision machine, effort should be paid to identification procedures of each single parameter.

The effort of parameter identification with the method in this work is less, comparing with the laboratory methods of Saber®. The Fig. B.1 is the summary of working hours for the two methods. Laboratory methods cost 33 working hour to measure 10 motors and determine parameters after analysis, regardless of the fact that two measurements can not be conducted because of lacking of equipments. Performance curve measurements of 10 motors takes 50 minutes and post analysis takes another 1 hour, which is all together less than 2 hour for 10 motors. Probably, Saber® methods can help find out more accurate parameters and therefore a better fitting to measurements can be produced. It can be assumed that fitting is improved 10% better. However, the effort

used in the former method is more than 10 times of the latter one. It is not to deny the usefulness of Saber® method. If there is a strong request to investigate deeper in the topic of motor, the method will play an important role. Under the current situation, the method used in this work is already enough to reveal the behaviors of DCPM motor.

Parameter	Unit	Description	Devices	Time cost per motor	Time cost per 10 motors	Test setup	Post analyse	Total
Ra	Ohm	Motor Winding resistance	* motor holder * voltage source * current sensor/meter	10 min	2 hour	1 hour	3 hour	6 hour
La	H	Motor Winding Inductance	* motor holder * voltage source, step input * current sensor/meter	10 min	2 hour	1 hour	3 hour	6 hour
Ke	v/rad/s	emf constant	* mashine configured in generating mode.	10 min	2 hour	1 hour	3 hour	6 hour
Kt	N*m/A	torque constant	* torque-wrench or torque transducer * voltage source * current source * current meter or sensor	N/A	N/A	N/A	N/A	N/A
bd	v	brush drop voltage	* voltage source * current meter or sensor	10 min	2 hour	1 hour	3 hour	6 hour
J	kg*m2	Motor inertia	* voltage source * rotational speed meter or sensor	N/A	N/A	N/A	N/A	N/A
Mfric	N*m	Motor Friction and damping factor	* voltage source * current meter or sensor * rotational speed meter or sensor	30 min	5 hour	1 hour	3 hour	9 hour
								33 hour

Type of measurement	Time cost per motor [min]	Amount	Time [min]	Post-analysis [min]	Sum [min]
DCPM motor performance curves	5	10	50	60	110
Drive performance curves	5	10	50	60	110

Total	220	min
	3,67	hour

Figure B.1: Measurement effort. Top: laboratory methods of Saber® Down: Calculation of characteristic curves

Bibliography

[1] N. Kyura and H. Oho, "Mechatronics–an industrial perspective," *Mechatronics, IEEE/ASME Transactions*, vol. 1, no. 1, pp. 10–15, 1996.

[2] T. Mori, "Mechatronics," *Yasakawa Internal Trademark Application Memo 21.131.01*, July 12 1969.

[3] R. H. Bishop, *Mechatronics – An Introduction*. CRC Press, September 13, 2005.

[4] R. H. Bishop, *The Mechatronics Handbook*, 2nd ed. CRC Press, February 26, 2002.

[5] F. Harashima, M. Tomizuka, and T. Fukuda, "Mechatronics – "What is it, why and how?" An editorial," *IEEE/ASME Transactions on Mechatronics*, vol. 1, no. 1, pp. 1–4, 1996.

[6] R. Isermann, "On the design and control of mechatronic systems – a survey," *IEEE Transactions on Industrial Electronics*, vol. 43, no. 1, pp. 4–15, 1969.

[7] J. Wallascheck, "Modellierung und Simulation als Beitrag zur Verkürzung der Ent–wicklungszeiten mechatronischer Produkte," in *Tagung Simulation in der Praxis*, vol. 1283. VDI-Berichte, 1995, pp. 35–50.

[8] W. Bolton, *Mechatronics: Electrical Control Systems in Mechanical and Electrical Engineering*, 5th ed. England: Prentice Hall, February 3, 2013.

[9] W. Schafer and H. Wehrheim, "The challenges of building advanced mechatronic systems," in *Future of Software Engineering*. IEEE Computer Society Washington, DC, USA, July 2007, pp. 72–84.

[10] K. Craig, "The role of computers in mechatronics," *IEEE Computing in Science and Engineering*, vol. 5, no. 2, pp. 80–85, 2003.

[11] K. Craig, "Mechatronics in university and professional education: Is there anything really new here?" *IEEE Education Special Issue of the Journal of Robotics and Automation*, vol. 8, no. 2, pp. 12–19, 2001.

[12] K. Craig and F. Stolfi, "Teaching control system design through mechatronics," *Mechatronics*, vol. 12, pp. 371–381, 2002.

[13] W. Schafer and H. Wehrheim, "Mechatronics: Designing intelligent machines," in *Proc. IEEE-Int. Conf.* Univ. of Cambridge, Sep. 12-13 1990, pp. 72–84.

[14] D. A. Bradley, D. Dawson, D. Burd, and A. J. Loader, *Mechatronics-Electronics in Products and Proceses*. London: Chapman and Hill, 1991.

[15] P. A. McConaill, P. Drew, and K. H. Robrock, *Mechatronics and Robotics*. Amsterdam: IOS-Press, 1991.

[16] G. Schweitzer, "Mechatronics – a concept with examples in active magnetic bearings," *Mechatronics*, vol. 2, no. 1, pp. 65–74, 1992.

[17] R. Isermann, "Integrierte mechanisch – elektronische Systeme," *Fachtagung Tech. Univ. Darmstadt*, vol. 12, no. 179, 1993.

[18] B. A. Hussein, "Modeling the physical and logical properties of mechatronics systems," Ph.D. dissertation, the Norwegian University of Science and Technology, Trondheim, 1999.

[19] G. Saikalis, H. Meyl, S. Oho, and D. McCune, "Virtual embedded mechatronics system," *SAE Technical Paper 2006–01–0861*, April 03 2006.

[20] C. Unsal and P. K. Khosla, "Mechatronic design of a modular self-reconfiguring robotic system," in *Robotics and Automation.Proceedings. ICRA '00. IEEE International Conference*, vol. 2, 2000, pp. 1742–1747.

[21] G. L. Gissinger, C. Menard, and A. Constans, "A mechatronic conception of a new intelligent braking system," *Control Engineering Practice*, vol. 11, no. 2, pp. 163–170, Feb 2003.

[22] R. S. Sharp and D. A. Crolla, "Intelligent suspension for road vehicles – current and future developments," in *EAEC-Int. Conf. New Developments Power Train, Chassis Eng.*, Strassburg, 1987, pp. 579–601.

[23] J. Wikander and M. Törngern, "Mechatronics as an engineering science," in *Mechatronics, the 6th UK Mechatronics Forum International Conference*, Skövde, Sweden, 9-11 September 1998, pp. 651–656.

[24] Z. Affi, B. EL-Kribi, and L. Romdhane, "Advanced mechatronic design using a multi-objective genetic algorithm optimization of a motor-driven four-bar system," *Mechatronics*, vol. 17, no. 9, pp. 489–500, Nov 2007.

[25] D. Shetty and R. A. Kolk, *Mechatronics System Design: SI*, 2nd ed. Cengage Learning Emea, 2010.

[26] T. Yoshimura, K. Nakaminami, M. Kurimoto, and J. Hino, "Active suspension of passenger cars using linear and fuzzy-logic con-

trols," *Control Engineering Practice*, vol. 7, no. 1, pp. 41–47, Jan 1999.

[27] W. Bolt, *Mechatronics: Electronic Control Systems in Mechanical and Electrical Engineering*, 3rd ed. Prentice Hall, 2003.

[28] K. Janschek, *Mechatronic Systems Design: Methods, Models, Concepts*. Springer, 2012.

[29] M. Steinbuch, Ed., *Mechatronics, A journal of IFAC(the International Federation of Automatic Control)*. ELSE, 2013.

[30] R. Isermann, *Mechatronische Systeme: Grundlage*, 2nd ed. Springer, 2008.

[31] VDI–Fachbereich Produktentwicklung und Mechatronik, Ed., *VDI 2206 – Entwicklungsmethodik für mechatronische Systeme*. VDI–Gesellschaft Produkt– und Prozessgestaltung, Jun 2004.

[32] J. M. Rolfe and K. J. Staples, Eds., *Flight Simulation (Cambridge Aerospace Series)*. Cambridge University Press, Jan. 12 2008.

[33] R. P. Allan, M. A. Ringer, J. A. Pamment, and A. Slingo, "Simulation of the earth's radiation budget by the european centre for medium-range weather forecasts 40-year reanalysis (era40)," *Journal of Geophysical Research: Atmospheres*, vol. 109, no. D18, 27, Sep. 18 2004.

[34] P. C. Cacciabue, *Modelling and Simulation of Human Behaviour in System Control (Advances in Industrial Control)*. Springer London, Jan. 1 1998.

[35] J. A. Sokolowski and C. M. Banks, Eds., *Modeling and Simulation Fundamentals: Theoretical Underpinnings and Practical Domains*. John Wiley & Sons, Inc., 2010.

[36] B. P. Zeigler, T. Kim, and H. Praehofer, *Theory of Modeling and Simulation: Integrating Discrete Event and Continuous Complex Dynamic Systems*, 2nd ed. Academic Press, Jan 2000.

[37] H. Bossel, *Modeling and Simulation*. A K Peters, July 1994.

[38] J. A. Sokolowski and B. C. M., Eds., *Principles of Modeling and Simulation: A Multidisciplinary Approach*. John Wiley & Sons, Inc., 2009.

[39] G. Pelz, *Mechatronic systems: modeling and simulation with HDLs*. John Wiley & Sons, Inc., Apl. 8 2003.

[40] W. de Silva, *Mechatronics*. CRC Press Inc., Nov. 29 2004.

[41] D. S. Nesculescu, *Mechatronics*. Addison Wesley Pub Co Inc, Dec 2001.

[42] J. P. Davim, Ed., *Mechatronics*. ISTE Ltd and John Wiley & Sons, Inc., 2011.

[43] S. Petkun, "Simulation of a window regulator in car door," in *European ASSURE Meeting*, Munich, Germany, Nov. 14 2001.

[44] S. Petkun, "Dynamische Modellierung eines komplexen mechatronischen Systems im Rahmen eines Simulators an dem Beispiel eines elektrischen Fensterhebers," in *Erstes Internationales Symposium für Mechatronik*, Chemnitz, Germany, Mar. 21–22 2002, pp. 358–366.

[45] Brose Fahrzeugteile GmbH, "Window lifter, especially for motor vehicles," Patent DE3 152 329A1, 07, 1983.

[46] P. Hlousek and G. Mühling, "Cable-return pad," Patent DE3 906 682A1, 09, 1990.

[47] P. Da Cruz, H. Dohles, A. Herwig, H. Hugel, F. Fassbender, U. Sommer, and M. Järpsten, "Window lifter," Patent WO2 004 057 142A2, 07, 2004.

[48] J. Held and R. Kalb, "Window lift, control device for a window lift and method for controlling a window lift," Patent WO2 005 041 378A1, 10, 2004.

[49] A. Stahn and H. Wich, "Carrier for a vehicle window pane regulator," Patent EP1 400 650B1, 09, 2003.

[50] A. Eberlein, M. Friedrich, H. Lieb, and J. Seeberger, "Motor-driven window lifter with anti-nipping device for a vehicle," Patent EP0 806 538B1, 05, 1997.

[51] P. Hess, "Lifting mechanism for a large window," Patent US3 897 652, 08, 1975.

[52] P. Hlousek, "Kreuzarm–Fensterheber, insbesondere für Kraftfahrzeuge," Patent DE3 606 902A1, 09, 1987.

[53] W. Commerell, H.-T. Mammen, K. Panreck, and J. Haase, "Simulation technischer Systeme – Anforderungen und Perspektiven," in *Fachtagung Simulation in Produktion und Logistik*. Berlin: Fraunhofer IRB Verlag, 10 2008.

[54] E. Hessel, J. Haase, and O. Hädrich, "Fortschritte bei der Systemsimulation im Automobilbau," in *Workshop der ASIM/GI-Fachgruppen STS und GMMS, Simulation technischer Systeme und Grundlagen und Methoden in Modellbildung und Simulation*, Wolfenbüttel, Germany, Feb. 23-24 2012.

[55] H.-T. Mammen and U. Buschmann, "Modellbeispiele mechatronischer Systeme," in *Workshop der ASIM/GI-Fachgruppen STS und GMMS, Simulation technischer Systeme und Grundlagen und Methoden in Modellbildung und Simulation*, Wolfenbüttel, Germany, Feb. 23-24 2012.

[56] A. Schön, "Erstellung einer firmenweiten Modellbibliothek – Potentiale, Anforderungen und Herausforderungen," in *Workshop*

der ASIM/GI-Fachgruppen STS und GMMS, Simulation technischer Systeme und Grundlagen und Methoden in Modellbildung und Simulation, Wolfenbüttel, Germany, Feb. 23-24 2012.

[57] S. Petkun, "Simulation added development on mechatronic products on the basis of car electrically power window regulator simulation," in *Proceedings of 47 Internationales Wissenschaftliches Kolloquium*, Ilmenau, Germany, 2002.

[58] S. Petkun and S. Khader, "Dynamische Modellierung eines Antriebes mit Zugmittelgetrieben," in *Proceedings of 47 Internationales Wissenschaftliches Kolloquium*, Ilmenau, Germany, 2002.

[59] S. Petkun, "Dynamical simulation of electrical window regulator demands on complete new verification approaches," in *SNUG Saber*, Munich, Germany, Oct. 08 2002.

[60] P. Tuinenga, *Spice: A Guide to Circuit Simulation and Analysis Using PSpice*, 3rd ed. Prentice Hall PTR Upper Saddle River, 1995.

[61] A. Angermann, M. Beuschel, M. Rau, and U. Wohlfarth, *MATLAB - Simulink - Stateflow: Grundlagen, Toolboxen, Beispiele*, 1st ed. Oldenbourg Wissenschaftsverlag, Nov. 2 2011.

[62] I. Getreu, "Behavioral modeling of analog blocks using the saber simulator," in *Circuits and Systems, Proceedings of the 32nd Midwest Symposium*, Champaign, IL, US, Aug. 14-16 1989, pp. 977–980.

[63] C. Chuang and C. Harrison, "Analogue behavioural modelling and simulation using vhdl and saber-mast," in *Mixed Mode Modelling and Simulation, IEE Colloquium*, London, UK, 1994, pp. 1–5.

[64] *IEEE Standard VHDL Analog and Mixed-Signal Extensions*, IEEE, Aug. 06 2002, 1076.1-1999.

[65] *IEEE Standard for VHDL Analog and Mixed-Signal Extensions – Packages for Multiple Energy Domain Support*, IEEE, Apr. 19 2011, 1076.1.1-2011.

[66] P. Ashenden, G. Peterson, and D. Teegarden, *The System Designer's Guide to VHDL-AMS. Analog, Mixed-Signal, and Mixed-Technology Modeling*. Morgan Kaufmann, Sep. 10 2002.

[67] *IEEE Standard VHDL Language Reference Manual*, IEEE, Jan. 26 2009, 1076-2008.

[68] P. Ashenden, *The designer's guide to VHDL*, 3rd ed. Morgan Kaufmann, Nov. 11 2006.

[69] R. Shannon, *Systems Simulation - The Art and Science*, 1st ed. Prentice Hall, Jun 1975.

[70] O. Balci, "Verification, validation, and certification of modeling and simulation applications," in *Proceedings of the 35th conference on Winter simulation: driving innovation: driving innovation*, 2003, pp. 150–158.

[71] A. Law, *Simulation Modeling and Analysis*, 4th ed. Mcgraw-Hill Professional, Jun. 01 2006.

[72] O. Balci, "Verification validation and accreditation of simulation models," in *Proceedings of the 29th conference on Winter simulation, IEEE Computer Society*, Washington, DC, USA, 1997, pp. 135–141.

[73] X. Zhao, S. Petkun, I. Zeidis, and K. Zimmermann, "Dynamics of an electrical window regulator system," *Scientific Journal of IFToMM, Problems of Mechanics*, vol. 4, no. 53, pp. 7–14, 2013.

[74] A. Andronov, A. Vitt, and S. Khaikin, *Theory of oscillators*. Dover Publicationsl, 2001.

[75] N. Bogoljubow and Y. Mitropolski, *Asymptotic methods in the theory of non-linear oscillations*. Gordon and Breach, 1961.

[76] K. Zimmermann, I. Zeidis, M. Bolotnik, and M. Pivovarov, "Dynamics of a two-module vibration-driven system moving along a rough horizontal plane," *Multibody System Dynamics*, vol. 22, pp. 199–219, 2009.

[77] R. Krishnan, *Electric motor drives: Modeling, analysis and control*, united states ed ed. Prentice Hall, Feb. 2001.

[78] S. Filizadeh, *Electric Machines and Drives: Principles, Control, Modeling, and Simulation*. Crc Pr Inc, 2013.

[79] W. Piotr, *Dynamics and Control of Electrical Drives*. Springer, 2011.

[80] A. Zaher and M. Zohdy, "Computer modeling and simulation of DCPM motors," in *ASM 07 The 16th IASTED International Conference on Applied Simulation and Modelling*, Spain, 2007, pp. 306–311.

[81] W. Mason, "Electrical and mechanical analogies," *Bell system technical jounal*, vol. 5, no. 3, pp. 493–502, 1926.

[82] F. Firestone, "A new analogy between mechanical and electrical systems," *Journal of the Acoustical Society of America*, vol. 4, no. 3, pp. 249–267, 1933.

[83] R. Cooper, *The Designer's Guide to Analog and Mixed-Signal Modeling*. Avant! Corporation, 2001.

[84] R. G. Sargent, "Verification and validation of simulation models," in *WSC 05 Proceedings of the 37th conference on Winter simulation*, 2005, pp. 130–143.

[85] I. Dudas, *The Theory and Practice of Worm Gear Drives*. Elsevier Science & Technology, 1 Nov. 2000.

[86] H. S. Fang and C. B. Tsay, "Mathematical model and bearing contacts of the zn-type worm gear set cut by oversize hob cutters," *Mechanism and Machine Theory*, vol. 35, no. 12, pp. 1689–1708, 2000.

[87] K. Y. Chen and C. B. Tsay, "Mathematical model and worm wheel tooth working surfaces of the zn-type hourglass worm gear set," *Mechanism and Machine Theory*, vol. 44, no. 9, pp. 1701–1712, 2009.

[88] C. B. Tsay, J. W. Jeng, and H. S. Feng, "A mathematical model of the ze-type worm gear set," *Mechanism and Machine Theory*, vol. 30, no. 6, pp. 777–789, 1995.

[89] F. L. Litvin, I. Gonzalez-Perez, K. Yukishima, A. Fuentes, and K. Hayasaka, "Design, simulation of meshing, and contact stresses for an improved worm gear drive," *Mechanism and Machine Theory*, vol. 42, no. 8, pp. 940–959, 2007.

[90] R. Stolyarchuk, "Multibody modeling and dynamical analysis of the worm gear drive system," in *The 48th Scandinavian Conference on Simulation and Modeling*, Göteborg, 30-31 Oct. 2007, pp. 66–72.

[91] X. Zhao and S. Petkun, "Modeling worm gear mechanism in three architectures, parameter identification and comparison," in *ASIM–Treffen STS/GMMS 2013*, Düsseldorf, Germany, 2013, pp. 219–226.

[92] H. R. Müller, "Zur Kinematik des Rollgleitens," *Archiv der Mathematik*, vol. 4, no. 3, pp. 239–246, 1955.

[93] D. P. Townsend, *Dudley's Gear Handbook*, 2nd ed. Mcgraw-Hill, Sep. 1991.

[94] J. Ziemer, S. Abernathy, J. Rosenbaum, S. Miller, and M. Okazaki, "Method of operating a wormgear drive at high energy efficiency," Patent US7 045 055B2, 04, 2004.

[95] M. Merkel and K.-H. Thomas, *Taschenbuch der Werkstoffe*. Carl Hanser Verlag, 17 Jan. 2008.

[96] K. L. Johnson, *Contact Mechanics*. Cambridge University Press; 1 edition, 28 Aug. 1987.

[97] S. W. Attaway, "The mechanics of friction in rope rescue," in *International Technical Rescue Symposium*, 1999.

[98] C. Fender and J. Waßmuth, "Verfahren zur Extraktion einer Weg- oder Winkelinformation aus einem elektrischen Signal eines elektrischen Antriebs mit einem Gleichanteil und einem im Wesentlichen sinusförmigen oder sinusformartigen Wechselanteil," Nov. 12 2009, dE Patent App. DE200,810,022,638.

[99] J. Übelein and B. Bopp, "Steuerungssystem für Fensterheber eines Kraftfahrzeugs," Jan. 3 2007, eP Patent App. EP20,060,012,106.

[100] R. Kalb, "Fensterheber," Oct. 28 2004, dE Patent App. DE200,410,017,110.

[101] S. Petkun, "Practical aspects of modeling of mechatronics system at the example of brosant system," in *ASIM–Treffen STS/GMMS 2013*, Düsseldorf, Germany, 2013, pp. 227–231.

[102] S. Petkun and X. Zhao, "Brosant – an example of the mechatronical way of thinking," in *Workshop der ASIM/GI-Fachgruppen STS und GMMS, Simulation technischer Systeme und Grundlagen und Methoden in Modellbildung und Simulation*, Wolfenbüttel, Germany, Feb. 23-24 2012.

[103] S. Petkun, "Mechatronics simulation on system level: Brosant approach," in *21. Symposium Simulationstechnik, Grundlagen,*

Methoden und Anwendungen in Modellbildung und Simulation, Winterthur, Schweiz, Sep. 7-9 2011.

[104] A. Kleis, "Zuverlässigkeitsanalyse eines permanenterregten Gleichstrommotors für den Einsatz in elektrischen Schleißsystemen für Kraftfahrzeuge," Master's thesis, Bergische Universität Wuppertal, Oct. 2004.

[105] R. Fischer, *Elektrische Maschinen*, überarbeitete und erweiterte auflage ed. München: Hanser Verlag, 1995.